



2D cross-hole MMR – Survey design and sensitivity analysis for cross-hole applications of the magnetometric resistivity method

Daniel Fielitz

Forschungszentrum Jülich GmbH
Institut of Bio- and Geosciences (IBG)
Agrosphere (IBG-3)

2D cross-hole MMR – Survey design and sensitivity analysis for cross-hole applications of the magnetometric resistivity method

Daniel Fielitz

Schriften des Forschungszentrums Jülich
Reihe Energie & Umwelt / Energy & Environment

Band / Volume 95

ISSN 1866-1793

ISBN 978-3-89336-689-7

Bibliographic information published by the Deutsche Nationalbibliothek.
The Deutsche Nationalbibliothek lists this publication in the Deutsche
Nationalbibliografie; detailed bibliographic data are available in the
Internet at <http://dnb.d-nb.de>.

Publisher and
Distributor: Forschungszentrum Jülich GmbH
Zentralbibliothek
52425 Jülich
Phone +49 (0) 24 61 61-53 68 · Fax +49 (0) 24 61 61-61 03
e-mail: zb-publikation@fz-juelich.de
Internet: <http://www.fz-juelich.de/zb>

Cover Design: Grafische Medien, Forschungszentrum Jülich GmbH

Printer: Grafische Medien, Forschungszentrum Jülich GmbH

Copyright: Forschungszentrum Jülich 2011

Schriften des Forschungszentrums Jülich
Reihe Energie & Umwelt / Energy & Environment Band / Volume 95

D 38 (Diss., Köln, Univ., 2010)

ISSN 1866-1793
ISBN 978-3-89336-689-7

Neither this book nor any part of it may be reproduced or transmitted in any form or by any
means, electronic or mechanical, including photocopying, microfilming, and recording, or by any
information storage and retrieval system, without permission in writing from the publisher.

to my parents

I would never have come so far without you!

Acknowledgment

I would like to thank the people who helped and supported me during my 4 years of Ph.D. research work, both on scientific and personal level.

First of all, I would like to thank my official supervisors Prof. Andreas Kemna and Egon Zimmermann, who both contributed a great deal to my work and without whom this work would not have been the same. I really appreciated the numerous discussions around the subject of my Ph.D. research work. You constantly provided me with scientific and technical advice that always helped me to refocus and to solve the open questions.

Secondly, I thank my Ph.D. supervisor at the University of Cologne Prof. Bülent Tezkan for your friendly disposition to accept the mentoring of this Ph.D. thesis. I thank Prof. Harry Vereecken, my additional Ph.D. supervisor and director of the Institute Agrosphere at the Forschungszentrum Jülich, for the possibility to do my Ph.D. at the Institute Agrosphere, for all the support and for the opportunity to travel around and visit conferences and workshops to present my work and to study further, I really enjoyed that. In addition, I thank you both for always listening to my scientific problems if necessary.

Thirdly, I would like to thank my colleagues at the Forschungszentrum Jülich and of the RTB-group for their kindness and for the great working atmosphere: Ulrike Rosenbaum, Sarah Garre, John Koestel, Xander Huisman and Franziska Wedekind. In particular, I thank the colleagues at the Central Institute of Electronics, who always had a warm welcome, a helping hand and a good coffee for me. Special thank goes to: Walter Glass, Joachim Berwix and Heinrich Meier, who additionally helped during several test measurements in the field.

In addition, I would like to thank Prof. Giorgio Cassiani (University of Padua) for letting me (and our research group) participate in and for the fantastic organization of the 2006 Gorgonzola field campaign. I really appreciated your kindness and the down-to-earth atmosphere during the measurements. The realization of the field measurements enormously contributed to the overall success of this research work.

My very special thank goes to Sarah Garre and Davor Turkovic, who particularly assisted me during the last phase of this Ph.D. research work both scientifically and mentally. Sarah with your scientific comments this thesis reach another level. Davor, your scientific, personal and mental support helped me to actually stay focused and to see through the last phase. Above all, I thank Melissa Leis and Ulrike Rosenbaum who also contributed to my thesis by proofreading. Finally, I thank my friends Anke Giffhorn, Sebastian Dohe, Robert Schmale and Mamo Hajo as well as my family, who kept feeding me with positive energy.

Abbreviations

MMR	Magnetometric resistivity method
2D	Two-dimensional
3D	Three-dimensional
AMR	Anisotrope Magnetoresistive
DC	Direct current (or pseudo DC) resistivity method
DHMMR	Drillhole or downhole MMR
DHTEM	Drillhole Time-domain Electromagnetic
EIT	Electrical impedance tomography
EM	Electromagnetic
ERT	Electric resistance tomography
FD	Finite Differences
FE	Finite Elements
FT	Fourier transformation
GPR	Ground penetrating radar
IP	Induced polarization
MERIT	Magneto-electrical resistivity imaging technique
MIP	Magnetic induced polarization
SAM	Sub-Audio Magnetics
SNR	Signal-to-noise ratio
TEM	Time-domain electromagnetic
TFMMR	Total Field Magnetometric resistivity method

Symbols

\mathbf{B}	Magnetic field ¹
\mathbf{B}^b	Magnetic field measured within borehole
\mathbf{B}^r	Magnetic field measured at reference station
\mathbf{B}_{ext}	External magnetic field
B^E	Earth magnetic field
B^g	Ground component of the MMR response
B^m	Modulation part or measured magnetic field
B_p	Parasitic correlated noise field
B^w	Wire component of the MMR response
B_θ	Azimuthal displacement from the x-axis
B_ϕ	Elevation displacement from the xy-plane
B_R	Magnitude of the magnetic field
\mathbf{d}	Data vector
d	Depth of the transmitter electrode
\mathbf{dl}	Infinitesimal wire element
dv'	Volume element
dx	Discretization size in x-direction
dz	Discretization size in z-direction
f	Frequency
F_1	Sensor-specific scaling factor
I	Current strength
\mathbf{j}	Current density
\mathbf{J}	Jacobian Matrix
K_o	Modified Bessel function of zero order
k	Wavenumber (corresponds to the Cartesian y-component)
l	Transmitter index

¹ Strictly speaking the measured quantity \mathbf{B} is the magnetic flux density related to the magnetic field, \mathbf{H} , as $\mathbf{B} = \mu \cdot \mathbf{H}$. For convenience, \mathbf{B} is herein likewise referred to as the magnetic field.

m	Model vector
<i>m</i>	Sensor index
N	Number of elements /supporting points
N_b	Number of elements in the outer grid
N_c	Number of individual measurement configurations
N_m	Number of data points of a measurement cycle
N_x	Number of elements in the x-direction (central grid)
N_z	Number of elements in the z-direction (central grid)
<i>n</i>	Resistivity block index
r	Vector to the point of measurement
r'	Vector to the considered subsurface volume
r_s	Vector pointing to the current source location
<i>r</i>	Displacement from the wire Borehole separation
$r(t)$	Reference signal / reference function
<i>s</i>	Conductivity contrast $s = \rho_2/\rho_1$
<i>S</i>	Cross-sectional area
T_{CPU}	Computational time
t_i	Time step
t_{int}	Integration time
<i>U</i>	Voltage
u_{out}	Output voltage (output of the fluxgate sensor)
<i>V</i>	Volume
(<i>X, Y, Z</i>)	Cartesian coordinates / Local coordinate system
<i>Z</i>	Impedance
(x_r, y_r, z_r)	Local coordinates of the magnetic reference sensor
x_b	Dimension of the outer grid (x-direction)
z_b	Dimension of the outer grid (z-direction)

α_i	Start and end point angle
(ϑ, φ, R)	Spherical coordinates
ϑ_c	Azimuthal deviation
μ	Magnetic permeability
μ_0	Magnetic permeability of free space
ρ	Electrical resistivity
σ	Electrical conductivity
ϕ	Electrical potential
Φ	MMR sensitivity

Kurzzusammenfassung

Bei der magnetometrischen Widerstandsmethode (engl.: magnetometric resistivity, MMR) werden die Magnetfelder von in den Untergrund injizierten, niederfrequenten Strömen gemessen, um hieraus auf die Leitfähigkeitsverteilung im Untergrund zu schließen. Mit dem Ziel die MMR-Methode als bildgebendes Verfahren für Bohrloch-Bohrlochmessungen zu implementieren, wurden in der vorliegenden Arbeit verschiedene Aspekte des Messdesigns für oberflächennahe Feldanwendungen untersucht. In numerischen, Labor- und Feldstudien wurde das Potential der MMR-Methode für eine verbesserte strukturelle Charakterisierung und Prozessmonitoring auf der Feldskala analysiert. Der vorliegende 2D-Ansatz verwendet Bohrlochmessungen des Magnetfeldes bedingt durch Stromeinspeisung ebenfalls im Bohrloch; in diesem Fall hat das resultierende Magnetfeld nur eine von Null verschiedene Komponente (senkrecht zur Untersuchungsebene – B_y).

In numerischen Studien wurden anhand von Untersuchungen hinsichtlich des methodischen Signal-Rauschverhältnisses und Auflösungsvermögens optimale Messparameter bestimmt. Die Modellierung von MMR-Signalen über 2D Leitfähigkeitsverteilungen wurde dabei mit dem neu-entwickelten 2.5D FE-Programm *MMRMod* durchgeführt. Die Stromeinspeisung mittels eines vertikalen Dipols liefert das bestmögliche Signal-Rauschverhältnis. Die Analyse von Sensitivitätsverteilungen zeigt, dass mit Dipolkonfigurationen kleinräumige, begrenzte Untergrundbereiche erfasst werden (vorteilhaft für tomographische Untersuchungen), sowie dass Transmitter-Empfänger-Konfigurationen, die einen vertikalen Abstand größer als der Bohrlochabstand aufweisen, kaum zur Auflösung des Untersuchungsgebietes beitragen.

Mit Hilfe von Laboruntersuchungen konnten Verfahren entwickelt werden, mit Hilfe derer grundlegende Schwierigkeiten von MMR-Bohrlochanwendungen überwunden wurden: eine Transformation der Messdaten in ein Referenzkoordinatensystem und eine Methode zur Korrektur von Fehlern, die aufgrund parasitär korrelierter Störfelder entstehen können. Die (letzte) Messmethode mit Phasenumschaltung sowie moderne Lock-in-Technik ermöglichen eine effektive Informationsgewinnung aus den gemessenen Magnetfelddaten.

MMR-Daten wurden abschließend während eines Wasserinfiltrationsexperiments auf der Gorgonzola-Testfläche in Bohrloch-Bohrlochkonfiguration erfasst. Datenaufnahme und –verarbeitung wurden entsprechend dem entwickelten tomografischen Messansatz durchgeführt. Messdaten wurden vor (Hintergrund-) und während (Monitoringdaten) der Infiltration aufgenommen. Die Hintergrunddaten wurden mithilfe von Modellkurven, basierend auf verschiedenen Leitfähigkeitsmodellen, qualitativ ausgewertet und interpretiert. Der Vergleich von Feld- und Modelldaten deutet darauf hin, dass Leitfähigkeitskontraste besser mit der MMR-Methode als mit der klassischen geoelektrischen Erkundung aufgelöst werden können. Darüberhinaus zeigt die Analyse der Monitoringdaten, dass eine klare, zeitliche sowie räumliche Abhängigkeit zwischen MMR-Anomalie und Wassersättigung des Bodens besteht.

Abstract

The magnetometric resistivity (MMR) method measures low-level (typically $< 1\text{ nT}$) magnetic fields associated with a low-frequency ($1 - 20\text{ Hz}$) electric current impressed into the ground to determine the subsurface resistivity structure. As a step towards the implementation of MMR for cross-hole imaging, in this Ph.D. thesis several aspects of survey design for near-surface applications are discussed. In numerical, laboratory and field studies the potential of MMR for advanced structural characterization and process monitoring at the field scale is assessed. The 2D cross-hole setup considers borehole measurements of the magnetic field as response to borehole current injection; in this case the magnetic field has only one non-zero component (perpendicular to the imaging plane $-B_y$).

Optimal survey parameters are inferred from numerical studies regarding signal strength, source-generated noise level and resolving power. Modeling of MMR responses over 2D conductivity structures was performed using a newly developed 2.5D FE program MMRMod. It could be proven that current injection via vertical dipoles provides superior signal-to-noise ratio compared to other transmitter configurations. Analyzing resolving power in terms of sensitivity distribution reveals that dipole configurations reflect confined subsurface volumes, advantageous for tomographic surveys and that transmitter-receiver combinations exceeding an offset equal to the borehole separation do not contribute significantly to the overall cross-hole resolution.

With the assistance of laboratory testing two concepts for solving two major difficulties inherent in cross-hole MMR field surveying are derived: the correction for the arbitrary borehole sensor orientation and the correction for parasitic correlated noise fields induced by the measurement system itself. The (latter) measurement method with phase switching is thereby first-time successfully applied to the processing of MMR data. In addition, the proposed data processing procedure includes modern lock-in-technique and has proven to be an appropriate tool for an effective information extraction from the measured magnetic fields.

Finally, cross-hole MMR data were collected during a water infiltration experiment at the Gorgonzola test site. Acquisition and processing are accomplished according to the developed tomographic measurement approach involving multiple-offset transmitter-receiver arrangements and repeated measurements with time (time-lapse mode). Data, obtained during initially conducted background measurement, are qualitatively validated based on two different conductivity models, one of which is obtained from the inversion of independently collected ERT data. Importantly, the comparison of field data with predicted model curves suggests better resolvability of contrasts by MMR than by ERT. Moreover, the analysis of time-lapse measurements reveals a clear spatiotemporal dependence of the anomalous MMR response (MMR response with respect to background value) based upon the water saturation.

Table of Contents

1. Introduction	7
1.1. Objectives	9
1.2. Outline	10
2. Theory of the Magnetometric resistivity method	11
3. Conceptual model of cross-hole MMR	13
3.1. Historical development of borehole MMR	13
3.2. Model setup and transmitter configurations	15
4. The MMR forward problem	17
4.1. Analytical solution for the wire component B^w	19
4.2. Numerical solution for the wire component B^w	20
4.3. Analytical solution for the ground component B^g	22
4.4. Numerical solution for the ground component B^g	23
4.4.1. Modeling approach	23
4.4.2. Finite element implementation	24
4.4.3. Homogeneous test model	26
4.4.4. Layered test model	33
4.5. Sensitivity calculations	35
4.5.1. The MMR sensitivity	35
4.5.2. Calculation of sensitivity by perturbation approach	35
5. Numerical analysis of different transmitter configurations	39
5.1. Model response curves	40
5.1.1. Signal strength	41
5.1.2. Implication for tomographic surveys	43
5.1.3. Source generated noise	44
5.2. Sensitivity distributions	46
5.2.1. Homogeneous case	47
5.2.2. Inhomogeneous case	50
5.2.3. Sensitivity-based comparison of ERT and MMR	52
5.3. Concluding remarks	54
6. Developing of a data processing procedure	55
6.1. The MMR measurement system	56
6.1.1. Fluxgate sensor	57
6.1.2. Measuring frequency	58
6.2. Lock-in amplification	59
6.3. Borehole sensor orientation	60
6.4. Minimizing the error due to parasitic correlated noise fields	63

6.5. Reduction for the wire component	64
6.6. Validation of the data processing procedure – the “Tank Experiment”	65
7. Field Example	70
7.1. The Gorgonzola field site.....	70
7.1.1.Site description	70
7.1.2.Survey specification	71
7.2. Data validation of background measurements	74
7.2.1.Moving receiver	75
7.2.2.Moving source	77
7.3. Time-lapse Responses	80
8. Summary and Recommendation	87
A. Indexing scheme	91
B. Extended survey specification	93
B.1. Background survey	94
B.2. Time-lapse survey	95
C. Validation of background measurements	100
C.1.Moving receiver	100
C.2.Moving source	104
D. Time-lapse responses	109

Chapter 1

Introduction

The presence and flow of water in the shallow subsurface controls a number of phenomena of great environmental interest like mountain slope instability, floods and soil and groundwater contamination. A better understanding of these processes is necessary to guarantee a sustainable use of soils and aquifers as well as to maintain acceptable groundwater quality. Direct measurements of soil water content are strongly invasive as they require the recovery of soil samples. Moreover, the extraction of a soil core constitutes a major disturbance in the natural in-situ condition, supports only a small and localized volume of the subsurface and can not be repeated. The application of geophysical methods provides the opportunity of a non-invasive, spatiotemporal resolving assessment of the subsurface. Application of geophysical methods to the monitoring of flow and transport processes in the subsurface are studied in the relative new field of hydrogeophysics (Vereecken et al., 2004). For this use of geophysical data experience shows that cross-borehole acquisition provides the most informative results (e.g. Looms, 2008). Cross-hole arrangements are on a more appropriate scale, offer high spatial resolution and exhibit only minimal intrusion of the subsurface. An obvious advantage of the cross-hole measurements is the simple fact that boreholes provide greater access to the region of ground where physical properties are to be determined (Acosta & Worthington, 1983). In particular, signal path ways are shorter and hence, data quality is less affected by damping of the injected signal.

The successful use of geophysical data in hydrogeophysical investigations requires, after Deiana et al. (2005):

- that data are collected in time-lapse mode,
- that the resolution and sensitivity of the geophysical methods in space and time is fully understood,
- that the collected geophysical data have a clear, quantitative petrophysical relationship to environmental variables of interest.

Time-lapse mode refers to repeated measurements with time using the same acquisition geometry and is intended to capture the interaction of the static geological signal with the dynamic hydrological process. An often used proxy in studies related to the water saturation

is the electrical conductivity. In the early 1940's, Archie (see Archie, 1942) already established an empirical, petrophysical relation linking the (bulk) electrical conductivity to pore fluid conductivity, matrix material and porosity, later known as Archie law. The subsurface electrical conductivity (or its reciprocal the electrical resistivity) distribution is generally mapped in electrical (DC) or electromagnetic (EM) surveys. For the DC resistivity method (or its tomographic implementation: electrical resistance tomography ERT) a number of electrodes are placed along surface or borehole profiles (or both). Current is commonly injected via two so-called current electrodes. The resultant electrical potential is measured using another electrode pair, the potential electrodes. By using different geometrical combinations of current and potential electrodes information from different regions of the subsurface can be inferred. In electromagnetic surveys a transmitter coil is used to generate an alternating electromagnetic field, which in-turn generates electrical eddy currents in the subsurface. These eddy currents induce a secondary electromagnetic field interfering with the transmitted field. From amplitude and phase of the combined field, measured with a receiver coil, the subsurface conductivity can be derived. As highlighted by previous authors, ERT and ground-penetrating radar (GPR) have proven to be powerful tools in the field of hydrogeophysical characterization both on the so-called lysimeter (large soil monoliths) scale (Koestel et al., 2008) and on the field scale (e.g. Kemna et al., 2002; Tronicke et al., 1999).

In this Ph.D. thesis a third technique is considered to derive information on subsurface conductivity distribution – the magnetometric resistivity (MMR) method. From Maxwell's equations it is a fact that every current flowing through a medium is accompanied by a magnetic field. MMR takes advantage of that by alternatively measuring the magnetic field instead of the electric potential as in the DC resistivity method. Historically, the MMR method dates back to a patent by Jakosky (1933), but it met with little success experimentally at that time.

In practice, the MMR method is advantageous over the traditional DC resistivity measurements in that magnetic sensing does not require galvanic coupling like electric potential measurements. Thus, a flexible data acquisition with measurements in dry areas or plastic-cased boreholes is conceivable. MMR field measurements are less susceptible to perturbations by local resistivity variations near the measurement point (Asten, 1988). Supplementary, the MMR method benefits over the DC resistivity technique in that the masking effect of conductive overburden is reduced and distorting effects of surface topography is less prominent (Veitch et al., 1990). The location of the magnetic sensor below the ground surface partially shields the measurements from EM noise and thus improves the signal-to-noise ratio. In comparison to the measurement of the scalar potential inherent in DC resistivity, measurements of the magnetic field provide additional directional information on the location of a target due to measuring of a vector quantity. Although the advantages of the MMR method over the conventional DC resistivity method for certain subsurface situations and measurement geometries are known for long, the method has not yet been implemented to cross-hole imaging.

1.1. Objectives

The objective of this Ph.D. research project is to establish cross-hole MMR as tomographic technique. In addition, the study aims to characterize the applicability of cross-hole MMR for hydrogeophysical imaging at the field scale. Since a fully three-dimensional (3D) implementation is both a numerically as well as an experimentally extensive issue, the present research is limited to the tomographic investigation in two dimensions for the time being.

Monitoring in environmental investigations has typically focused on coupled interpretation of separate results, obtained from application of individual geophysical methods. Besides the conventional combinations of known geophysical methods, for instance ERT and GPR (Deiana et al., 2007; Looms, 2007), new technologies and approaches emerge, in particular the magneto-electrical resistivity imaging technique (MERIT). Terminologically, this extended approach combines the evaluation of electric and magnetic field data information induced by low-frequency current injection (see review Yaramanci et al., 2005). Kulesa et al. (2002) was the first to consider the simultaneous acquisition and joint inversion of ERT and MMR data in a more sophisticated imaging framework to monitor subsurface fluid flow. Due to the different sensitivity characteristics with respect to the direction of current flow, this emerging new technique is seen to be a promising approach to resolve subsurface flow and transport processes better than the individual methods ERT or MMR.

Previous investigations at the Research Center Juelich, in particular at the Institute Agrosphere (ICG 4) and the Central Institute of Electronics (ZEL), have focused on the implementation of MERIT at the soil column scale (approx. 0.5 m high), for instance Zimmermann et al. (2005) and Verweerd (2007). They numerically and experimentally proved that the addition of magnetic field data information leads to an increase in the resolving capability when compared to traditional ERT data. Using a fundamental inversion routine a considerable increase in resolution could be obtained in model scenarios where a shielding layer hides an anomalous object. Up scaling of the MERIT system to the field scale will be the next important step.

For mining applications, such a combined approach has already proven its usefulness, e.g. referring to Sub-Audio Magnetism (SAM) as proposed by Cattach et al. (1993) and later on pursued by Hashemi et al. (2005) and Whitford et al. (2005). Furthermore, Svoboda et al. (2002) started to build up an advanced technology for mapping subsurface water conductivity using combined surface magnetic field and borehole electric potential measurements.

Although MMR is considered as stand-alone technique in the following Ph.D. thesis, this research work shall be deemed to be a preliminary step within the scope of introducing MERIT to the field scale. The presented study describes three years of cooperative work between the Central Institute of Electronics (Zentralinstitut für Elektronik – ZEL) and the Agrosphere Institute, Institute for Chemistry and Dynamics of the Geosphere (Institut für

Chemie und Dynamik der Geosphere: Agrosphäre), both part of the Research Center Jülich in Jülich (Forschungszentrum Jülich GmbH). In particular, the prototype field instrumentation used in this study was developed at the ZEL. Moreover, Andreas Kemna (Department of Applied Geophysics, University of Bonn) contributed significantly to the success of this work by providing the 2.5D MMR forward modeling program MMRMod. Finally, Prof. Giorgio Cassiani (Department of Geophysics, University of Padua) assisted with the realization of the field studies (in 2006) by designing and organizing the field experiment on-site.

1.2. Outline

This thesis will start by introducing the magnetometric resistivity method and particularly its cross-hole variant through the description of the governing equations and the general MMR convention in chapter two as well as the conceptual model of the considered 2D setup in chapter three. In addition a short historical overview of the development of borehole MMR will be given. The fourth chapter will deal with the formulation of the MMR forward problem. This chapter comprises the numerical methods, used to predict the different components of the MMR response. Furthermore, the numerical solutions, obtained for simple geometries, are tested against analytical solutions in order to verify modeling accuracy of the implemented algorithms. In the fifth chapter, a numerical study for the optimum transmitter configuration is presented. Synthetic data will be used to evaluate the different configurations in terms of signal strength, source-generated noise and resolution power. Finally, by means of resolving power with respect to a fixed cube, the complementary character of the MMR and ERT is demonstrated. The sixth chapter will treat the development of a proper data processing procedure. Since the MMR measurement system, designed for the tomographic investigation in boreholes, is completely new and processing of magnetic field data imposes several requirements, several technical developments had to be made in order to obtain good data quality. In addition, the measurement system and in particular the developed data processing routine is tested against numerical solutions available for a simple laboratory experiment. The seventh chapter describes a MMR field application, used to monitor a water infiltration experiment at the Gorgonzola test site (Italy). MMR data, acquired during initial background measurements, are qualitatively validated based on two conductivity models, one of them obtained from the inversion of independently acquired ERT data. Time-lapse MMR measurements are discussed and analyzed in terms of the anomalous MMR response caused by the water body. A summary and recommendations for future research on cross-hole MMR are discussed in chapter eight.

Chapter 2

Theory of Magnetometric resistivity

In this chapter, the theoretical foundations of the magnetometric resistivity (MMR) method and the basic MMR convention are introduced. The MMR method considers measurements of low level (typically < 1 nT) magnetic fields as a response to a low-frequency (1 – 20 Hz) current impressed into a subsurface volume via grounded electrodes. The evaluation of magnetic field measurements is used in order to obtain information on the subsurface resistivity distribution.

The Biot-Savart law relates the magnetic field $\mathbf{B}(\mathbf{r})$ at a point external to a volume V containing an arbitrary current distribution $\mathbf{j}(\mathbf{r}) d\mathbf{v}'$ and is given by the integral relationship

$$\mathbf{B}(\mathbf{r}) = \frac{\mu}{4\pi} \int \frac{\mathbf{j}(\mathbf{r}') \times (\mathbf{r} - \mathbf{r}')}{|\mathbf{r} - \mathbf{r}'|^3} d\mathbf{v}' \quad (2.1)$$

with no restriction on the form of the current density $\mathbf{j}(\mathbf{r})$. Here, μ denotes the magnetic permeability, and $|\mathbf{r} - \mathbf{r}'|$ is the distance between the volume element $d\mathbf{v}'$ and the measurement point. For hydrogeophysical applications, magnetization effects can be generally neglected and thus $\mu = \mu_0 = 4\pi \cdot 10^{-7} \text{ Vs/(Am)}$ can be assumed. Furthermore, we assume Ohm's law (2.2) to be obeyed within the considered volume V with

$$\mathbf{j}(\mathbf{r}') = \sigma(\mathbf{r}') \nabla' \phi(\mathbf{r}') \quad (2.2)$$

where $\sigma(\mathbf{r}')$ and $\phi(\mathbf{r}')$ are the electrical conductivity and electric potential, respectively. Edwards et al. (1978) used Stoke's theorem and some vector identities in order to reduce the volume integral to a set of surface integrals. The Biot-Savart law is hereby modified to the form (2.3)

$$\mathbf{B}(\mathbf{r}) = \frac{\mu}{4\pi} \int \frac{\nabla' \phi(\mathbf{r}') \times \nabla' \sigma(\mathbf{r}')}{|\mathbf{r} - \mathbf{r}'|^3} d\mathbf{v}' \quad (2.3)$$

This is a very useful expression for computing MMR responses, as it contains $\nabla' \sigma(\mathbf{r}')$, which is likely to become zero everywhere except at the surfaces defining units of different

conductivity. The equation (2.3) also reveals the important fact that $\mathbf{B}(\mathbf{r})$ only contains information on conductivity changes – absolute values are inaccessible. In the present study, only spatial variations in two dimensions are assumed, i.e. current sources are in-plane with magnetic sensors (x-z-plane) with a conductivity structure striking in the y-direction. With such an approach, the resulting magnetic field only has one non-zero component, B_y .

A concept that attempts to measure the magnetic field caused by non-inductive current flow, induced by using signal electrodes, will be influenced by those (same) currents in the signal leads connecting the signal electrodes. It is not possible to separate the desired component of the magnetic field from the data using only the field measurements. In summary, MMR responses are, in practice, always a superposition of a magnetic field due to both a wire current B^w and a current in the ground B^g . However, if the current strength I and the exact layout of the signal cables are known, it is possible to estimate the wire contribution and then subtract it from the measurement values (*see* Chapter 5, 6). The interfering magnetic field of the wires delivering the current to the electrodes is likewise obtained from the Biot-Savart law by integration along the involved wires,

$$\mathbf{B}^w(\mathbf{r}) = \frac{\mu_0 I}{4\pi} \int \frac{d\mathbf{l}' \times (\mathbf{r} - \mathbf{r}')}{|\mathbf{r} - \mathbf{r}'|^3} d\mathbf{r}' \quad (2.4)$$

where the vector $d\mathbf{l}'$ represents an infinitesimal wire segment. Following the MMR convention (Chen et al., 2002b), the ground component B^g can be split up, in turn, into a fraction caused by primary current flow in a uniform half-space B_p^g , frequently referred to as the normal magnetic field, and a fraction B_s^g provoked by secondary (or perturbed) current flow due to conductivity anomalies. This part exclusively contains information on the underlying conductivity distribution. The secondary magnetic field B_s^g is synonymous with anomalous MMR response in the following. In order to access this information, measured magnetic fields B^m , associated with low-frequency current injection, have to be primarily reduced in accordance to the following formula:

$$B_s^g = B^m - B^w - B_p^g \quad (2.5)$$

Estimations of the wire contribution and background fields are therefore essential in MMR data processing. Thus, the computational methods for their prediction are comprehensively discussed in Chapter 4.

Chapter 3

Conceptual model of cross-hole MMR

In this chapter, the conceptual model of the considered cross-hole approach is described. The cross-hole variant of the MMR method uses two boreholes in the vicinity of a conductive or resistive target, in order to obtain information on the cross-hole resistivity distribution.

To begin with, a short history of the development of borehole MMR, both of theoretical and practical nature is given. Secondly, the conceptual 2D model and the transmitter configurations considered for low-frequency current injection are described.

3.1. Historical development of borehole MMR

The MMR method has been known since the early 1930's, but field experiments had only little success at that time. Part of the problem was concerning the instrumentation, as the first measurements were carried out with free-hanging bar magnets or vibrating strings. Developments of magnetometers with having sufficient sensitivity sparked a revival of the idea in the 1970's. The first MMR field experiments were all predominantly directed toward surface exploration (Edwards, 1974; Edwards & Howell, 1976), with both current electrodes and magnetic sensors located on the surface of the Earth. The traditional horseshoe measurement layout (Fig. 3.1a), first-time proposed by Jakosky (1933), has basically remained the same over the years and recently proved to be an appropriate configuration for the detection of contaminant plumes (Kaiguang & Jianwen, 2008). Besides surface exploration, it soon became apparent that lowering either magnetic sensor or current electrodes into a borehole make it possible to overcome the limitations of the surface MMR method, e.g. insensitiveness to 1D layering.

Throughout literature, the incorporation of boreholes into MMR measurements is named differently. Referring to the concept of borehole MMR (Acosta & Worthington, 1983), downhole MMR (e.g. Asten, 1988) or drillhole MMR (e.g. Bishop et al., 1997) do not necessarily indicates that current is injected via subsurface sources. In particular, downhole and drillhole MMR (DHMMR) applications usually employ a surface dipole for the current injection (Fig. 3.1b). In this thesis, only cross-hole MMR explicitly denotes that both magnetic sensors and transmitter electrodes are employed below the Earth's surface.

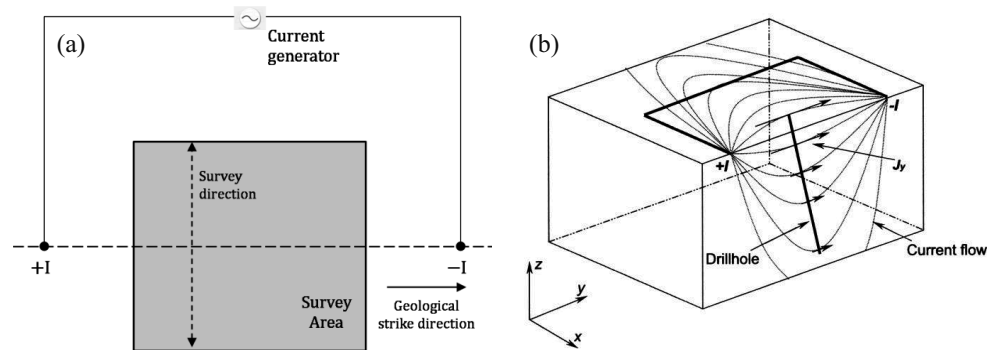


Figure 3.1. MMR survey layouts (a) traditional “Horsehoe” layout for surface exploration (redrawn after Fathianpour et al., 2005) (b) DHMMR setup (Purss et al., 2003)

A first borehole MMR field experiment was reported by Nabighian & Oppliger (1980). At the same time, Acosta & Worthington (1983) described the method used in correlation to a hydrogeological problem. They were the first to announce the advantage of the MMR method over traditional DC resistivity method for the detection of localized current flow within an otherwise non-conducting environment, thus making the method ideal for hydrogeophysical applications. The theoretical cross-hole MMR responses of a disc conductor (Edwards, 1984) and half-plane conductor (Pai & Yeoh, 1987), respectively, were derived in order to serve as interpretational aids for the mineral exploration. The conductive disk and half-plane conductor thereby represent simple models of either a lamellar mineral deposit or an orebody. Nabighian et al. (1984) presented the theoretical basis which included the current channeling number and induced polarization effect of the cross-hole MMR method in a unified format.

Veitch et al. (1990) pointed out the general solution for the magnetic field within a layered earth due to a point source. The type curves of Veitch et al. (1990) have basically remained the best published references for real cross-hole MMR applications. Unfortunately, Veitch et al. (1990) only considered subsurface pole sources.

In the time ranging from the end of the 1980’s to beginning of the 2000’s, DHMMR became a popular method (at least in Australia) for the detection of weakly conductive mineralization, such as nickel, sulphides or gold. DHMMR surveys are typically conducted by setting up one grounded dipole at the surface – oriented parallel to the strike direction while the magnetic sensor is lowered in a drillhole in order to record the magnetic field. This technique was primarily adopted complementarily to the DHTM (Drillhole time-domain electromagnetic) method. While DHTM becomes insensitive for the mapping of very poor or strong conducting bodies, DHMMR remains an efficient method in that case (Purss et al., 2003). Due to the combined use, DHMMR surveys have historically relied on the use of TEM probes to measure the local magnetic response from the galvanic current (e.g. Acosta & Worthington, 1983; Asten, 1988; Bishop et al., 1997, 2000; Stolz, 2003; Elders & Asten, 2004).

Unfortunately, this fact negatively affects the quality of data obtained (Purss & Cull, 2003). The main disadvantage is that TEM probes work best with a frequency range of 1-2 kHz, whereas frequencies in traditional MMR surveys vary from 1 to 25 Hz. The second impediment is that numerical manipulation is needed in order to transfer measured dB/dt values (common TEM probe output) into real B-field values. Only by advances in magnetic field sensor design it was possible to overcome such limitations, for instance modern magnetic field sensors are capable to be used in typical exploration drillholes. More recently, DHMMR has additionally been extended to simultaneously analyze both the amplitude and the phase of the measured magnetic fields (Purss et al., 2003).

3.2. Model setup and transmitter configurations

A typical 2D cross-hole situation is described by two vertical profiles representing two adjacent boreholes. Fig. 3.2(a) schematically illustrates the considered 2D cross-hole setup.

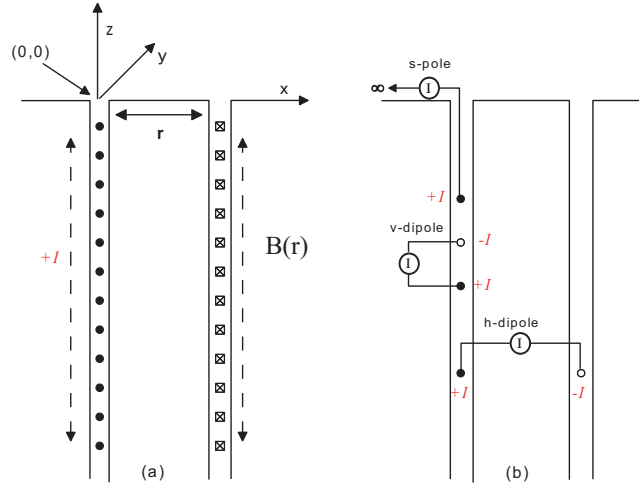


Figure 3.2. General model setup (a) and transmitter configurations (b) considered in the concept of 2D cross-hole MMR. Transmitter electrodes (+I) and magnetic sensors are indicated as circles and squares. Additional sink electrodes (-I) are displayed as open circles.

For simplicity, we assume the boreholes to be straight and position them on the x-axis. The effect of the borehole (required in practice to lower the magnetic sensor into the ground) on the magnetic response is ignored and all current sources are idealized to point sources. In order to perform high-resolution imaging with MMR, one borehole (the so-called transmitter borehole A), is equipped with an electrode array, while a magnetic sensor or sensor array samples the magnetic field at various positions in the receiver borehole B.

In order to comprehensively analyze the impact of different transmitter configurations on data acquisition in cross-hole MMR surveys, we consider both pole and dipole subsurface current

sources. In the case of using only a single current electrode, (referred to as *s-pole* configurations), the current sink is assumed to be at infinity (towards negative x-direction). Generally, in electrical cross-hole surveys, dipole current injection is feasible by placing both electrodes either in the same or in different boreholes. As the first electrode arrangement forms a vertical dipole and the second a horizontal one, they are labeled as *v-dipole* and *h-dipole* configurations. While the dipole length of *h-dipole* configurations is fixed and pre-determined by the borehole separation r it is variable for *v-dipole* configurations. A larger dipole length is likely to generate higher signal strength; it reduces the total number of possible configurations, which in-turn will reduce the overall cross-hole resolution. Thus, the optimal dipole length will result from a balance between minimally detectable signal amplitude and best resolution (*see* Chapter 5). The three transmitter configurations considered for current injection are schematically illustrated in Fig. 3.2b.

Chapter 4

The MMR forward problem

The forward problem in magnetostatics is defined as the calculation of the magnetic field generated by an internal current pattern for given boundary conditions, injected current positions and a known conductivity distribution. In MMR terminology, the magnetic field represents the measured data, generally denoted with data vector \vec{d} . The conductivity distribution, more precisely the conductivities of all considered cells or elements composing the imaging region, represents the model parameters, which are summarized in the model vector \vec{m} .

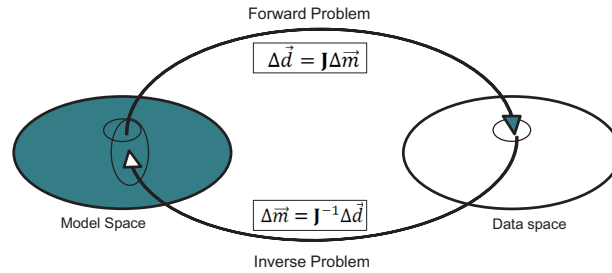


Figure 4.1. Relation of model and data space via forward and inverse modeling. \mathbf{J} represents the Jacobian or sensitivity matrix, respectively.

The goal of all electrical methods is to obtain an image of subsurface electrical conductivity distribution from the measured data. This is commonly referred to as the inverse problem. Therefore, a forward modeling algorithm needs to be developed in order to implement it in the inversion scheme. In addition, the forward problem formulation can be used to supply simulation data. In the present study, forward modeling is used to optimize the data acquisition (Chapter 5) and to enable a qualitative interpretation of actual field measurements (Chapter 7). The sensitivity of the MMR method is an essential property in both forward and inverse problem, as it provides a link between the data and the model vector in terms of the Jacobian matrix \mathbf{J} . As such, the sensitivity represents a substantial and meaningful quantity in any data interpretation process.

This chapter focuses on the numerical solutions, obtained for both MMR components, as well as on the present implementation of these solutions. From the numerical point of view, both MMR components B^g and B^w can be computed separately. Whereas the analytical solution and numerical implementation for the wire component are rather simple, the calculation of the ground component is more complex.

Generally, the calculations of MMR responses over a conductive structure can be roughly grouped into three categories. The first one is based on the derivation of an analytical solution for a small number of simple structures. In case of cross-hole MMR, these structures include a uniform half-space (Nabighian et al., 1984), a layered earth (Veitch et al., 1990), and a half-plane conductor (Pai & Yeoh, 1987). The second category uses the surface integral equation method for forward modeling. For some simple problems, the gradient of the electrical conductivity vanishes everywhere except on the boundaries of units with distinct conductivities. Thus, the volume integral for the modified Biot-Savart law is reduced to a finite number of surface integrals. Gomez Trevino & Edwards (1978) developed a rapid algorithm in order to compute all three components of the magnetic field over a 2D structure. Nabighian et al. (1984) and Cheesman & Edwards (1989) used such a procedure to compute the MMR response associated with multiple finite plates of arbitrary conductance. The last category of forward modeling strategies is based upon the modification of a “numerical resistivity” method (Edwards & Nabighian, 1991). Since this type of computation is used in this study, it is described more extensively in section (4.4). An adaptation for 2D imaging purposes was first proposed by Pai & Edwards (1983) and later on pursued by Kemna et al., (2003) and Fathianpour et al. (2005), respectively. An adaptation for three-dimensional modeling of Total Field MMR (TFMMR) responses over arbitrary 3D structures was reported by Boggs et al. (1999). Alternatively, to calculate the MMR response via the modified Biot-Savart law (2.3), a differential equation for the magnetic vector potential may be evaluated from which the MMR response is obtained likewise (Haber, 2000).

For the verification of the numerical solution (4.2 and 4.4), analytical solutions were derived for simple systems (4.1 and 4.3) to represent both components B^w and B^g . These simple systems are a straight finite wire (wire component) and a homogeneous half-space (ground component). Furthermore, the numerical solution for a layered half-space is compared to published results (subsection 4.4.4.).

As an essential, initial step of the forward problem the generation of an appropriate model space and in case of numerical modeling a finite differences or finite element grid is required. Hence, modeling accuracy is investigated for a number of different grids representing the homogeneous test model (subsection 4.4.3). The geometry of this test model is the standard model of investigation in this work, particularly when referring to the numerical analysis of different transmitter configurations (Chapter 5) and for the field example (Chapter 7). Finally, in the last section the theoretical basics and numerical implementation of the MMR sensitivity computation are described.

4.1. Analytical solution for the wire component B^w

The formulation of the analytical solution for the magnetic field of the wire delivering current to the grounded electrodes follows the idea of Fathianpour (1997). A thin wire is considered (Fig. 4.2) with cross-sectional area S and extending from z_1 to z_2 in z -direction used to derive the analytical solution.

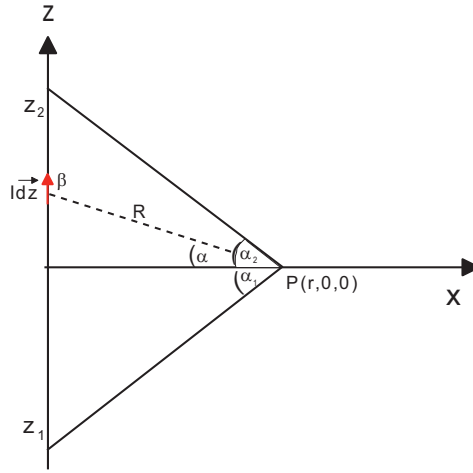


Figure 4.2. Geometry used to derive the magnetic field at point $P(r,0,0)$ caused by a current carrying wire (strength I . Start and end points are indicated by z_1 and z_2 as well as α_1 and α_2 .

The observation point is set on the x -axis with distance r from the wire. Provided that the current flows entirely along the wire, the current density is assumed to be constant across S .

$$dv' = dS' \cdot dz' \quad (4.1)$$

$$\int_V j dv' = \int_{z_1}^{z_2} dz' \int j dS' \quad (4.2)$$

$$= \int_{z_1}^{z_2} I dz' \quad (4.3)$$

With the relations (4.1) – (4.3), the Biot-Savart law (2.1) can be reduced to a line integral

$$\mathbf{B}(r) = \frac{\mu_0 I}{4\pi} \int_{z_1}^{z_2} \frac{dz' \times \mathbf{R}}{R^3} \quad (4.4)$$

where $R = \sqrt{r^2 + z'^2}$.

The cross product $(\mathbf{dz}' \times \mathbf{R})$ points in the y-direction and its absolute value is evaluated as

$$|\mathbf{dz}' \times \mathbf{R}| = dz \cdot R \cdot \sin(\mathbf{dz}', \mathbf{R}) = dz \cdot R \cdot \sin(\beta) = dz \cdot R \cdot \cos(\alpha) \quad (4.5)$$

Here, the fact is used that sine and cosine function exhibit a phase shift of 90 degrees. In order to obtain the result in terms of the parameter α depending only on the final positions of the wire, the following relations are introduced

$$z = r \cdot \tan(\alpha) \quad dz = r(1 + \tan^2(\alpha))d\alpha \quad R^2 = r^2(1 + \tan^2(\alpha)). \quad (4.6)$$

Substituting these relations into equation (4.4) yields for the y-component:

$$B(r) = \frac{\mu_0 I}{4\pi r} (\sin(\alpha_2) - \sin(\alpha_1)) \quad (4.7)$$

This last equation shows that to calculate the magnetic field caused by current flowing along a straight wire only the coordinates of the measuring point and the end points of the wire are required. For the often needed case of a semi infinitely long wire, e.g. extending from origin to infinity, a value of $\pm\pi/2$ is adopted for the appropriate angle, resulting in

$$B(r) = \frac{\mu_0 I}{4\pi r}. \quad (4.8)$$

4.2. Numerical solution for the wire component B^w

To obtain the numerical solution, the integral equation (4.4) is transferred into a finite sum. The magnetic field due to the wire current is now expressed as the sum of fields contributed by finite current elements $I \cdot \mathbf{dz}_i$

$$\mathbf{B}(r) = \frac{\mu_0 I}{4\pi} \sum_i^N \frac{\mathbf{dz}_i \times \mathbf{R}_i}{R_i^3} \quad (4.9)$$

For this purpose, the wire is described by $N + 1$ supporting points with z_i . A single segment is fully described by the following expressions

$$\mathbf{dz}_i = \begin{pmatrix} 0 \\ 0 \\ z_i - z_{i-1} \end{pmatrix} \quad \mathbf{R}_i = \begin{pmatrix} -r \\ 0 \\ \frac{z_i + z_{i-1}}{2} \end{pmatrix}$$

The y-component of the magnetic field, obtained for a single wire segment i , is evaluated as:

$$B_{y_i} = \frac{2\mu_0 I}{r} \frac{r(z_i - z_{i-1})}{(4r^2 + (z_i - z_{i-1})^2)^{3/2}}. \quad (4.10)$$

In order to test the numerical implementation and to determine the correct discretization size of the wire segments, a simple test model is adopted (Fig. 4.3). The magnetic field with depth is computed according to a wire of finite length $2 \cdot l$, flush with the surface and with current flow in the positive x-direction.

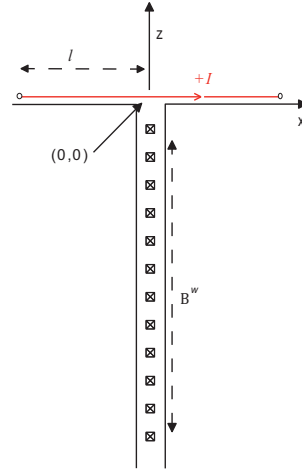


Figure 4.3. Geometry of the wire test model. To test the numerical solution for B^w a surface wire of length $2 \cdot l$ carrying current $+I$ is assumed. The magnetic field is measured with depth.

The displacement r of the measuring point from the wire is equivalent to the depth of the sensor. Besides the optimal discretization of the wire, the impact of the displacement of the measuring point from the wire on modeling accuracy is investigated. Therefore, a magnetic sensor is inserted at depths ranging from 0.01 m to 10 m and the results are displayed in a logarithmic plot (Fig. 4.4).

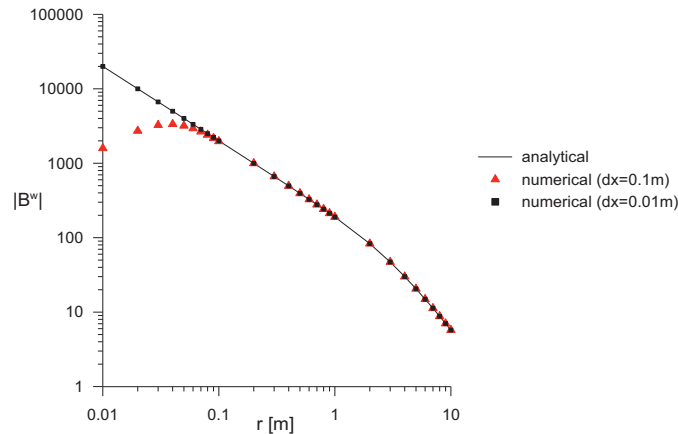


Figure 4.4. Variation of the MMR wire contribution B^w (absolute value) with discretization size dx and displacement r of the measuring point from the wire.

From the inspection of Fig. 4.4, a discretization of the wire with 0.01 m seems to be sufficient if a minimal wire-sensor displacement of 0.01 m is considered. Furthermore, the numerical approach permits a simple implementation of angled or even more complex wire layouts

4.3. Analytical solution for the ground component B^g

The number of analytical MMR solutions available for 2D cross-hole geometries is limited. The analytical solution for a magnetic field due to primary current flow in a homogeneous half-space B_p^g will be derived below. The magnetic field due to a subsurface source at depth d can be expressed by employing equivalent current filaments, as proposed by Nabighian et al. (1984). According to the filament model, B_p^g is equivalent to the magnetic field produced by a current filament of strength I which flows downward from infinity to a height d above the ground surface.

By considering equation (4.7) and using $\alpha_1 = -\pi/2$ as well as

$$\sin \alpha_2 = -\frac{z+d}{\sqrt{r^2+(z+d)^2}}, \quad (4.11)$$

the following expression is yielded:

$$B_p^g(r, z) = \frac{\mu_0 I}{4\pi r} \left(1 - \frac{z+d}{\sqrt{r^2+(z+d)^2}} \right). \quad (4.12)$$

Chen & Oldenburg (2004) proved the validity of this expression by deriving a general expression for the magnetic field due to a semi-infinite source in a 1D earth using a Hankel transform pair. They also pointed out that this expression is consistent with the solution obtained by Veitch et al., (1990) employing the image method.

The magnetic field due to a subsurface dipole is simply obtained by superposition of the two solutions obtained for pole sources of opposite polarity. If an *h-dipole* configuration, with $r = 0$ for the sink electrode is considered, equation (4.12) represents the analytical solution for this particular case. In case of a *v-dipole* configuration, with electrodes of opposite polarity buried at depths d_1 and d_2 , assuming furthermore that d_1 is supplied with a positive current, the magnetic field due to current flow in a uniform half-space is given by:

$$B_p^g(r, z) = \frac{\mu_0 I}{4\pi r} \left(\frac{z+d_2}{\sqrt{r^2+(z+d_2)^2}} - \frac{z+d_1}{\sqrt{r^2+(z+d_1)^2}} \right) \quad (4.13)$$

4.4. Numerical solution for the ground component B^g

4.4.1. Modeling approach

As already indicated, an adaptation of the “numerical resistivity” method as proposed by Edwards & Nabighian (1991) is used to compute the MMR ground response for a given conductivity distribution $\sigma(\mathbf{r})$. This type of forward modeling generally involves two steps. First, the well-known electrostatic problem defined by the Poisson equation (4.14) has to be solved for the electric potential $\phi(\mathbf{r})$ with \mathbf{r}_s denoting the source location.

$$\nabla \cdot (\sigma(\mathbf{r}) \nabla \phi(\mathbf{r})) + I \delta(\mathbf{r} - \mathbf{r}_s) = 0 \quad (4.14)$$

The second step is to calculate the magnetic field according to the modified Biot-Savart law (2.3). Yaramanci et al. (2005) pointed out that a straightforward implementation of this approach may be a computationally intensive task, as an evaluation of two three-dimensional convolution integrals for each component of the magnetic field would be necessary. A more efficient approach is to calculate the magnetic field in the wavenumber domain, where the convolution operator is reduced to simple multiplication. As conductivity is constant in strike direction y , the electrostatic problem (4.14) can be solved in the corresponding wavenumber domain for a Fourier transformed potential,

$$\tilde{\phi}(x, k, z) = \int_0^\infty \phi(x, y, z) \cos(ky) dy \quad (4.15)$$

with wavenumber k . Thus, for the first step of the calculation, standard two-dimensional finite-differences (FD) or finite-element (FE) solvers can readily be used. After having determined the electric potential distribution, the modified Biot-Savart law is formulated in the wavenumber domain as well by taking the Fourier transform of the magnetic field. By expanding equation (2.3) and taking the Fourier transform in the y -direction, the following integral, for the B_y component is obtained:

$$\begin{aligned} \tilde{B}_y(x, k, z) = & \frac{\mu_0}{4\pi} \int_{-\infty}^0 \int_{-\infty}^\infty \left(\frac{\partial \tilde{\phi}(x', k, z')}{\partial z'} \cdot \frac{\partial \sigma(x', z')}{\partial x'} \right. \\ & \left. - \frac{\partial \tilde{\phi}(x', k, z')}{\partial x'} \cdot \frac{\partial \sigma(x', z')}{\partial z'} \right) FT \left[\int_{-\infty}^\infty \frac{dy'}{|\mathbf{r} - \mathbf{r}'|} \right]. \end{aligned} \quad (4.16)$$

where FT stands for Fourier transformation. Note that the values of B_x and B_z are both zero in the xz -plane for structures striking in the y -direction, as discussed in Chapter 2.

By substituting the following relationship (Erdélyi et al., 1954)

$$FT \left[\frac{1}{\sqrt{(x-x')^2 + y^2 + (z-z')^2}} \right] = 2K_0(ks) \quad (4.17)$$

in which $s = \sqrt{(x-x')^2 + (z-z')^2}$ and K_0 is the modified Bessel function of order zero, into equation (4.16) the final equation for B_y of the MMR ground component in the wavenumber domain is yielded

$$\begin{aligned} \tilde{B}_y(x, k, z) = \frac{\mu_0}{2\pi} \int_{-\infty}^0 \int_{-\infty}^{\infty} & \left(\frac{\partial \tilde{\phi}(x', k, z')}{\partial z'} \cdot \frac{\partial \sigma(x', z')}{\partial x'} \right. \\ & \left. - \frac{\partial \tilde{\phi}(x', k, z')}{\partial x'} \cdot \frac{\partial \sigma(x', z')}{\partial z'} \right) K_0(ks) dx' dz'. \end{aligned} \quad (4.18)$$

This expression, along with electric potential in equation (4.15), forms the basic equation for calculating the 2D MMR ground response in wavenumber domain. Equation (4.18) reveals the efficiency of the present approach, since the calculation of the transformed magnetic field reduces to a set of numerical line integrations of the transformed potentials over the boundaries of all conductivity anomalies. Results in the spatial domain are obtained by taking an inverse Fourier transformation for the magnetic field calculated for a set of strategically chosen wavenumbers.

4.4.2. Finite element implementation

For the computation of the ground component, the 2.5D MMR forward modeling program MMRMod developed by Kemna (personal communication) is used. The implemented algorithm involves a 2.5D FE approximation to the transformed electric potential $\tilde{\phi}(x', k, z')$, followed by a discrete evaluation of equation (4.18) on a regular grid. The FE formulation is based on the existing 2.5D resistivity modeling software CRMod by Kemna (2000), developed in order to predict DC or IP responses, respectively. The principle of the FE method is to replace an entire continuous domain by a number of subdomains in which the unknown function is represented by simple interpolation functions with unknown coefficients. In particular, functions denote here the electrical conductivity distribution. In this way, the solution of the whole system is approximated by a finite number of unknown coefficients (Jin, 1993). As an essential initial step of any FE analysis, a discretization or subdivision of the domain is needed. The design of the discretized model or grid will significantly affect the required computer storage, the computational time and the accuracy of the numerical results. The first step is to select a region large enough so that the considered boreholes are located inside of this central region. Grid texture is fine within this central region and elements are distributed evenly. Secondly, a boundary region has to be added away from the central region in order to satisfy boundary conditions. Thus, element size in both vertical and horizontal

directions is increased almost exponentially toward the bottom and side boundaries. In methods employing a galvanic current source, there is no need to discretize the air region as no current will flow in this region. Fig. (4.5) schematically shows the grid type used for the computation of MMR responses over 2D conductivity structures in this study.

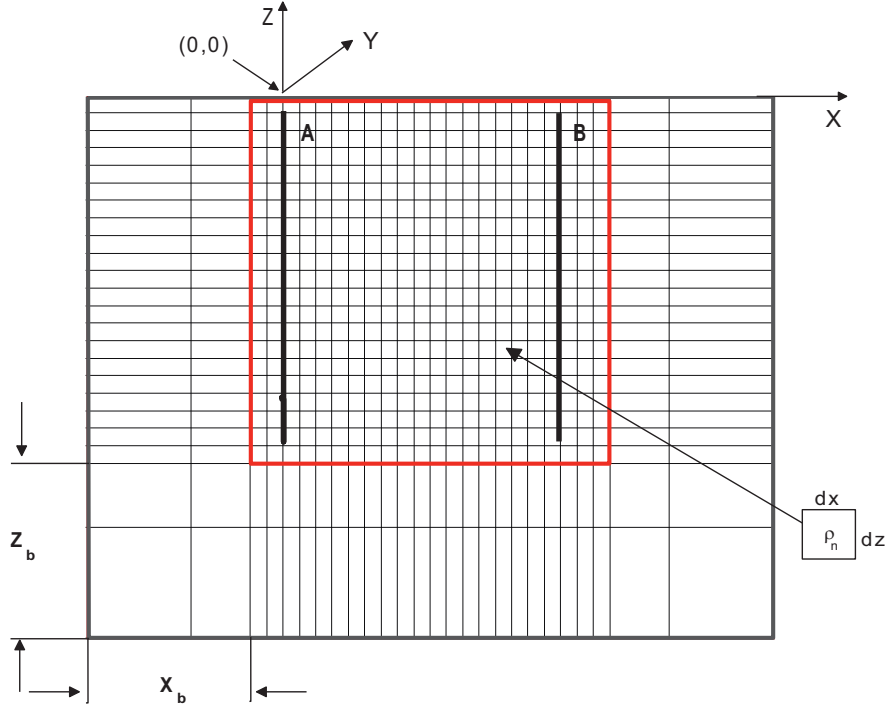


Figure 4.5. General FE grid used in 2.5D forward modeling. The red frame marks the central grid and encloses the boreholes A and B, whereas x_b and z_b describe the boundary grid. The element size in the central region is explicitly given by dx and dz .

Since MMR is a volume method, the contribution of conductivity gradients even outside the boundary grid, to the integral in (4.18) cannot be neglected, particularly not for the earth-air interface. To account for that fact, an additional term is introduced in the calculation of the MMR response which is based on the asymptotic behavior of the electric potential according to the employed mixed boundary conditions:

$$\sigma \frac{\partial \tilde{\phi}}{\partial n} + \beta \tilde{\phi} = 0 \quad (4.19)$$

Furthermore, the conductivity is assumed to proceed outside the grid. A more comprehensive description is given in Kemna et al. (2008). In the following, the modeling accuracy of the MMRMod program is checked with two models: a homogeneous and a layered test model.

4.4.3. Homogeneous test model

Since the geometry of the homogeneous test model represents the standard model of investigation in this work, numerical and analytical results obtained over a homogeneous half-space of $\rho_0 = 1 \Omega \cdot m$, are compared for a number of different grids and varying depths of investigation. The model contains 24 current electrodes in the transmitter borehole A and 24 magnetic sensor positions in the receiver borehole B. Borehole separation r is specified as 6.65 m, which refers to the field site described in Chapter 7. Electrode and sensor positions are distributed equally, ranging from -1.6 m to -20 m resulting in a vertical displacement of 0.8 m (Fig. 4.6).

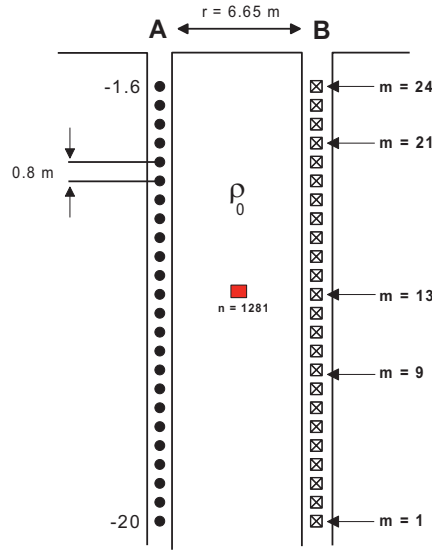


Figure 4.6. Geometry of the homogeneous test model. Transmitter electrodes and magnetic sensor positions are indicated by circles and crossed squares, respectively. Index m denotes the depths of investigation used to verify modeling accuracy and sensitivity modeling. Red square indicates the positions of arbitrary chosen element for the perturbation tests.

Furthermore, for the *h-dipole* configurations the current sink electrodes are assumed to occupy the same positions as the magnetic sensors. Anticipating the actual investigation regarding signal strength (see section 5.1.1), a dipole length of 2.4 m for the *v-dipole* configuration is considered. Because of the large number of different transmitter-receiver combinations, the spatial location of both is indicated by indexing schemes. In the following sections, l will be used for the transmitter, m for the receiver and n for the resistivity block index. While l and m are counted in the positive z -direction, the block index n starts in the upper left corner of the finite element grid.

Due to the fact that electrodes have to be on grid nodes, restrictions on discretization of the central region are induced horizontally by the borehole separation and by the vertical electrode or sensor displacement. Thus, the actual element size is a fraction of 6.65 m (x -direction) and 0.8 m (z -direction). Furthermore, the element size within the central region shall preferably be equal in both the horizontal and vertical direction to avoid potential introduction of anisotropic current channeling caused by the discretization. As potential element size $dx = 0.3375$ m and $dz = 0.4$ m (type B) as well as $dx = 0.16875$ m and $dz = 0.2$ m (type C) are chosen. First, both types are compared assuming a fixed boundary grid. The difference between numerically computed and analytical values is shown in Fig. 4.7 for an arbitrary chosen response curve ($l = 13$, fixed).

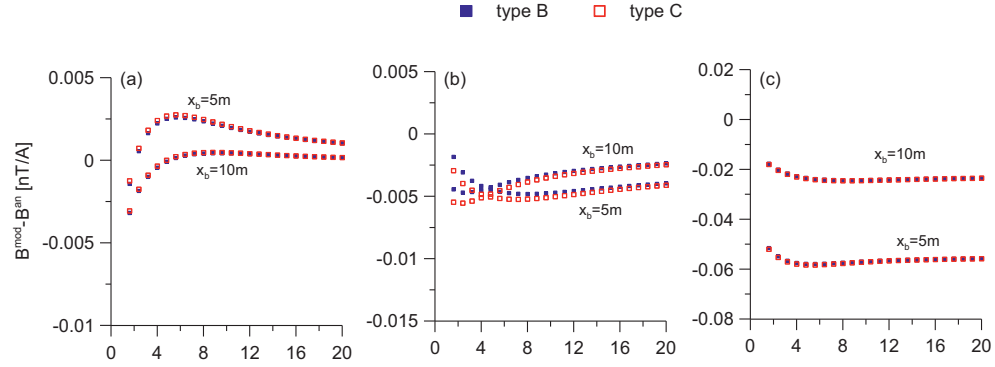


Figure 4.7. Comparison of modeling errors obtained for grid type B and C. The differences between numerically modelled and analytical values for arbitrary chosen transmitter configuration ($l = 13$, fixed) is displayed for (a) v -dipole, (b) h -dipole and (c) s -pole.

From the analysis of these error plots (Fig. 4.7), it becomes apparent that the fine discretization of type C does not result in a significant improvement of modeling accuracy. Therefore, the further investigation focused on the dimension of the boundary grid. Type B was chosen to investigate its impact on modeling accuracy. The outward extension, symmetrically for bottom and side boundaries, was increased from 5 m (grid B5) to 100 m (grid B100), while proportionally increasing the number of cells N_b . Specifications of all considered grids are summarized in Table 4.1.

The largest modeling errors are most likely to be obtained at most-distant points from the current source, as reported by Fathianpour et al. (2005a). Therefore, as depths of investigation the top and bottom end of the borehole are chosen. In addition, an intermediate depth ($l, m = 13$) is employed in order to investigate the progression of modeling errors away from the boundaries of the grid. Fig. 4.8, 4.9 and 4.10 illustrate the modeling accuracy for all three transmitter configurations, separately. First, the variation of B_p^g with depth of the magnetic sensor is shown in subfigures (a), (d) and (g). Since there is only little visual

difference between the analytical and computed magnetic fields, the difference between them is additionally plotted. The distribution of modeling errors with respect to fixed transmitter positions (l fixed) is thereby displayed in plots (b), (e) and (h), while errors with respect to a fixed sensor position (m fixed) are plotted in subfigures (c), (f) and (i).

grid label	dx [m]	dz [m]	x_b [m]	N_b	N_x	N_z	N	T_{CPU} [s]
C5	0.16875	0.2	5	2	52	102	5824	1448
C10	0.16875	0.2	10	4	52	102	6360	1590
B5	0.3375	0.4	5	2	26	51	1590	182
B10	0.3375	0.4	10	4	26	51	1870	234
B20	0.3375	0.4	20	8	26	51	2478	437
B50	0.3375	0.4	50	20	26	51	4686	1607
B100	0.3375	0.4	100	40	26	51	9646	5703

Table 4.1. Grid specifications of all considered FE grids. T_{CPU} denotes computational time needed to perform a single forward run, comprising 1656 possible transmitter-receiver combinations of *s-pole*, *v-dipole* and *h-dipole*.

Results for the *v-dipole* and *h-dipole* configuration show excellent agreement with the analytical solution. Modeling errors converge rapidly towards zero in case of increasing the size of the boundary grid, and give rise to the fact that sufficient modeling accuracy is already achieved for grid B20. The only considerable modeling errors occur when approaching the earth-air interface. Nevertheless, even these larger discrepancies of 0.05 nT/A (Fig. 4.9h) corresponds to a maximum relative error of 0.5 % which emphasizes the first guess of an excellent agreement.

Meanwhile, the *s-pole* configurations feature larger and more systematic errors. Modeled values systematically underestimate the analytical ones. This constant error for a certain grid decreases from 0.06 nT/A (grid B5) to 0.01 nT/A (grid B20) for an increase of the boundary grid (Fig. 4.10). Note that the type curves for grid B100 exhibit no systematic error. However, the systematic errors correspond to an average relative error of 3% (Fig. 4.10b-c) or 0.6% (Fig. 4.10h-i).

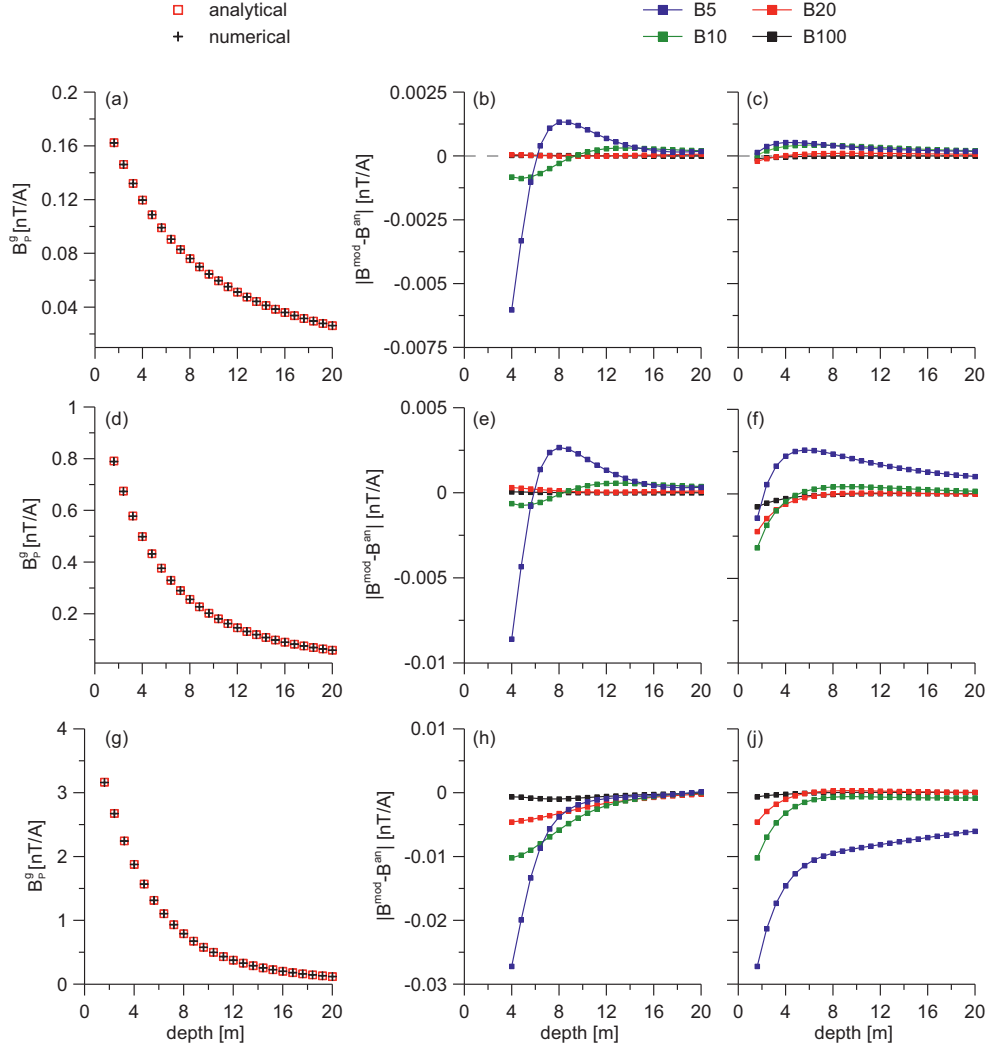


Figure 4.8. Modeling accuracy for the v -dipole configuration. Modeled and analytical responses B_p^g are compared in the left column (exemplarily for grid B20). Errors are displayed for all considered FE grids of type B in the center and right columns. Fixed model parameters are: (a-b) $l = 1$, (c) $m = 1$, (d-e) $l = 13$, (f) $m = 13$, (g-h) $l = 24$ and (i) $m = 24$.

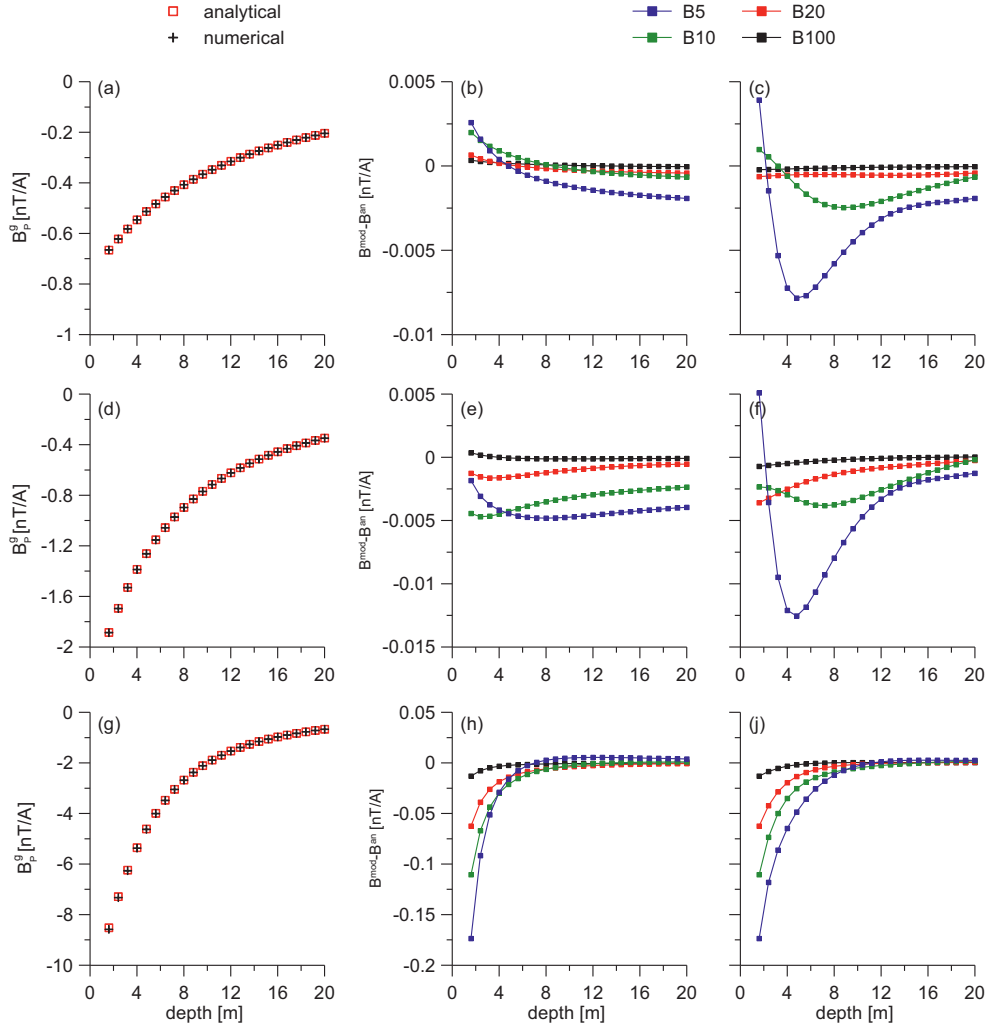


Figure 4.9. Modeling accuracy for the *h-dipole* configuration. Modeled and analytical responses B_p^g are compared in the left column (exemplarily for grid B20). Errors are displayed for all considered FE grids of type B in the center and right columns. Fixed model parameters are: (a-b) $l = 1$, (c) $m = 1$, (d-e) $l = 13$, (f) $m = 13$, (g-h) $l = 24$ and (j) $m = 24$.

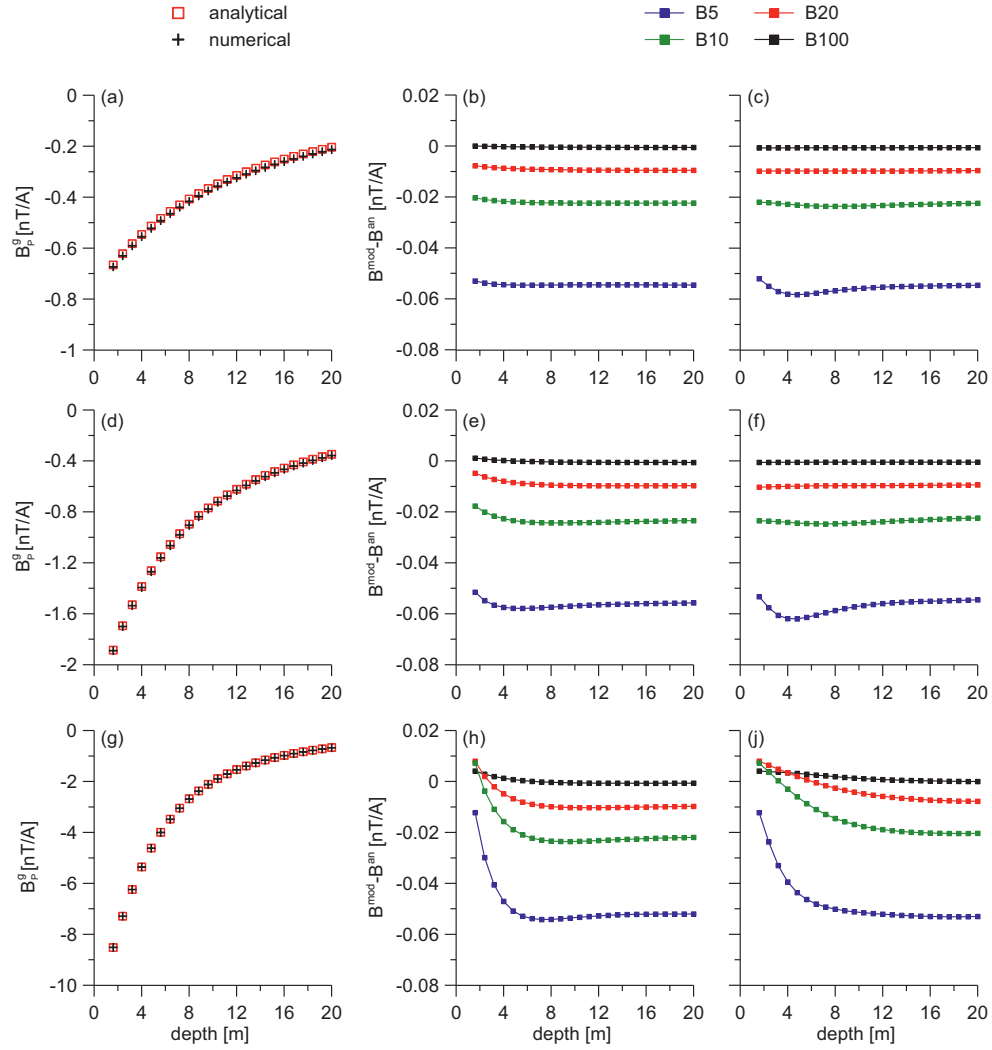


Figure 4.10. Modeling accuracy for the *s-pole* configuration. Modeled and analytical responses B_p^g are compared in the left column (exemplarily for grid B20). Errors are displayed for all considered FE grids of type B in the center and right columns. Fixed model parameters are: (a-b) $l = 1$, (c) $m = 1$, (d-e) $l = 13$, (f) $m = 13$, (g-h) $l = 24$ and (j) $m = 24$.

In a previous numerical study using the FE method, Fathianpour et al. (2005a) have reported an average error of 4% for the B_y component of a magnetic field measured along a surface profile and by employing only one surface electrode.

Besides the modeling accuracy, the computational time T_{CPU} , needed for a single forward run (Table 4.1), is an important factor to consider. Computational time T_{CPU} is of particular relevance for the sensitivity calculation as the total computational time, needed to generate a 2D sensitivity map, increases at least directly proportional with the number of elements. For instance, total time needed to compute a sensitivity map with grid B100 is $7 \cdot 10^7$ times higher compared to the computation with grid B20. In fact, we would need more than 10 weeks longer to generate similar maps.

It is concluded that grid B20 is the best choice as it combines excellent modeling accuracy, below 0.5% for dipole and below 3% for *s-pole* current injection, and a proper computational time required for sensitivity considerations. Finally, the distribution of all modeling errors with respect to their corresponding absolute values is shown in Fig. 4.11.

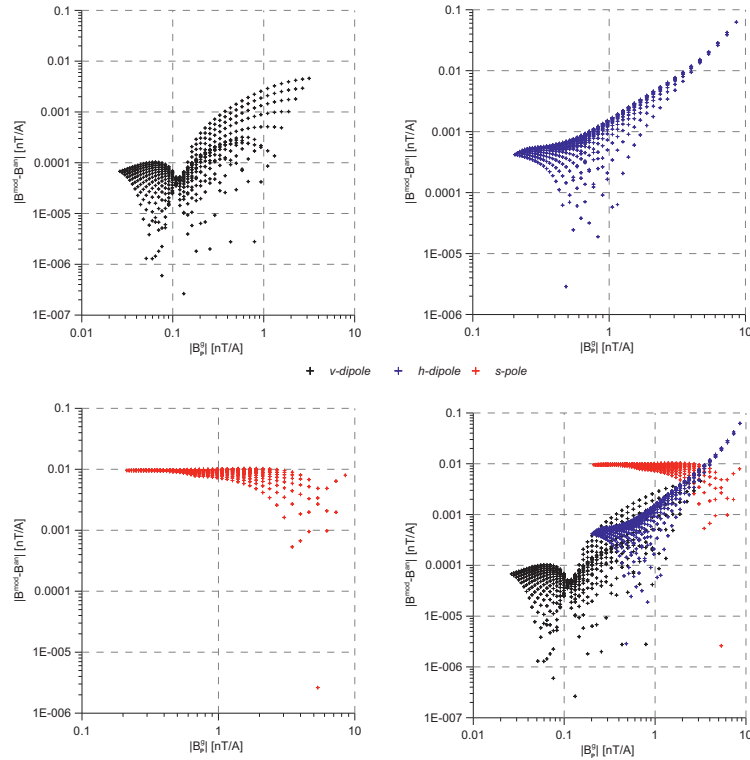


Figure 4.11. Modeling errors $|B^{mod} - B^{an}|$ obtained for modeling on grid B20 versus modeled ground response $|B_p^g|$ displayed for all feasible transmitter-receiver combinations.

4.4.4. Layered test model

In a second step, our program is checked with a two-layer half-space model. In order to verify the numerical modeling with published results, the example discussed by Veitch et al. (1990) and later reconsidered by Chen & Oldenburg (2004), who finally provided data for comparison, is used. As shown in Fig. 4.12, a standard model with a layer boundary at 50 m, depth of a single transmitter electrode $d = 25$ m, borehole separation $r = 50$ m and a resistivity contrast $s = \rho_1/\rho_2 = 10$ was adopted. Modeling accuracy is investigated by varying d , r and s independently. Due to the fact that d and r are varied between 10 m and 200 m, a discretization with $dx = 5$ m ($dx = dz$) was employed. Additionally, the boundary grid was extended outwards by 500 m.

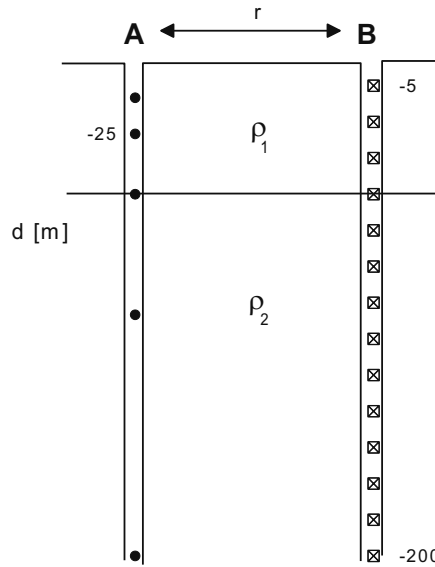


Figure 4.12. Geometry of the layered test model. Standard parameters are given explicitly. Symbols are the same as in the previous figures (Fig. 4.6).

In Fig. 4.13a, 4.13c and 4.13e the modeled ground responses B_p^g obtained for the standard model, are compared to the results of Chen & Oldenburg (2004), referred to as the *reference* values. The value of the varied model parameter is labeled on the respective profile. Modeling errors for all varied model parameters are plotted in subfigures (b), (d) and (f).

A common feature to all response curves is the discontinuity in the slope at the layer interface, which also denotes in all cases the highest absolute value. This response characteristic was earlier referred to as a primary advantage of MMR surveying, as pointed out by Veitch et al. (1990). Modeling errors are generally below 10 pT/A except for the peak values.

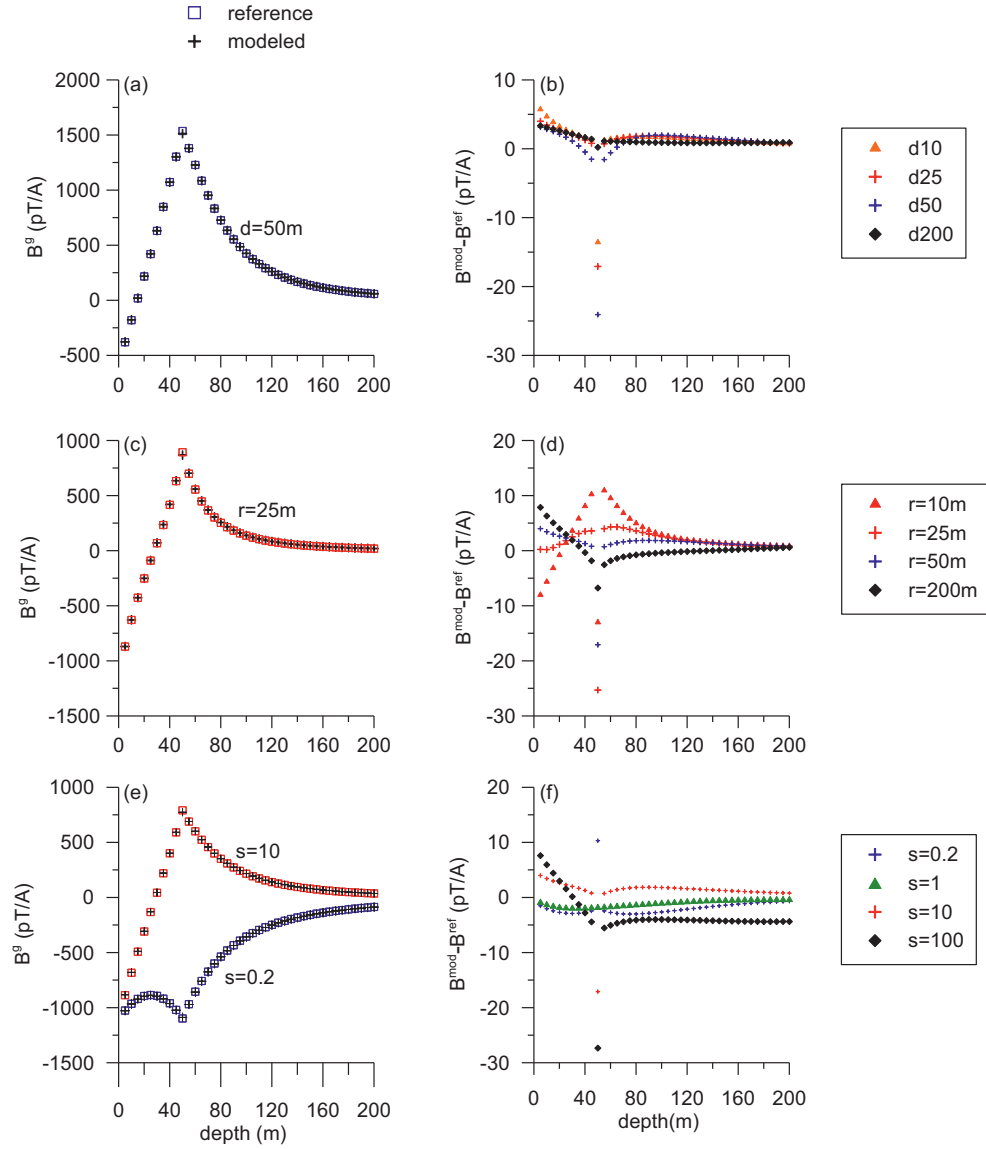


Figure 4.13. Modeling accuracy for the layered test model. Comparison of analytical and modeled values obtained for the MMR ground component B^g are shown in the left column. Differences are displayed in the right column. Varied parameters are: (a-b) depth of the transmitter electrode d , (c-d) borehole separation r and (e-f) conductivity contrast s .

However, modeling errors occurring at the peak values correspond to a maximum relative error of 3%. Nevertheless, the average relative error is below 1% for all other variations, stating that computed results are in an excellent agreement with the reference values.

Fathianpour et al. (2005) reported for a vertical fault test model an average relative error of less than 1% for the B_y component, but with the addition of a larger grid and a higher number of wavenumbers. Boggs et al. (2005) verified specified modeling errors for an inclined fault model of up to 30 %, considering surface current excitation and 3D geometries and verifying only the vertical component of the magnetic field.

Concluding, the results of the implemented forward modeling program MMRMod are in good agreement with the analytical solutions as well as with published results and can now readily be used for the numerical analysis of different transmitter configurations (Chapter 5). In order to support this analysis by means of 2D sensitivity maps, the basic formulations of MMR sensitivity computation, used in the present work, are described in the following section.

4.5. Sensitivity calculation

4.5.1. The MMR sensitivity

The MMR sensitivity Φ is the derivative of the magnetic response B , at an arbitrary point m within the model space, with respect to the resistivity ρ assigned to the n th block or element within the model space. For a fixed transmitter position l sensitivity is defined as

$$\Phi_{mn} = \frac{\partial B_m}{\partial \rho_n}. \quad (4.20)$$

The sensitivity matrix Φ_{mn} contains the sensitivities at all considered points m within the model space with respect to all resistivity blocks n . On the one hand, a row contains information on the spatial sensitivity distribution for a specific source-receiver configuration. This is of special concern for the survey design because we have to select transmitter-receiver combinations so that their high-resolution regions cover the entire area of interest. On the other hand, every column contains the sensitivities for all receiver locations with respect to a fixed volume. They are to be considered if a priori information on the location of a target body exists and the optimum resolution of the source-receiver configuration is searched.

4.5.2. Calculation of sensitivity by perturbation approach

The differential form $\partial B_m / \partial \rho_n$ may be substituted by a difference expression $\Delta B_m / \Delta \rho_n$. We specify single-sided perturbation by changing the resistivity of a single element by a small amount and subtracting the unperturbed magnetic response from the perturbed one. With $\Delta \rho_n = \rho''_n - \rho'_n$ and ρ''_n as perturbed resistivity, an approximation of the sensitivity Φ_{mn}^s is obtained according to the following equation:

$$\Phi_{mn}^s = \frac{B_m(\rho_n'') - B_m(\rho_n')}{\Delta\rho_n}. \quad (4.21)$$

This type of approximation is referred to as single-sided perturbation. Another possibility is to increase and decrease the resistivity in the particular cell by the amount $\Delta\rho_n$. By subtracting the resulting two magnetic responses from each other, a sensitivity estimate via double-sided perturbation Φ_{mn}^d is obtained.

$$\Phi_{mn}^d = \frac{B_m(\rho_n' + \Delta\rho_n) - B_m(\rho_n' - \Delta\rho_n)}{2\Delta\rho_n} \quad (4.22)$$

An important difference between the two approaches is the required computation time. Modeling of a 2D sensitivity distribution via single-sided perturbation necessitates, besides the computation of the unperturbed magnetic response, a single forward run for each cell, whereas in the double-sided approach two independent runs are necessary. Hence, modeling expense, in terms of T_{CPU} , would be doubled. Tests may reveal if the two approaches yield similar results. Furthermore, to identify the correct amount of $\Delta\rho$, sensitivities are calculated for an arbitrary chosen cell and a wide range of perturbations varying between 0.01% and 50% of the considered background value (magnetic response is independent of the background value). In fact, a background value of $\rho_0 = 1 \Omega\cdot m$ is employed.

First of all, Fig 4.14 clearly reveals that both single-sided and double-sided perturbation achieve similar values for all three considered transmitter configurations. Generally, both types of computation achieve a stable value between 0.1% and 1%. In case of a vertical offset between transmitter and receiver location (Fig. 4.14a-c and Fig. 4.14g-i) computation of sensitivity becomes numerically instable for smaller perturbations, in some cases already for $\Delta\rho$ lower than 1% (Fig. 4.14h). Thus, seeing these two features a perturbation amount of 1% ($\Delta\rho = 0.01 \Omega\cdot m$) is chosen for the sensitivity calculations in Chapter 5.

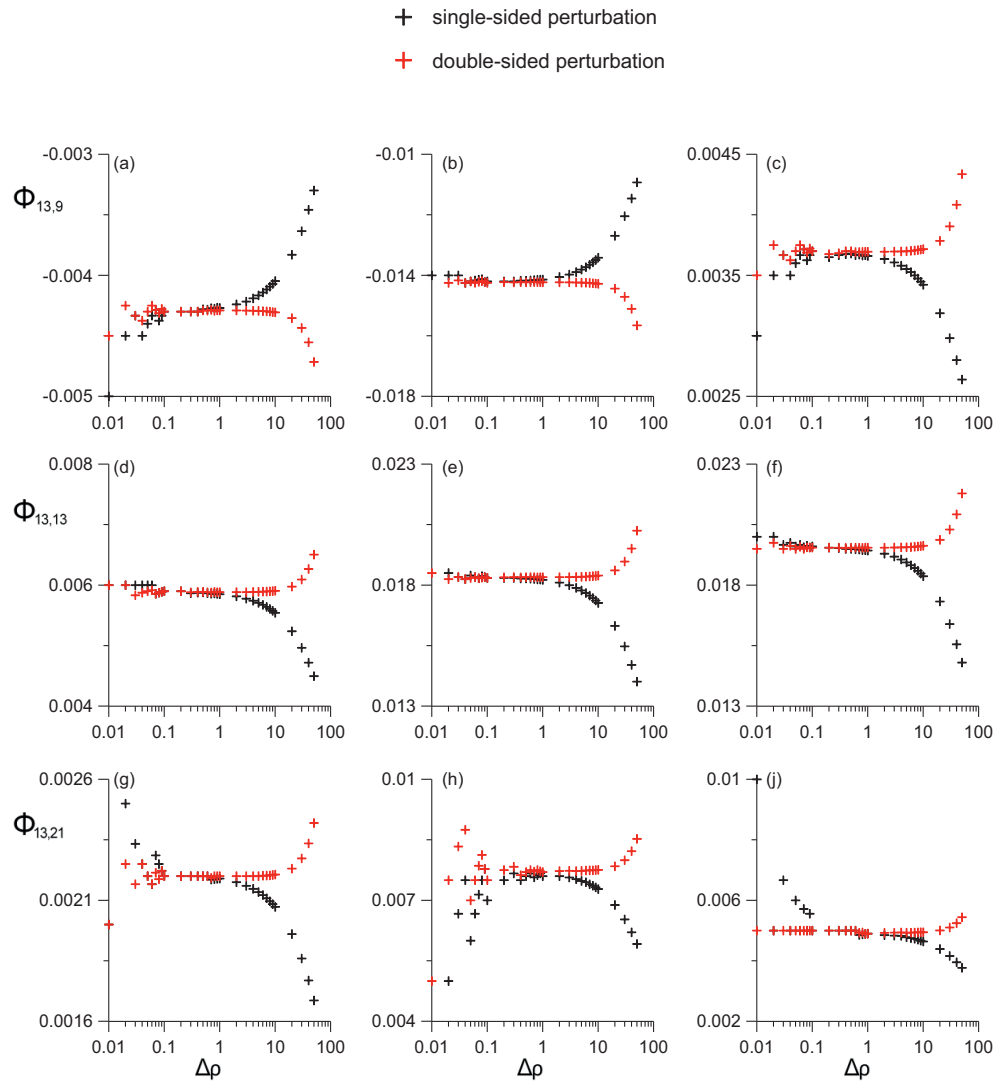


Figure 4.14. MMR sensitivity Φ versus perturbation value $\Delta\rho$ for *v-dipole* (a, d, g), *h-dipole* (b, e, h) and *s-pole* (c, f, i). Transmitter and sensor positions are indicated by the sensitivity index.

Chapter 5

Numerical analysis of different transmitter configurations

In this chapter the numerical methods, described in Chapter 4, are used in order to analyze the different transmitter configurations and their potential application in 2D cross-hole imaging. The numerical analysis comprises the derivation of 1D model response curves (section 5.1) as well as 2D sensitivity maps (section 5.2), both obtained for various transmitter-receiver combinations. A general procedure to minimize site characterization costs is to investigate theoretical responses of planned experiments before field programs are initiated. In the first part of this chapter, such model response curves are predicted for an abstract representation of a hydrogeophysical problem: a small conductive body in resistive half-space. The analysis of these curves is predominantly directed towards the identification of the most suitable transmitter configuration for the planned MMR field application (described in Chapter 7), but can also be interpreted in a more general way. In addition, model response curves enhance the intuitive understanding of cross-hole MMR responses and in particular of the responses to expect in a hydrogeophysical imaging context. Since sensitivity is a substantial and meaningful numerical quantity, the 2D spatial distribution of MMR sensitivity is discussed in the second part. Sensitivity distributions are needed during the inversion process in order to apply appropriate changes to the reconstructed model. The appropriate changes are iteratively made to the dummy model until you reach a certain data misfit.

MMR sensitivity was mentioned sporadically by several authors, all in conjunction with inversion techniques. Chen et al. (2002a) used a sensitivity-based weighting scheme in order to distribute numerical artifacts away from the current sources. For the design of a weighting method, they found it sufficient to use a simple approximation of sensitivity. This estimate was considered to be the sensitivity distribution obtained over a homogeneous half-space. Kemna et al. (2003) presented a real example of the spatial distribution of MMR sensitivity. They adapted a sensitivity-based iterative reconstruction algorithm for both data quality assessment and qualitative imaging purposes. In order to test the algorithm for 2D imaging, again only the pre-calculated sensitivities of the homogeneous case were used.

In this work, sensitivity maps for a homogeneous model are derived first. They may serve as a basis of a primary image reconstruction process. Subsequently, it is tried to ascertain the validity of such an approach in case of heterogeneous subsurface.

Besides its use for model reconstruction, sensitivity is an indicative quantity for experimental design. Therefore, the spatial sensitivity distributions are additionally analyzed in terms of resolving power and survey optimization.

5.1. Model response curves

Model response curves are derived in order to investigate the signal strength and noise level of the different transmitter configurations. Signal strength refers to the MMR ground response B_s^g due to a conductive anomaly (with $\rho_0 = 0.1 \Omega \cdot \text{m}$). In this calculation, the anomaly is a rectangular block symmetrically centered at a depth of 5.6 m at $x = 3.3$ m with sides 1.33 m long in the x-direction and 1.6 m long in the z-direction (Fig. 5.1a). The noise level refers to the expected wire component of the MMR response B^w (Fig. 5.1b).

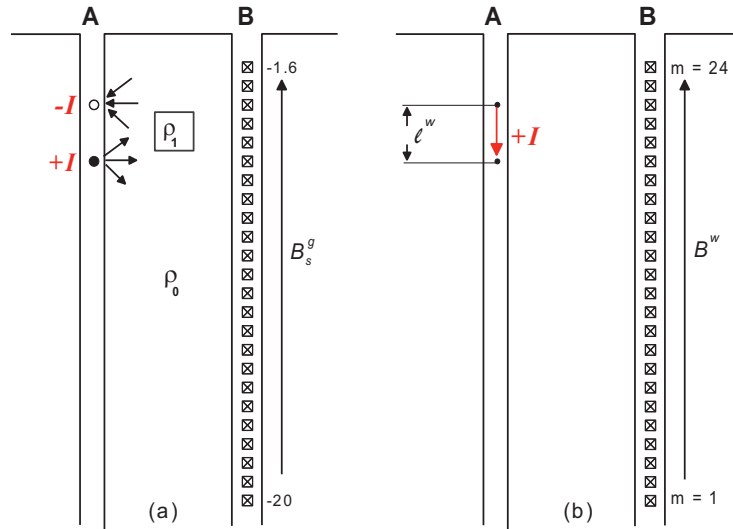


Figure 5.1. Conceptual models for (a) signal strength and (b) source generated noise (exemplarily for a *v-dipole* configuration) investigation.

The data are represented in two ways: the first type features the MMR response as a function of the sensor depth with respect to a fixed transmitter configuration, referred to as moving-receiver setup. By contrast the second type of curve illustrates the MMR response at a fixed sensor position and is therefore a function of the depth of the transmitter electrode, referring to a moving-source arrangement.

5.1.1. Signal strength

Investigations of MMR signal strength are primarily intended to see whether the different transmitter configurations can achieve a threshold value of 0.5 nT/A. This value stems from the MMR measurement system (Chapter 6), that is able to record magnetic field values higher than 0.5 nT/A with an accuracy of 1% (Zimmermann et al., 2008). As a preliminary issue, the optimal dipole length l_{dip} for the *v-dipole* configurations had to be ascertained. Two main aspects are to be considered for the optimal choice. Generally, larger dipole lengths can measure a larger subsurface volume. Indeed, a longer dipole also reduces the total number of feasible transmitter-receiver combinations N_c to be used in a survey, e.g. increasing l_{dip} by 1.6 m decreases N_c by 2. The number of individual measurement configurations N_c in-turn determines the overall cross-hole resolution. The number of electrodes in between the two employed current electrodes can be changed to obtain different dipole lengths. The generated signal strength according to different dipole length l_{dip} is shown in Fig. 5.2. The response peaks clearly exceed the threshold value for dipole lengths equal or longer than 2.4 m. The optimal dipole length $l_{dip} = 2.4$ m is chosen as it combines high amplitude, which is high enough to provide accurate data acquisition as well as a number of independent configurations that is still high enough to achieve a good resolution of the cross-hole region.

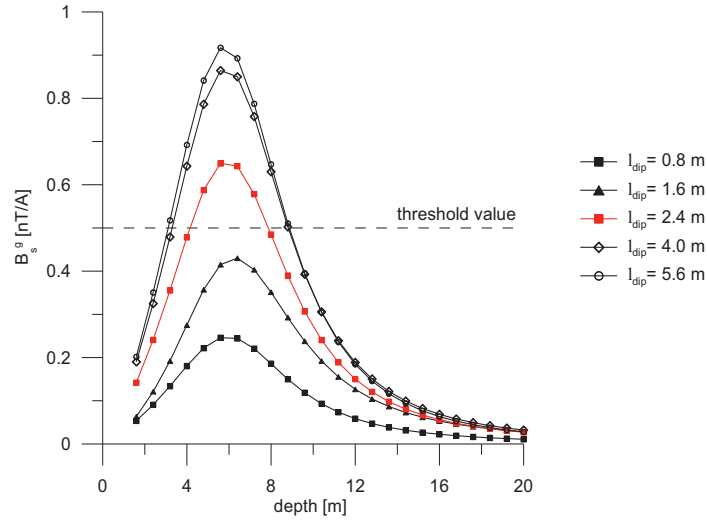


Figure 5.2. Signal strength of B_s^g as a function of the sensor depth with respect to fixed *v-dipole* current injection at the same level as the conductivity anomaly. 5 Different dipole lengths l_{dip} for *v-dipole* configurations are shown.

In the following, model responses are shown (Fig. 5.3) for three depths of investigation, located near-surface ($l, m = 21$), at the same level of ($l, m = 19$) and below the considered anomaly ($l, m = 17$).

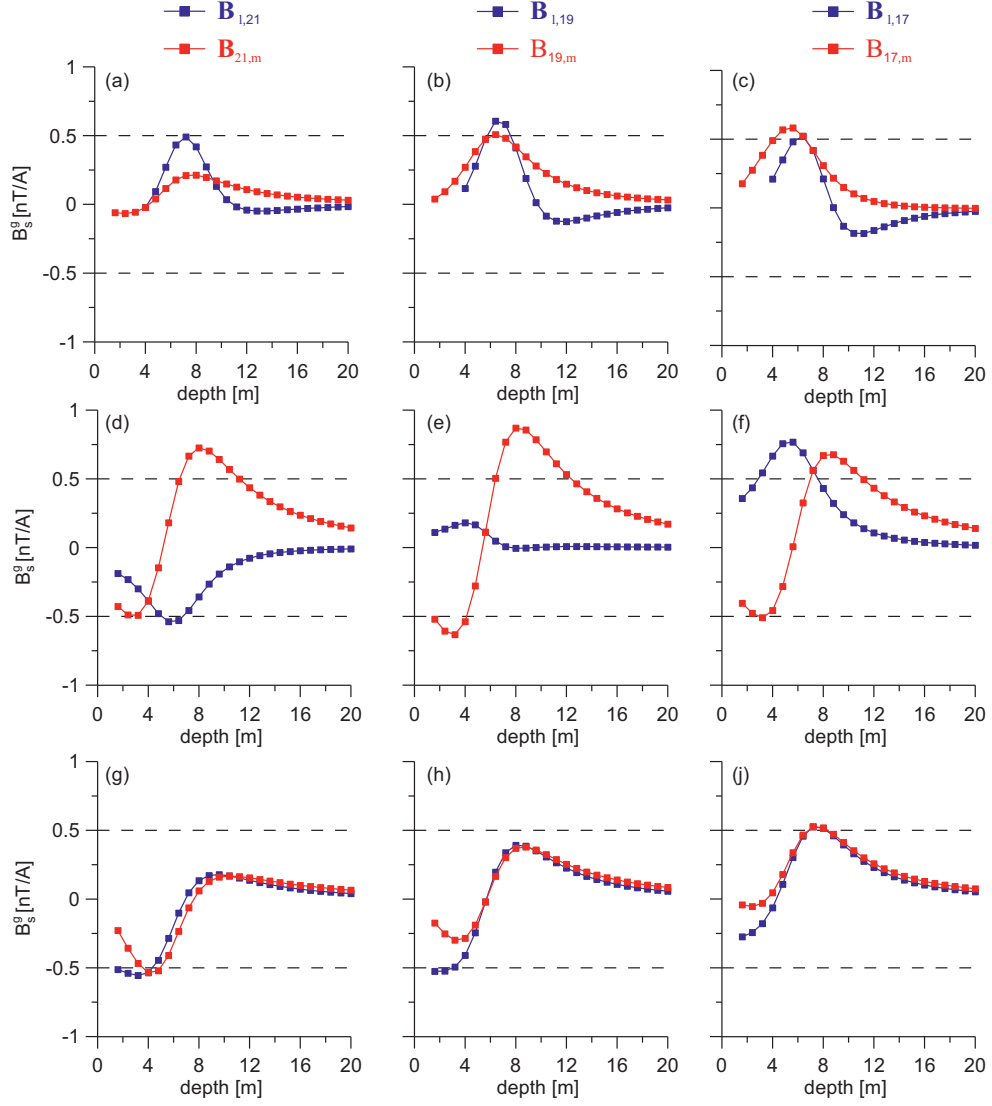


Figure 5.3. Variation of B_s^g with depth of the transmitter electrode (blue) and with sensor depth (red). B_s^g is the magnetic field due to a conductive body (with $\rho_1 = 0.1 \Omega \cdot m$) for transmitter configuration (a-c) v -dipole, (d-f) h -dipole and (g-i) s -pole. Dashed lines mark threshold value for the signal strength.

The largest values of B_s^g are obtained for the *h-dipole* configuration (Fig. 5.3d-f), having a peak value of 0.8 nT/A for moving receiver setup with $l = 19$. Furthermore, *h-dipole* configurations exhibit high peak-to-peak values due to the fact that the response curves exceed the threshold value for both a positive and a negative maximum. Model response curves feature two peak values of opposite polarity, whereas the negative peaks are less pronounced than the positive ones.

For the *v-dipole* configuration, all model response curves exhibit a single positive peak. The response peaks only exceed the threshold value when the fixed sensor or transmitter, are at the same level as the anomaly. Note that the maximum peak, for a moving receiver setup, is obtained for the transmitter electrode positioned below the anomaly (Fig. 5.3c), as the actual mid-point of the vertical dipole is on level with the depth of the anomaly.

The lowest peak values are generated by *s-pole* configurations. Due to the reciprocity principle transmitter and receiver are interchangeable and therefore curves for both moving source and moving receiver setup are almost identical.

5.1.2. Implication for tomographic surveys

In order to examine the transmitter configurations also in a tomographic sense, an investigation of the response characteristics of selected curves was done to see if they could be used as a proxy for high resolution.

Generally, response curves for the *v-dipole* configurations (Fig. 5.3a-c) have a clear positive peak with a maximum at the anomaly's depth range. Peak values and flattening of the curve decrease or increase with increasing vertical offset, regarding the center of the anomaly.

The response curves for the *h-dipole* configurations (Fig. 5.3d-f) exhibit different shapes and a more complex behavior. For a fixed sensor position, response curves exhibit a polarity change for the generated amplitude peak, whereas for $m = 19$ no significant response values are yielded. By contrast, response curves generally feature two peaks of opposite polarity for a fixed transmitter configuration, whereas the negative peaks are less pronounced than the positive ones. The spatial mid-point between these two extreme values exactly coincides thereby with the center of the anomaly.

Response curves for *s-pole* configurations (Fig. 5.3g-i) reveal similar characteristics. However, the determination of the anomaly's depth through peak values is less accurate compared to the *h-dipole*. Furthermore, curves partly show no real peak. This, plus the low generated signal strength, makes this type of configuration the least meaningful.

As a quantitative indicator, the departure of the response curve from a delta function is investigated. The idea behind this strategy is the fact that a narrower peak represents a smaller

resolved subsurface volume. The peak width w_{peak} is defined as the depth range where the response values have descended to half of the maximum value B_{max} .

This is quantified for the model response curves obtained for the fixed sensor position $m = 17$ (redrawn in Fig. 5.4). For this case all three curves exhibit similar shape: They only have one positive maximum. Results show that *v-dipole* configurations clearly produce the narrowest peak, whereas *h-dipole* and *s-pole* configurations with almost double peak width sample rather large volumes.

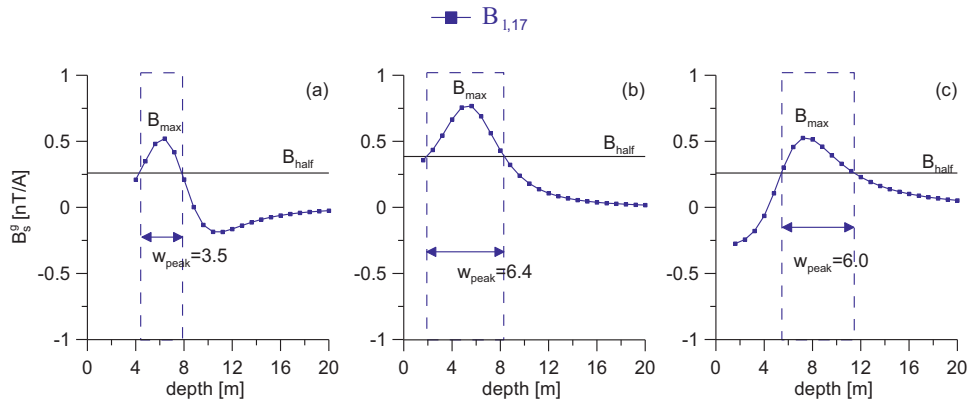


Figure 5.4. Variation of B_s^g with respect to fixed sensor position $m = 17$ (as in Fig. 5.3). Model response curves are displayed for (a) *v-dipole*, (b) *h-dipole*, (c) *s-pole*.

5.1.3. Source-generated noise

The last part of this section focuses on the source-generated noise of each transmitter configuration. The noise level is quantified in terms of magnetic field due to the current carrying wire. The wire is assumed to run strictly vertical, 0.05 m to the left of borehole A and 0.05 m to the right of borehole B. Furthermore, the wire is assumed to run along with the x-axis and to coincide with the air-earth-interface, in case surface segments are required (*h-dipole* and *s-pole*). In order to investigate the different configurations in terms of signal-to-noise ratio (SNR), a threshold value for the wire contribution is appointed with 10 nT/A. In conjunction with the threshold value for the signal strength a SNR of 5% is yielded.

The response curves for the *h-dipole* configurations (Fig. 5.5d-f) exceed the threshold value by several magnitudes over the entire model depth. Using *h-dipole* transmitter configuration would therefore impede a correct data acquisition. Two negative features are obvious for the *s-pole* configurations (Fig. 5.5g-i). On the one hand, the response curves distinctly exceed the threshold value either for the moving source or the moving receiver setup (or both). Otherwise, the curves show a zero crossing, which is highly dependent on the correct prediction of the wire layout, in particular the correct positioning of the wire at the surface.

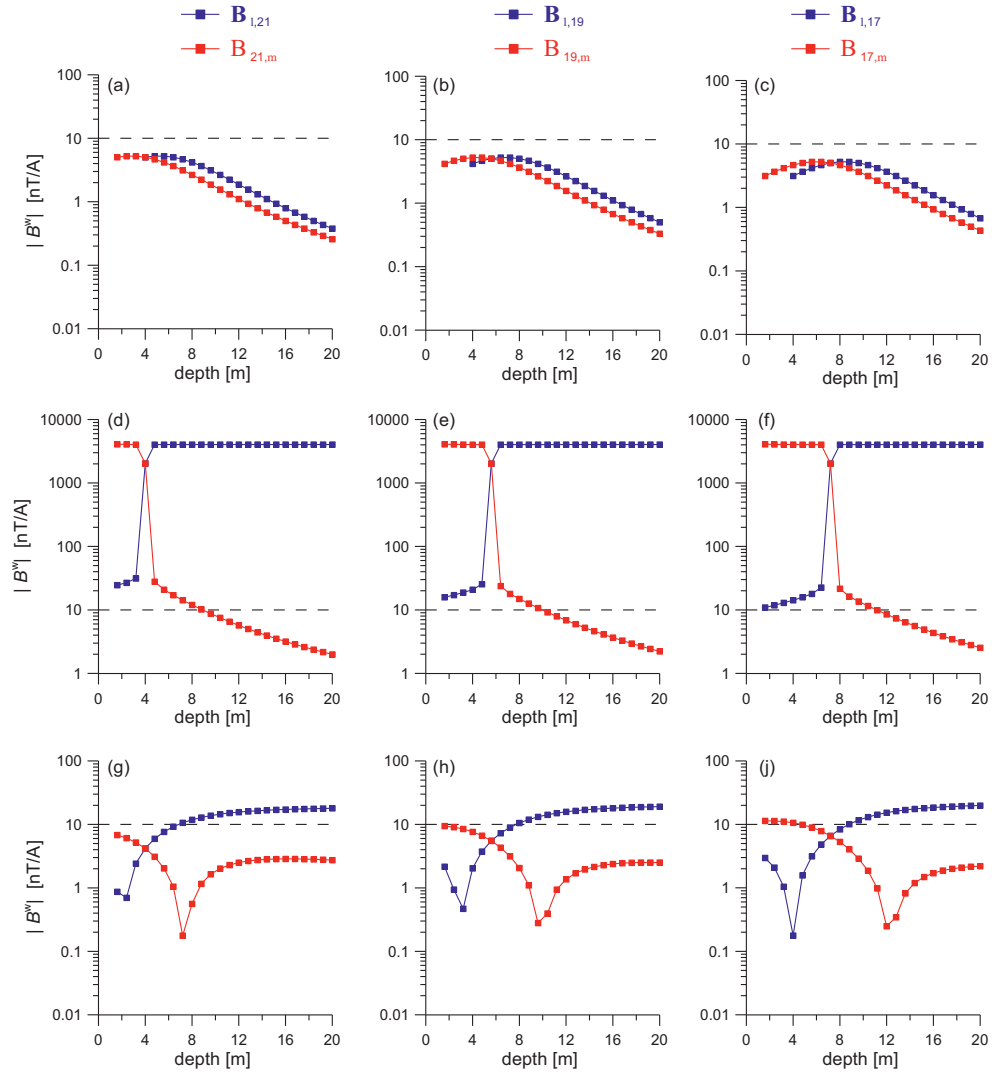


Figure 5.5. Variation of $|B^w|$ with depth of transmitter electrode (blue) and with sensor depth (red) for *v-dipole* (a-c), *h-dipole* (d-f) and *s-pole* (g-i). Dashed lines indicate SNR of 5%.

By analyzing the responses, obtained for *v-dipole* configuration (Fig. 5.5a-c), it is recognized that this type of array clearly exhibits the best signal-to-noise behavior. From a practical point of view, the wire layout of *v-dipole* features shortest and invariant lengths and is most-distant from the considered measurement points. From the numerical point of view, computation of the wire contributions for *v-dipole* can be most easily and most rapidly accomplished.

5.2. Sensitivity distributions

The MMR sensitivity indicates the change in MMR ground response due to a change in resistivity of a volume block or finite element. Each single transmitter-receiver combination exhibits its own sensitivity distribution. In order to give a comprehensive overview using the least number of figures, the arrangements are depicted using a moving receiver setup consisting of five consecutive offset sections. Due to the fact that the sensitivity only depends on the relative position of source and receiver, a moving source setup would yield a similar pattern. The considered configurations share the same transmitter electrode located at -10.4 m depth ($l = 13$). The sensor positions feature therein vertical offsets with respect to the transmitter electrode ranging from $+r$ to $-r$. Fig. 5.6 shows the considered moving-receiver setup schematically.

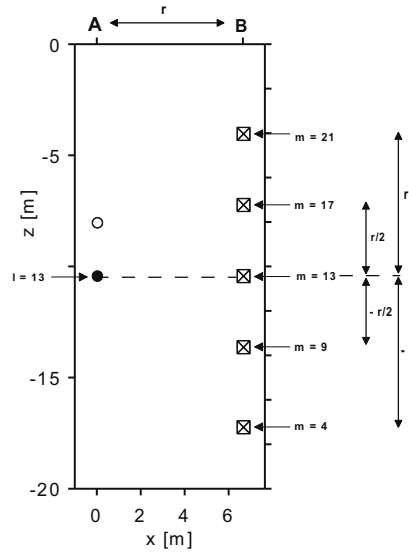


Figure 5.6. Moving receiver setup used for the sensitivity calculation for homogeneous medium. Capital letters A and B indicate the positions of the boreholes.

First, the sensitivity obtained for a homogeneous conductivity distribution is examined. Afterwards a more complex, inhomogeneous conductivity model will be considered. Finally, a sensitivity-based comparison between the conventional DC resistivity method and the MMR method is discussed.

All sensitivity distributions are obtained using 2.5D MMR forward modeling program MMRMod and perturbation approach (Chapter 4). The sensitivity is displayed as a logarithmic property normalized by the maximum of the sensitivity values obtained for each transmitter configuration. Table 5.1 shows the maximum sensitivity value obtained for each offset section and transmitter configuration, separately, whereby bold printed values are used as normalization factors. Finally, displayed sensitivity distributions are smoothed by interpolating modeled values on a finer grid of 0.1×0.1 m resolution.

transmitter configuration	sensitivity $\Phi_{l,m}$				
	$\Phi_{13,21}$	$\Phi_{13,17}$	$\Phi_{13,13}$	$\Phi_{13,9}$	$\Phi_{13,4}$
<i>s-pole</i>	0.0867	0.1480	0.1593	0.1655	0.1115
<i>v-dipole</i>	0.1292	0.1672	0.1801	0.1785	0.1166
<i>h-dipole</i>	0.1528	0.6916	14.48	0.7106	0.1760

Table 5.1. Maximum sensitivities obtained for the homogeneous medium and the considered transmitter-receiver combinations (Fig. 5.6). Normalization factors are printed bold.

5.2.1. Homogeneous case

The most common way to analyze the sensitivity of a measurement configuration is to take a look at the spatial distribution of positive and negative sensitivities.

For the sensitivity computation, a uniform half-space with $\rho_0 = 1 \Omega \cdot \text{m}$ and perturbations with $\Delta\rho = 0.01 \Omega \cdot \text{m}$ (according to the results in section 4.4) are considered. The basic properties of the sensitivity maps are explained for an *s-pole* configuration, as the spatial distributions are less complex in this case. The different transmitter configurations are compared in terms of varying resolving power as well. Fig 5.7 shows the sequence of sensitivities obtained for the *s-pole* configuration. Solid lines mark zero sensitivity lines, which are associated with a change of sign. These lines coincide with the direct connection of transmitter and receiver.

Generally, the absolute value of the sensitivity increases as one approaches the transmitter or receiver locations. Distinct areas of high positive and negative sensitivity are visible, at least for the zero and medium offset sections. These zones stretch out between source and receiver, forming tube-like, slightly bended structures. For the zero-offset case, the region of maximum sensitivity extends over a depth range equivalent to the borehole separation. For transmitter-receiver combinations having maximum offset¹ significant sensitivity values are exclusively obtained in the nearby region of transmitter and receiver. While for cells located above the

¹ Corresponds here to a full borehole separation

zero-sensitivity line an increase of resistivity results in a decrease of magnetic response, the same increase causes an increase of magnetic response for cells below the line. In other words, the secondary magnetic field B_s^g caused by a resistive perturbation/anomaly above the direct connection of transmitter and receiver is negative whereas B_s^g is positive for subjacent regions. In case of a conductive anomaly, response conditions are vice versa.

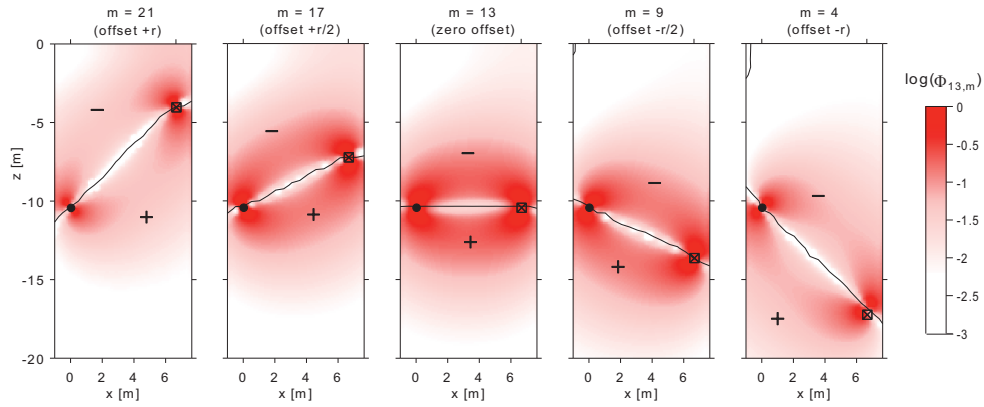


Figure 5.7. Logarithmic normalized sensitivity for an *s-pole* configuration in a uniform half-space, shown along five consecutive offset sections (a)-(e). The solid lines denote the zero-sensitivity lines; + and – denote regions of positive and negative sensitivity. Transmitter and receiver are indicated as circles and crossed square, respectively.

For dipole configurations again distinct regions of negative and positive sensitivity appear which are significantly less spatially extended. Both types (*v-dipole* and *h-dipole*) have in common that the zero-sensitivity line forms the interconnection of both electrodes and the magnetic sensor. Thereby, the magnetic sensor takes up the position in-between. For the *v-dipole* configuration (Fig. 5.8) a tube-like zone of negative sensitivity stretches out between transmitter electrodes and magnetic sensor, that is almost entirely enclosed by the zero-sensitivity line. This high sensitivity region exhibits considerably less depth extension, than the *s-pole*, approximately equivalent to the dipole length l_{dip} . The maximum offset using a *v-dipole* configuration yields almost zero resolution of the cross-hole region.

Using an *h-dipole* configuration with zero offset produces a maximum sensitivity that exceeds the peak value of *s-pole* and *v-dipole* configurations by two magnitudes (Table 5.1). Unfortunately, the generated region of high sensitivity is restricted to a few cells surrounding the sensor position (Fig. 5.9c). For the medium offset sections (Fig. 5.9b, d) zones of high sensitivity develop along the receiver borehole, more precisely between sink electrode and magnetic sensor. While for a sensor position above the dipole this zone becomes positive (Fig. 5.9b), it is negative for a corresponding position below (Fig. 5.9d).

However, considering *h-dipole* no offset section can achieve significant resolution of the (inner) cross-hole region.

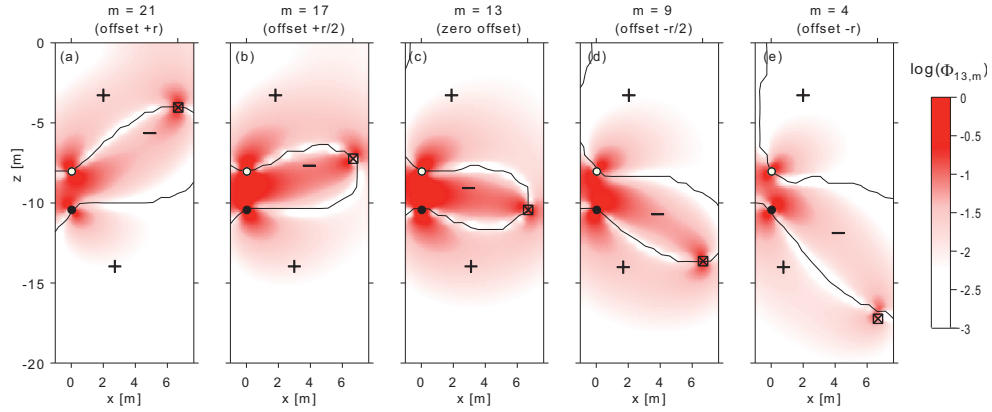


Figure 5.8. Logarithmic normalized sensitivity for a *v-dipole* configuration in a uniform half-space. Sections and indications are as in the previous figures.

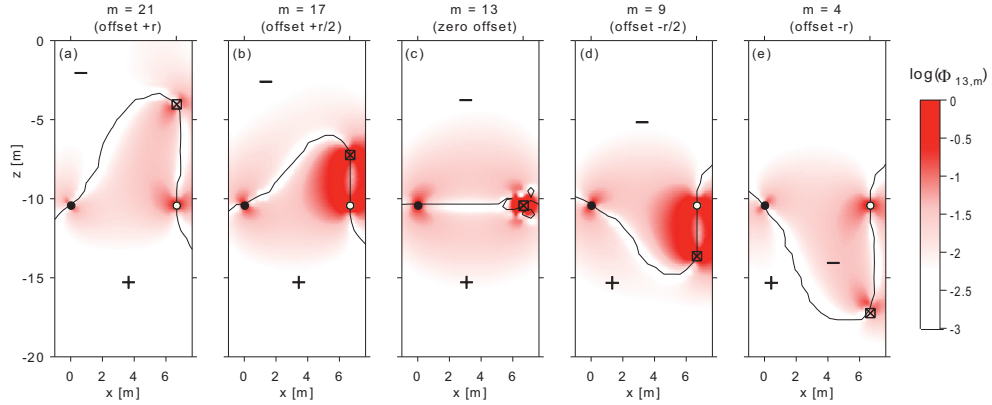


Figure 5.9. Logarithmic normalized sensitivity for an *h-dipole* configuration in a uniform half-space. Sections and indications are as in the previous figure. Note that the sink electrode isn't visible in the zero-offset section due to its nearby position to the magnetic sensor.

5.2.2. Inhomogeneous case

Non-uniform conductivity structures deform sensitivity distributions obtained for the homogeneous case. The following example gives an overview of what to expect for a more heterogeneously structured medium. For this purpose, only the most informative transmitter-receiver combinations of each configuration are to be considered. In order to calculate sensitivity, the unperturbed resistivity distribution ρ' is assumed to be a layered half-space composed of three layers. The middle layer extends from 7.2 m to 11.2 m depth and contains all electrodes (Fig. 5.10). First and third layer obey equal resistivity with $\rho_1 = \rho_3 = 1 \Omega \cdot \text{m}$, as in the homogeneous case. The resistivity of the intermediate layer is varied from $0.1 \Omega \cdot \text{m}$ to $10 \Omega \cdot \text{m}$ within five steps. The 3rd step is thus the homogenous case. To evaluate the influence of conductivity contrasts with respect to the homogeneous case the former normalization factors (Table 5.1) are maintained.

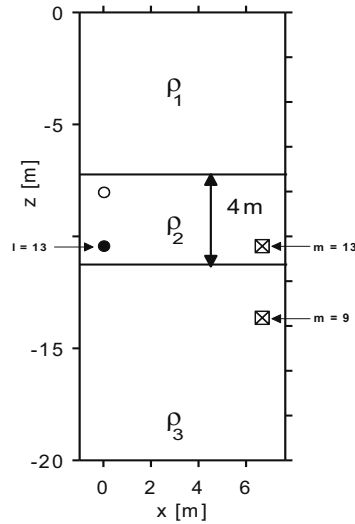


Figure 5.10. Geometry of the three-layer half-space with $\rho_1 = \rho_3$. Transmitter-receiver combinations to be considered for the inhomogeneous case are indicated.

Results for the *s-pole* and *v-dipole* configuration show a similar behavior (Fig. 5.11 and 5.12). For both cases, transmitter and sensor exhibit zero offset. For a conductive layer with $\rho_2 = 0.1 \Omega \cdot \text{m}$ (Fig. 5.11a and 5.12a), the spatial pattern is significantly disturbed as maximum sensitivity is obtained throughout the entire middle layer. By contrast, the first and third layers exhibit almost no sensitivity. For the case that the middle layer becomes resistive with $\rho_2 = 10 \Omega \cdot \text{m}$ (Fig. 5.11d and Fig. 5.12d), merely sensitivity values along the layer

boundaries are yielded. The former high-sensitivity area disappears completely. In cases of moderate contrasts, the pattern of the homogeneous case is nearly maintained.

For the *h-dipole* configuration, transmitter and receiver having medium offset are considered with the receiver positioned below the middle layer. Fig. 5.13(a)-(d) show the same behavior as previously discussed. However, in case of a resistive middle layer, high-sensitivity region of the homogeneous case is cut off at the layer boundary but retains its intensity below the layer.

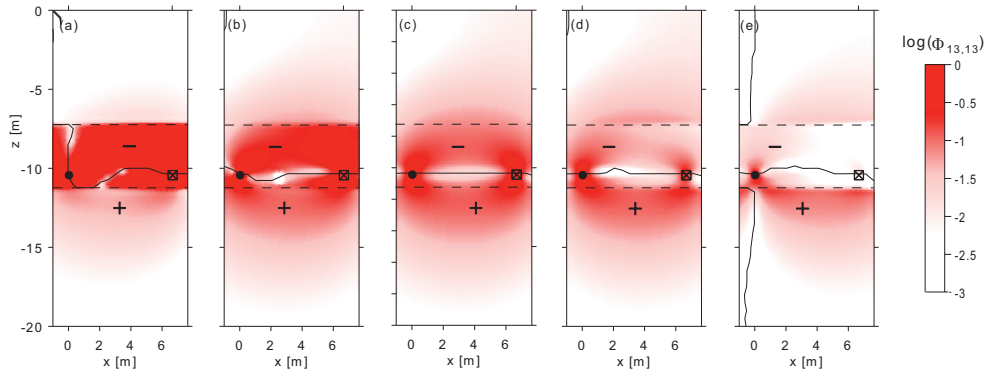


Figure 5.11. Logarithmic normalized sensitivity for an *s-pole* configuration positioned in the middle layer of the three-layer model (zero offset). Resistivity of the middle layer ρ_2 is varied from: (a) $0.1 \Omega \cdot \text{m}$, (b) $0.5 \Omega \cdot \text{m}$, (c) $1 \Omega \cdot \text{m}$, (d) $2 \Omega \cdot \text{m}$ to (e) $10 \Omega \cdot \text{m}$. Layer boundaries are indicated as dashed lines, all other indications are as in the previous figures. Subfigure (c) represents homogeneous case (Fig. 5.7c).

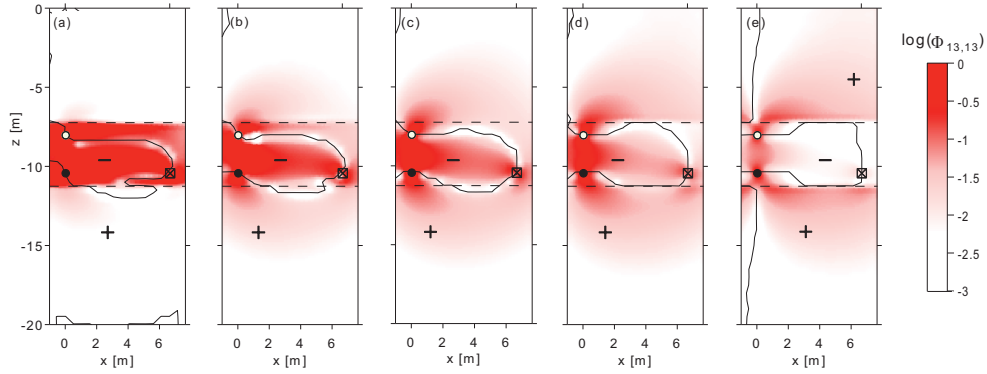


Figure 5.12. Logarithmic normalized sensitivity for a *v-dipole* configuration positioned in the middle layer of the three-layer model (zero offset). Resistivity of the middle layer ρ_2 is varied from: (a) $0.1 \Omega \cdot \text{m}$, (b) $0.5 \Omega \cdot \text{m}$, (c) $1 \Omega \cdot \text{m}$, (d) $2 \Omega \cdot \text{m}$ to (e) $10 \Omega \cdot \text{m}$. Layer boundaries are

indicated as dashed lines, all other indications are as in the previous figures. Subfigure (c) represents the homogeneous case (Fig. 5.8c).

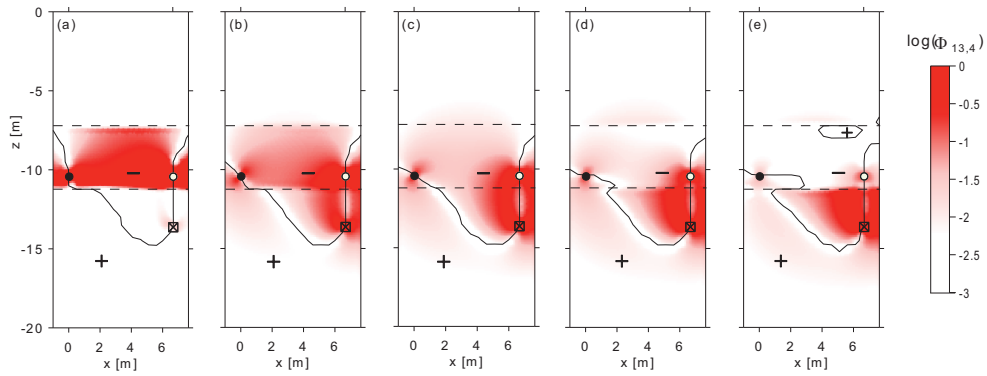


Figure 5.13. Logarithmic normalized sensitivity for an *h-dipole* configuration. The magnetic sensor is positioned below the middle layer of the three-layer model (offset of $-r/2$). Resistivity of the middle layer ρ_2 is varied from: (a) $0.1 \Omega \cdot m$, (b) $0.5 \Omega \cdot m$, (c) $1 \Omega \cdot m$, (d) $2 \Omega \cdot m$ to (e) $10 \Omega \cdot m$. Layer boundaries are indicated as dashed lines. Subfigure (c) represents the homogeneous case (Fig. 5.9c).

5.2.3. Sensitivity-based comparison between DC and MMR method

Another interesting possibility for looking at sensitivity is obtained by exchanging the running index. So far, sensitivity distributions for fixed transmitter-receiver configurations were analyzed by letting the cell index n run through the entire model space. By keeping the location of one resistivity block fixed and letting the magnetic sensor taking up all possible values of the modeling area, more precisely the mid-points of all elements, the following sensitivity maps are generated. Sensitivity is now a function of the magnetic sensor position. The considered perturbation is a resistivity block of rectangular form ($1.33 \text{ m} \times 1.6 \text{ m}$) and symmetrically centered at a depth of 10 m (Fig. 5.13).

These types of sensitivity plots are intended to reveal information about which part of an anomaly can actually be sensed. In order to give a comparative depiction between the conventional DC resistivity and the MMR method, DC sensitivity distributions were computed in the same manner using identical transmitter configurations. For this reason, electric potential distributions were calculated with the existing 2.5D code by Kemna (2000). From the inspection of Fig. 5.14, DC and MMR clearly exhibit strictly opposite sensitivity

characteristics with respect to current flow. A positive maximum of the DC sensitivity is observed for the edges where current flows from the background medium into the conducting block (Fig. 5.14d-f).

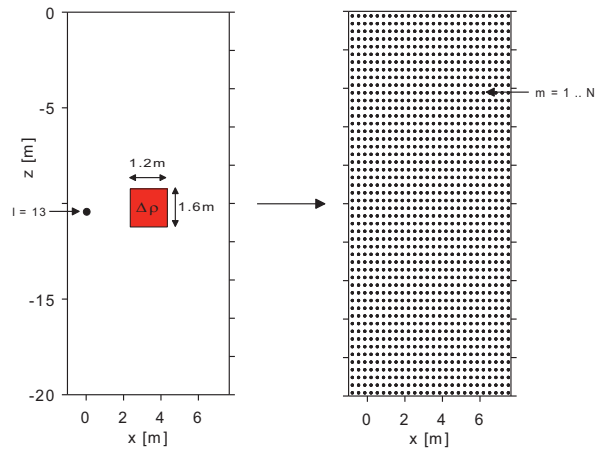


Figure 5.14. Conceptual model for the computations of sensitivities with respect to a fixed block. Running index m (sensor position) takes up the mid-points of all cells.

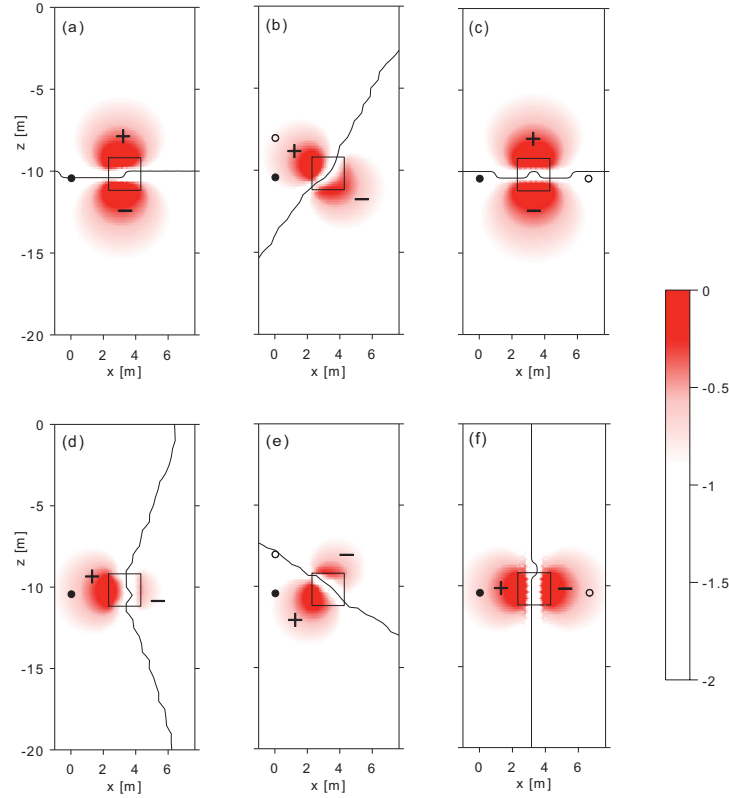


Figure 5.15. Logarithmic normalized sensitivity with respect to a buried cube obtained for MMR (a)-(c) and ERT (d)-(f) and by considering *s-pole* (a, d), *v-dipole* (b, e) and *h-dipole* (c, f) current injection. Note that each sub-figure is normalized to its own maximum value.

This result agrees well with the theory of charge accumulation at conductivity contrasts (Li & Oldenburg, 1991). Due to the accumulated charge an electric potential gradient is induced. The Biot-Savart law (2.3) explicitly indicates that the resultant magnetic response has to be perpendicular to this gradient. Looking for example at the *s-pole* configuration (Fig. 5.14c and 5.14f), DC is most sensitive to the left edge, facing the transmitter electrode, while MMR has greatest sensitivity along upper and lower edge. Additionally, results reveal clearly that DC is not able to resolve opposite edges or corners, respectively, with equal intensity, except for *h-dipole* configurations. In contrast, MMR sensitivity distributions exhibit identical magnitude for opposite edges. This agrees well with the theory that MMR is able to look beneath a conductive overburden, as proposed by Edwards et al., (1978).

5.3. Concluding Remarks

The numerical analysis indicates that *v-dipole* configurations are most suitable for 2D cross-hole applications. From the inspection of signal strength only, a combination of *h-dipole* and *v-dipole* configurations as commonly used in ERT (Deiana et al., 2005) would have been suggested. However, adding the results obtained for the wire component B^w it becomes clear that only *v-dipole* configurations exhibit a maintainable SNR. In addition, the considered wire contribution features a simple shape making it easy to predict. By contrast, the high noise level of *h-dipole* configurations would always impede a correct data acquisition or data processing. Furthermore, with the specified dipole length ($l_{dip} = 2.4\text{ m}$) *v-dipole* configurations offer reasonably high signal strength and response characteristics attractive for tomographic surveys. Sensitivity distributions support this appraisal. Our synthetic sensitivity studies revealed that for a homogeneous medium distinct regions of negative and positive sensitivity appear for all three transmitter configurations. Furthermore, the configurations differ in their sampling volume inferred from spatial extension of high sensitivity values. While *v-dipole* configurations sample rather small, distinct volumes, *s-pole* configurations cause rather large regions of equal sensitivity. Analyzing information from multiple-offset gathers of the each transmitter configuration yields that transmitter-receiver combinations exceeding a vertical offset equal to the borehole separation can be discarded from the data interpretation process. Further effort has to be made to verify this proposition. Development or modification of an existing MMR image reconstruction algorithm (Kemna et al., 2003) will be needed in order to check whether inversion of a full MMR data set and a reduced one (in terms of offset consideration) will yield similar images of the cross-hole region.

The representative example of an inhomogeneous medium suggests that the homogeneous case gives a good approximation or first guess in terms of image reconstruction for moderate conductivity contrasts of approximately 1:2. Since sensitivity computation is time and power consuming, using pre-calculated sensitivities obtained for a homogeneous starting model may increase computational speed. Nevertheless, above these moderate contrasts the spatial pattern of the homogeneous case is broken up so that the sensitivity distributions have to be calculated individually.

Finally, the sensitivity-based comparison of the DC and MMR resistivity method points out that complementary information is obtained from individual data sets. Thus, a combination of both, as proposed by Kulesa et al. (2002) or Kemna et al. (2003), has the capacity to resolve small-scale resistivity variations better than the single method.

Chapter 6

Developing a data processing procedure

Generally, data processing is required after the measurement phase and before data may be interpreted by means of forward modeling or inversion. This chapter describes the applied data corrections necessary to extract the MMR ground response from the measured data.

The vector nature of the magnetic field poses an additional challenge in terms of sensor alignment on MMR data acquisition and processing. During data collection in boreholes, it is impossible to keep the magnetic sensor aligned in any specific direction. The actually measured components are therefore only projections of the desired components. In order to effectively utilize the vector information inherent in magnetic field readings, data have to be transformed into a uniform, reference coordinate system. Svoboda et al. (2002) presented a method to map measured magnetic field components onto a reference direction. In the present study, this method is adapted for cross-hole measurement applications (section 6.3).

Records of the total magnetic field provide a basis for the adapted orientation correction. Via lock-in-technique (section 6.2) the low-frequency magnetic field, associated with the induced current density distribution, is separated from the measured output signal, as proposed by Zimmermann et al. (2005). In addition, a new measurement method with phase switching is introduced in order to compensate for errors induced by the measurement system itself (section 6.4).

The most prominent data processing step is the correction for the magnetic field of the wire delivering current to the respective electrodes (section 6.5), commonly referred to as primary field correction (e.g. Svoboda et al., 2002; Cattach et al., 1993). Finally, data processing procedure is validated based on experimental measurements in a controlled laboratory environment (section 6.6).

At first, a brief description of the MMR measurement system, used in this study, is given. The prototype field instrumentation and the proposed data processing algorithm are developed in close cooperation with the Central Institute of Electronics (ZEL) within the Research Center Juelich under the special direction of Egon Zimmermann.

6.1. The MMR measurement system

The MMR measuring system was developed for tomographic measurements of the (complex) electrical conductivity distribution. The measurement system is designed to record stimulated magnetic fields, associated with low-frequency current injection with a measuring uncertainty of less than 1 %. A sinusoidal voltage source with peak-to-peak amplitude of up to 600 V_{pp} is used to produce the required current density in the ground. A frequency-stable function generator (Agilent 33220A), a power amplifier (Kepco BOB100) and a transformer are employed to generate the excitation signal which is afterwards transferred to commercial electrode switching boxes (GeoServe RESECS) via a multi-core cable (Fig. 6.1). Current and voltage measurements are accomplished in a control unit (MERIT F01) arranged in series between transformer and switching boxes. Each switching box is able to address up to 16 electrodes individually, and measuring system is capable to incorporate up to three boxes. Magnetic field readings are realized through high-sensitive three-axis magnetic field sensors. The choice for and operating mode of the employed sensors are discussed in the next subsection. For the later signal processing, time series of both output and input signal are recorded and sampled with a frequency of 1 kHz. For the operation in a typical laboratory environment, optimal noise reduction is provided by the use of measurement cycles of 10 seconds (Zimmermann et al., 2005). For field measurements, the excitation period has to be adapted to the needed survey speed and to on-site noise level. Electrode switching and signal sampling are PC-controlled.

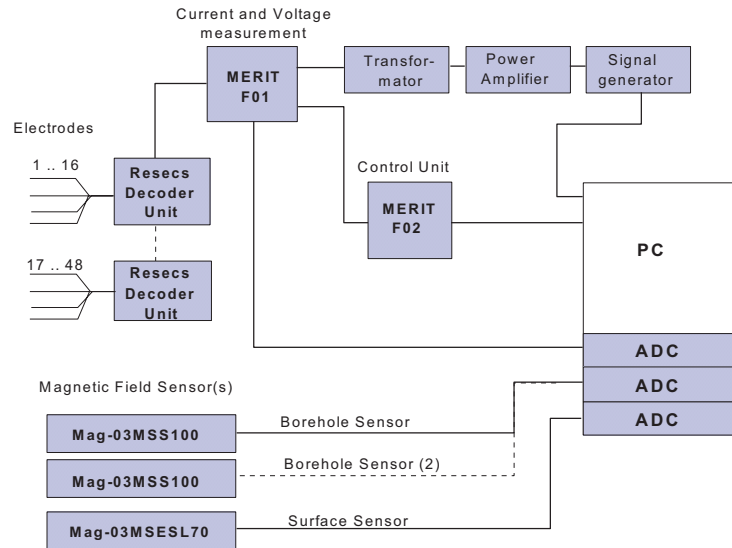


Figure 6.1. Block diagram of the MMR measurement system, after Zimmermann et al. (2008)

6.1.1. Fluxgate sensor

A wide variety of sensors is currently available and used to measure magnetic fields. Fluxgate magnetometers are chosen to measure the direction and magnitude of magnetic fields. Fluxgates are affordable, rugged and compact. Furthermore, fluxgate sensors provide precision measurements of static and alternating magnetic fields in three axes. This, plus their typically low power consumption makes them ideal for the intended field application.

Fluxgate magnetometers were invented in the 1930s by Victor Vacquier at Gulf Research Laboratories. Vacquier applied them during World War II as instruments for detecting submarines. After the war fluxgate were used to measure shifts in the magnetic patterns on the sea floor and confirmed so placed the theory of plate tectonics. The basic operating mode of fluxgate magnetometers is illustrated in Fig. 6.2 and briefly summarized in the following.

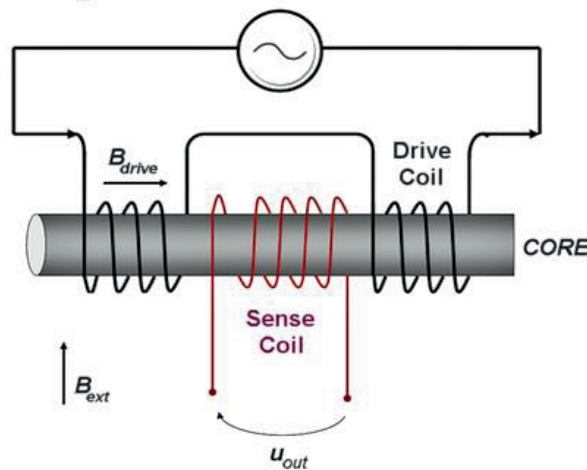


Figure 6.2. Basic operating mode of a fluxgate magnetometer. Drive and sense coil are explained in the text. B_{ext} and u_{out} indicate the external magnetic field and the output voltage of the magnetometer, respectively.

A fluxgate magnetometer consists of a magnetically susceptible, core wrapped by two coils. An alternating electrical current is passed through an inner “drive” coil, driving the core through an alternating cycle of magnetic saturation. This changing field induces an electrical voltage in the second “sense” coil, measured by a detector. In a magnetically neutral background, the output voltage will be symmetrical. However, when the core is exposed to a background field B_{ext} , it will be more easily saturated in alignment with that field and less easily saturated in opposition to it. Hence the alternating magnetic field, and the induced output voltage, will be unsymmetrical. The extent to which this is the case will depend on the

strength of the background magnetic field. Often, the voltage at the output coil is integrated, yielding a voltage u_{out} , proportional to the magnetic field.

The employed Bartington fluxgates Mag-03 (Fig. 6.3) exhibit a measuring range of $\pm 100 \mu\text{T}$, environmentally sealed connectors and are submersible to 100 meters. Moreover, they have a square section, small enough to be suitable in conventional boreholes. Sensor outputs u_i are in the form of three analog voltages from -10 V to +10 V, proportional to B_x , B_y and B_z .



Figure 6.3. Bartington Fluxgate Mag-03. Three-axis borehole sensor with spacers that keep the sensor always in the center of the borehole.

6.1.2. Measuring frequency

Selection of measuring frequency is affected by two major limitations: the inherent noise level of the magnetometer and possible, unwanted induction effects. The noise spectrum of the considered fluxgate sensor Mag-03 exhibits a severe increase for frequencies below 3 Hz (Zimmermann et al., 2008). In addition, the displayed Fourier spectrum (Fig. 6.4) illustrates the significant increase of natural geo-magnetic noise towards low-frequencies. The error due to inductive effects becomes higher than 1 % s for frequencies above 50 Hz. Thus, the optimal measuring frequency is deduced as 25 Hz.

6.2. Lock-in-Amplification

In MMR surveys target signals are periodical and have small amplitudes, generally below 1 nT/A. The frequency spectrum of a typical MMR field data set is shown in Fig. 6.4.

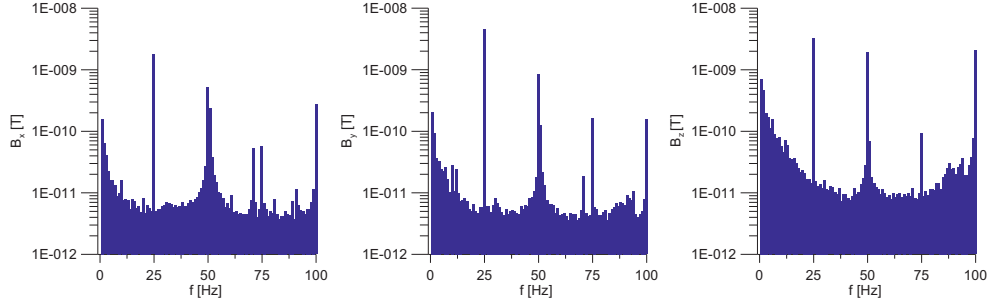


Figure 6.4. Frequency spectrum of the recorded B-field at sensor position $m = 24$ (MNr. 33 specified in the Appendix B), averaged over all employed transmitter configurations for (a) x-component B_x , (b) y-component B_y and (c) z-component B_z .

The total magnetic field, measured by the fluxgate sensors is composed of two major spectrally distinct components: (a) the static Earth's magnetic field (B^E), corresponding to the DC values and (b) a temporally –varying magnetic field at 25Hz. In the following, the fraction, associated with the 25 Hz excitation signal, is referred to as modulation part B^m . The other significant peaks at 50Hz, 75 Hz and 100 Hz are due to power line harmonics. In some cases, the amplitude of the modulation part B^m is only marginally higher than the surrounding noise. Introduction of lock-in-technique allows for measurements of small amplitude, temporarily varying magnetic fields in an environment with high noise level (Verweerd, 2007). The phase-sensitive amplification of the modulation part is based on the mathematical principle that the product of two sine or cosine functions only yields a non-zero value if the frequency is identical. The measured signal $u_i(t)$ is multiplied with a reference signal $r(t)$ of identical shape and frequency. In order to avoid phase errors, all measurement channels are periodically synchronized. Synchronization leads to a spurious slackening of speed of the entire measurement system. Overall measurement period at a single sensor position is increased by approximately 200 %. For future applications, a time reduction is in progress. The output magnetic field B_i is finally determined by the following equation, where i refers to the particular component of the observed signal

$$B_i = \frac{F_1}{I} \frac{1}{t_{int}} \int_0^{t_{int}} u_i(t) r(t) dt \quad (6.1)$$

Here, t_{int} is the integration time and F_1 represents the sensor-specific scaling parameter converting voltage values into equivalent magnetic field values, specified as $F_1 = 10^{-5}$ T/V.

Furthermore, the magnetic field is normalized to the true injection current I that can be calculated according to:

$$I = \frac{I_1 - I_2}{2} \quad (6.2)$$

I_1 and I_2 represent measured values of the current strength, in both current paths. Since the current is measured with shunt-resistors, the voltages U_1 and U_2 across the resistors are actually measured by the system (control unit F01) and equation (6.2) is changed to:

$$I = \frac{1}{2} \left(\frac{U_1}{Z_1} - \frac{U_2}{Z_2} \right) \quad (6.3)$$

6.3. Borehole sensor orientation

The difficulty of an arbitrary sensor orientation in boreholes is supposed to overcome by additionally recording the magnetic field at a reference station at the surface. The magnetic axis of the reference sensor (x_r, y_r, z_r) are assumed to be perfectly aligned with the local coordinate system, described through (X, Y, Z) .

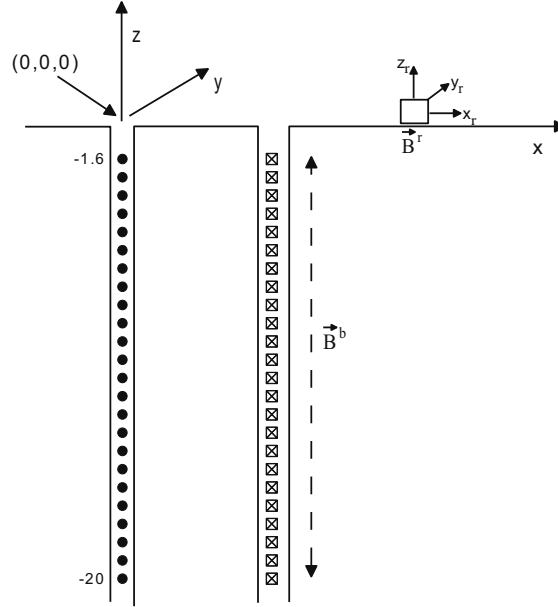


Figure 6.5. Location and orientation of the reference sensor. (X, Y, Z) and (x_r, y_r, z_r) span the local and the sensor coordinate system, respectively. \mathbf{B}^b and \mathbf{B}^r denote magnetic fields, measured with borehole or reference sensor, respectively.

The angular deviation of the borehole sensor is determined by means of Earth's magnetic field data, corresponding to the DC values of the frequency spectrum. These DC values are calculated from the measured voltage signal by averaging over the entire measurement cycle. Due to the sampling rate, a measurement cycle consists of N_m data points. Thus, Earth field values are obtained by:

$$B_i^E = F_1 \frac{1}{N_m} \sum_{j=1}^{N_m} u_{i,j} \quad (6.4)$$

In order to differentiate between borehole and reference station the superscript b and r are introduced. The calculated Earth field values for borehole $B_i^{E,b}$ and reference station $B_i^{E,r}$ as well as the modulation part in the borehole $B_i^{m,b}$ are transferred into Spherical coordinates:

$$(B_\theta, B_\phi, B_R) \leftarrow (B_x, B_y, B_z). \quad (6.5)$$

Thereby, the measured Cartesian components (B_x, B_y, B_z) are transferred into angular displacements B_θ and B_ϕ as well as the magnitude B_R of the corresponding magnetic field. Azimuth B_θ and elevation B_ϕ are angular displacements in radians measured from the positive x -axis, and the x - y plane, respectively. A homogeneous Earth's magnetic field is assumed in the considered subsurface, indicating that

$$B_R^{E,b} = B_R^{E,r}. \quad (6.6)$$

Furthermore, it is supposed that the orientation of the borehole sensor is strictly vertical, indicating that

$$B_\phi^{E,b} = B_\phi^{E,r}. \quad (6.7)$$

The variation of B_ϕ^E and B_R^E , obtained for a typical cross-hole application, are shown in Fig. 6.6. In both cases, the achieved values at the reference station are displayed as solid lines showing only less variation. Error bars indicate the maximum deviation of the borehole values with respect to reference values. Dashed lines indicate in case of B_R^E a deviation of 1 % and in case of B_ϕ^E of 10 %. Results validate the made assumption of a homogeneous Earth field by featuring distinctly less than 1 % variation.

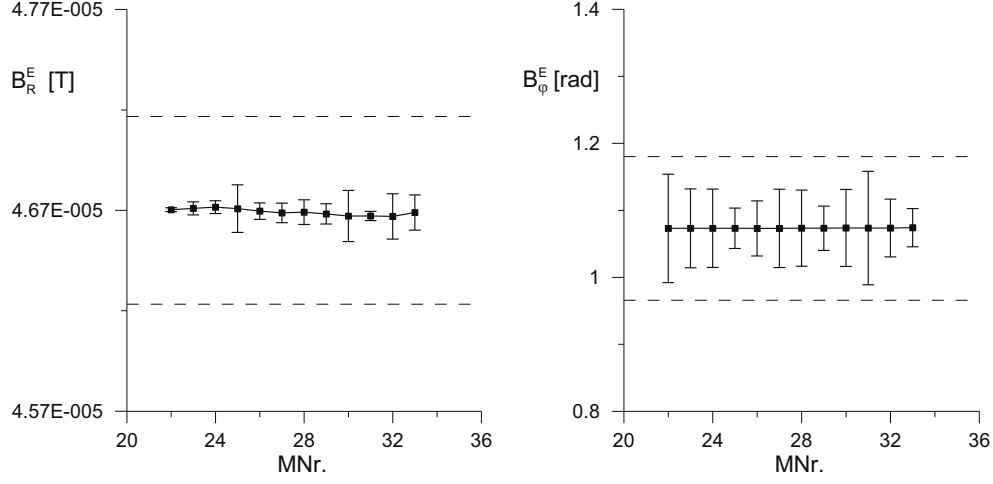


Figure 6.6. Variation of B_R^E and B_ϕ^E obtained during background measurements of the field campaign (Gorgonzola 2006). Error bars indicate maximum deviation between reference and borehole values. Measurement numbers (MNr.) are specified in the Appendix B.

The azimuthal deviation of the borehole sensor orientation with respect to the local coordinate system can therefore be calculated from

$$\vartheta_c = B_\vartheta^{E,b} - B_\vartheta^{E,r}. \quad (6.8)$$

Subsequently, ϑ_c is applied to the azimuthal component of the modulation part $B_\vartheta^{m,b}$ in order to yield the correct value

$$B_{\vartheta_c}^{m,b} = B_\vartheta^{m,b} + \vartheta_c. \quad (6.9)$$

Once calculated, the corrected MMR response, in particular for the y-direction $B_{y_c}^{m,b}$ can be determined by back-transformation into Cartesian coordinates.

$$\left(B_{x_c}^{m,b}, B_{y_c}^{m,b}, B_{z_c}^{m,b} \right) \leftarrow \left(B_r^{m,b}, B_\varphi^{m,b}, B_{\vartheta_c}^{m,b} \right) \quad (6.10)$$

6.4. Minimizing the error due to parasitic correlated noise fields

According to the MMR convention, to this point the MMR response¹ $B^{m,b}$ shall solely consist of magnetic contribution due to the ground and wire. In practice, during preliminary field and laboratory test measurements it became apparent that the so far processed magnetic response contains another systematic noise contribution. The MMR convention is therefore expanded to:

$$B^{m*} = B^m + B_p. \quad (6.11)$$

Here, B^m is the MMR response according to equation (2.5) and B_p is a systematically generated noise field. In MMR surveys, power amplifiers and multi-core cables can generate significant interfering magnetic field that are in-phase with the intended measuring signal (Fig. 6.7). The measurement method with phase switching is intended to avoid errors due to such parasitic correlated magnetic fields B_p . It uses the simple fact that the noise field is generated prior to the actual electrode switching. Hence, B_p is independent of direction of current flow in the subsurface.

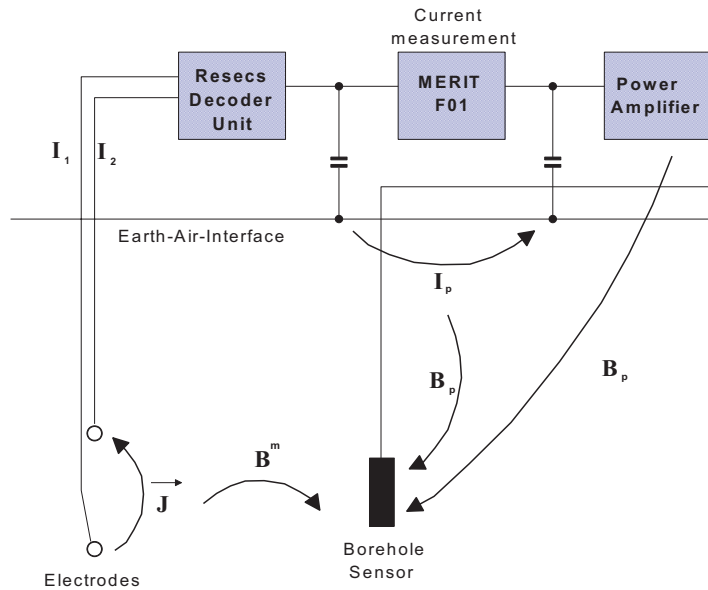


Figure 6.7. Block diagram describing the origin of the parasitic correlated noise field B_p .

¹ Due to simplicity reasons we neglect the subscript y_c in the following.

In order to compensate for the error, caused by B_p , measurements of the magnetic field are repeated for a swapped current injection. The two current modes, normal and reverse, exhibit a phase shift of 180 degrees, indicating that the current flow changes direction. For the theoretical formulation, a symmetrical excitation with $I_1^n = +I_0$, $I_2^n = -I_0$ for normal mode and $I_1^r = -I_0$, $I_2^r = +I_0$ for the reverse mode is assumed. The actual MMR response exhibits a polarity change with $B_{reverse}^m = -B_{normal}^m$. Without loss of generality, this becomes apparent by considering the simple, analytical formulas describing B^w and B_s^g . In contrast, the parasitic magnetic field B_p remains unaffected with the two injection modes. For the MMR response, associated with normal and reverse current mode, is yielded:

$$B_{normal}^{m*} = B_{normal}^m + B_p \quad (6.12)$$

$$B_{reverse}^{m*} = -B_{normal}^m + B_p \quad (6.13)$$

The sum of both data sets yields the true MMR response B^m , normalized to the excited current I_0 :

$$B^m = \frac{B_{normal}^m + B_p}{2I_0} - \frac{-B_{normal}^m + B_p}{2I_0}$$

$$B^m = \frac{B_{normal}^m}{I_0} \quad (6.14)$$

6.5. Reduction for the wire component

By achieving this level of data processing the MMR response merely contains the magnetic contribution of the wire B^w , delivering current from the switching boxes to the respective electrodes, as well as the ground contribution B^g . In practice, the switching boxes are positioned directly on top of the transmitter borehole. Current is transferred to the borehole electrodes via single, parallel connector cables. Thus, the magnetic field measurements are shielded from all wire contributions in the borehole except the straight vertical wire connection between the two considered electrodes of the vertical dipole. Its magnetic contribution is calculated according to the numerical approach, specified in chapter three. According to the MMR convention (2.5), the resultant wire contribution is subtracted from the measured MMR response B^m to yield the ground component B^g :

$$B^g = B^m - B^w \quad (6.15)$$

6.6. Validation of MMR data processing – the “Tank Experiment”

Before the MMR measuring system is used in actual field measurements, a series of laboratory tests was conducted to assess the usefulness of the proposed data processing procedure. In order to study the performance of the whole system in terms of reproducibility of reference responses testing was conducted in a controlled laboratory environment.

For the laboratory setup, the magnetic sensor is assumed to be already fixed aligned according to the local coordinate system. The measured components of the magnetic field represent therefore the true Cartesian components. According to that, the output magnetic field B_i has only to be reduced for the noise field B_p and the wire component B^w . In order to compare the observed and processed magnetic response with analytically calculated values, the measurement setup is designed to simulate a homogeneous half-space. Analytical values for the ground and wire component are determined according to the current filament approach. Due to its simpler experimental implementation, a conventional DHMMR measurement setup with surface excitation and borehole magnetic field measurements is employed. The experimental arrangement of the measurement setup is shown in Fig. 6.8.

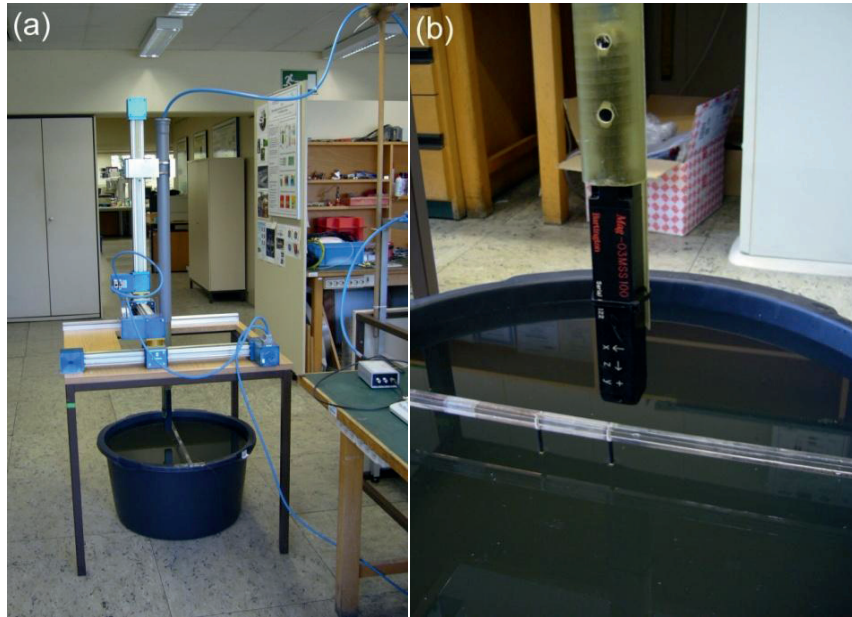


Figure 6.8. The laboratory measurement setup. (a) Water-tank with automatic scanner system and (b) close-up of the current dipole with fluxgate sensor in the back.

A water filled tank of 0.6 m diameter and 0.25 m depth represents the homogeneous medium. In order to excite current at the water surface, a current dipole of 6cm length is used. For this purpose two brass screws are inserted in a Plexiglas rod, which is fixed at 3.5 cm above the water surface. The electrodes are insulated from the rod to the water surface and connected to the measurement system via two thin copper wires. A twisted cable runs between the measurement system and the mid-point between the electrodes in order to shield data acquisition from its contribution. At this mid-point the cable is divided into two copper wires put straight on the rod and connected to the electrodes. The finally recorded MMR response should consist of the desired magnetic field due to primary current flow in the uniform half-space and the straight wire connection between the two electrodes. A three-axis fluxgate sensor (Bartington Mag-03) was mounted on an automatic scanner device. The PC-controlled measurements involve movement of the scanner to precise positions below the water surface, application of a constant voltage signal, and continuous sampling of the resulting magnetic field amplitudes in three components. Close to the PC the components of the MMR measurement system (described in section 6.1.) are located. Repeat measurements were made for each sensor position according to normal and reverse current mode.

For the measurement phase, a local coordinate system is defined. The projection of the mid-point between the electrodes on the water surface represents hereby the origin of the coordinate system. The mid-point is indicated as point P in Fig. 6.9. The Plexiglas rod coincides with the x-direction (Fig. 6.9), while z-direction is directed positively upwards. The positive current electrode ($+I$) is indicated at $x = -0.03$ m, while negative current electrode ($-I$) is positioned at $x = +0.03$ m.

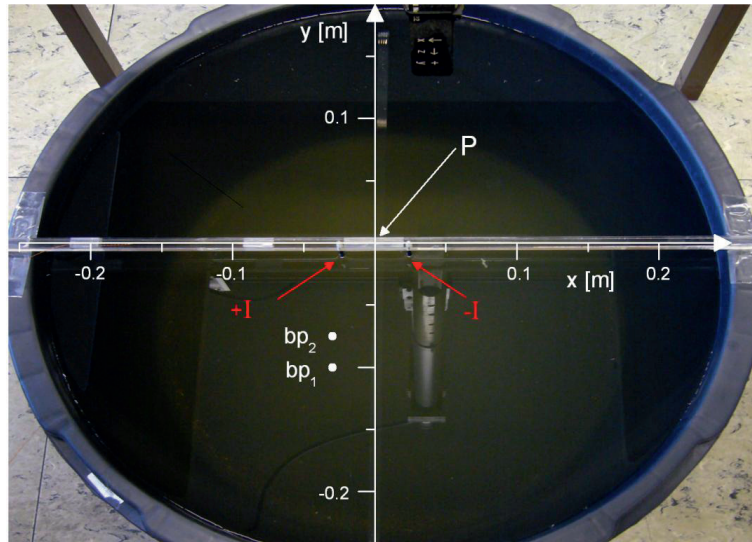


Figure 6.9. Water-filled tank with local coordinate system used for the experimental validation. The two considered borehole profile are indicated by bp_1 and bp_2 .

Magnetic field is recorded along two borehole profiles bp_1 and bp_2 . Due to the small model dimension the exact magnetic sensor axis are determined prior to the actual borehole measurements. For this purpose, the magnetic field along a vertical profile next to a straight, horizontal wire is measured. Due to the symmetry of the magnetic field of the wire, the horizontal component perpendicular to the wire direction will exhibit a zero-crossing while the vertical component exhibits a maximum. In the present case the position of the borehole profiles and the current dipole are not in-plane (Fig. 6.9), causing the ground component B^g to contribute to both the x- and y-component of the measured magnetic field.

The variation of B^g with depth for the two borehole profiles bp_1 and bp_2 is illustrated in Fig. 6.10. Displayed are observed and processed values as points and modeled values as straight line. The horizontal error bars indicate the contribution due to the noise field B_p . First of all, by analyzing the x-component B_x^g (Fig. 6.10a and 6.10b) it becomes apparent that the analytical solution is not valid for positions above the ground surface. Furthermore, an increasing discrepancy between measured and simulated values for B_x^g is observed with increasing depth. This deviation is most likely caused by a sensor itself, representing a large resistive anomaly. For the y-component B_y^g this systematic is less pronounced but clearly visible at least between 0.05 m and 0.15 m depth. Nevertheless, for the near-surface position, not yet affected by the strong sensor anomaly, observed and analytically calculated magnetic fields are in good agreement.

The results prove that MMR field data can successfully be corrected for the interfering noise fields generated by the measurement system B_p and by the wire B^w . The final data processing procedure is displayed as flow chart (Fig. 6.11). The flow chart reveals the complexity of the proposed data processing.

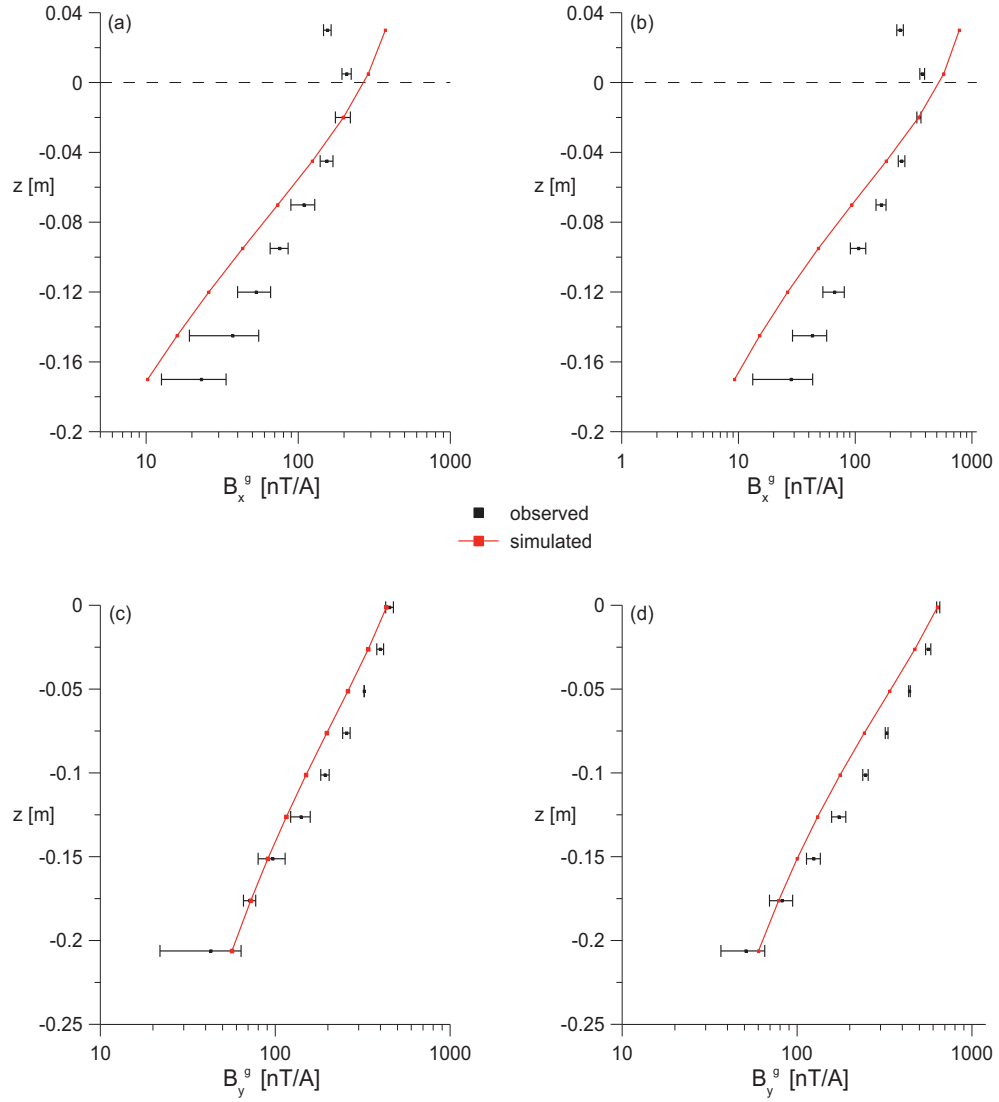


Figure 6.10. Comparison between measured (readily processed) and simulated MMR ground response B^g . (a) B_x^g measured along bp_1 , (b) B_x^g measured along bp_2 , (c) B_y^g measured along bp_1 and (d) B_y^g measured along bp_2 .

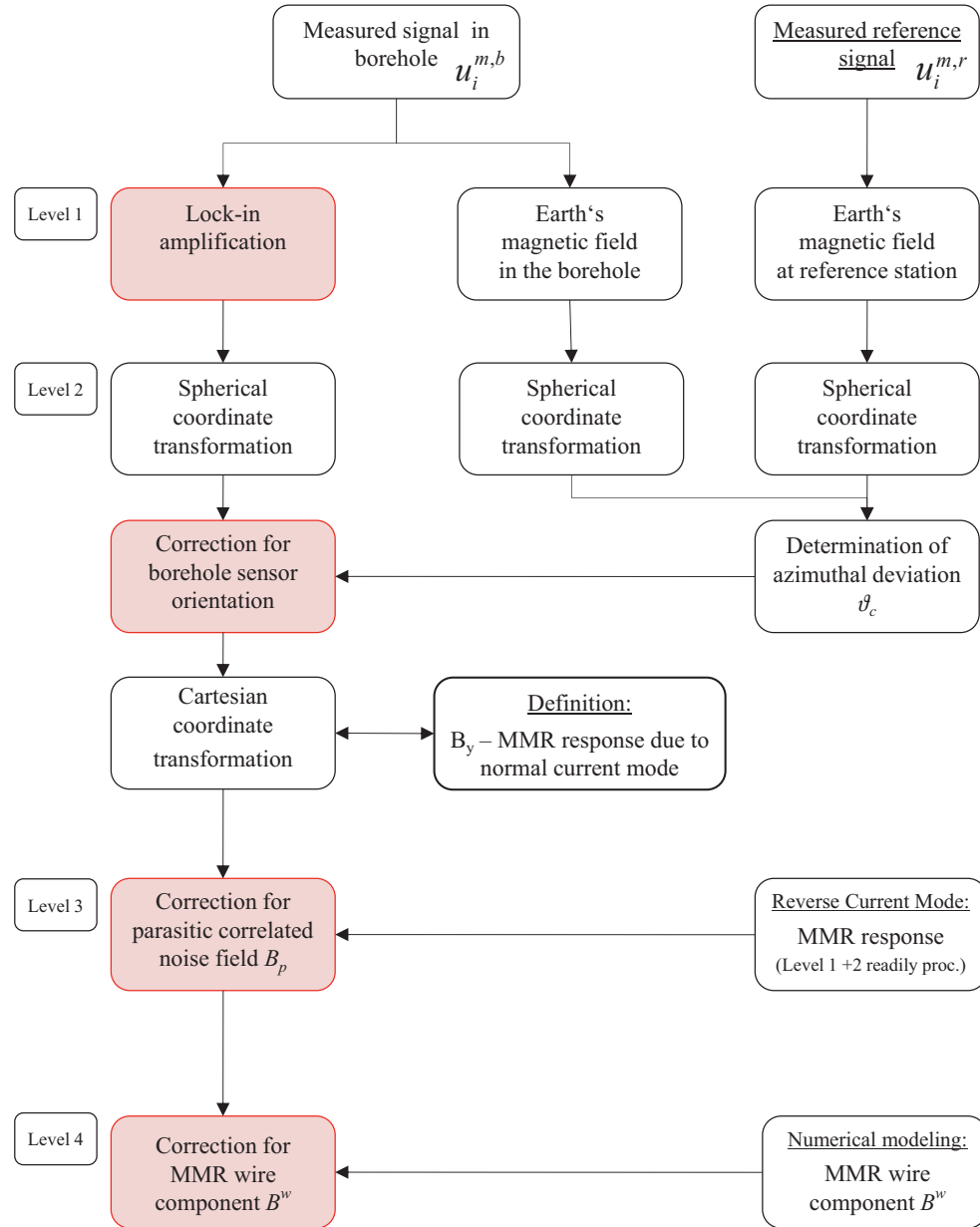


Figure 6.11. Flowchart of the final MMR data processing procedure. The four basic levels of data processing (according to the sections 6.2 – 6.5) are highlighted as red frames.

Chapter 7

Field Example

This chapter describes and discusses the cross-hole MMR data acquired during a water-injection experiment in the unsaturated zone, conducted in Quarternary sediments of the Po River plain. The field site is located in Gorgonzola, east of Milan (Italy). The main dataset collected at the Gorgonzola site is composed of measurements acquired before (background data) and during (time-lapse data) the water injection. In the first part, the test site and the main survey specification are described, followed by the results obtained for background and time-lapse measurements, separately.

7.1. The Gorgonzola field site

The Gorgonzola experimental site was specifically designed for non-invasive cross-hole monitoring of subsurface dynamics with geophysics and consequently for the assessment of vulnerability of the underlying aquifer. In particular, GPR and ERT were used during field surveys from July 2005 to January 2006 (Deiana et al., 2005) and also accompanied the MMR measurements during the described field campaign in June 2006. Moreover, the image obtained from the inversion of independently acquired ERT (background) data composes the data base for the validation of the MMR background data. Detailed information on data acquisition and inversion of the ERT survey are given by Deiana et al. (2005).

7.1.1. Site description

A detailed site description can be found in Deiana et al. (2005), and is here only briefly summarized. The measurement area is situated in an industrial area near a public communication junction. Four boreholes have been drilled up to a depth of 20 m (A-D in Fig. 7.1a). Site stratigraphy is known from an extracted soil core in borehole D and contains at least one remarkable feature namely the existence of 2-m-thick layer of cemented gravel and sand at roughly 12 m depth. This zone has the potential of being a water retaining layer. The other boreholes (A-C) are permanently equipped with 24 stainless-steel electrodes each. The electrodes are vertically spaced by a distance of 0.8 m ranging from 1.6 m to 20 m depth. Boreholes A and B are considered for the actual cross-hole measurement setup (Fig. 7.1b). Due to irrigation in the surrounding countryside, water table has a yearly oscillation between

depths of 13.5 m and 20 m. Actual measurements of the depth to the water table proved that and yielded a depth within A of 18.65 m and within B of 18.63 m.

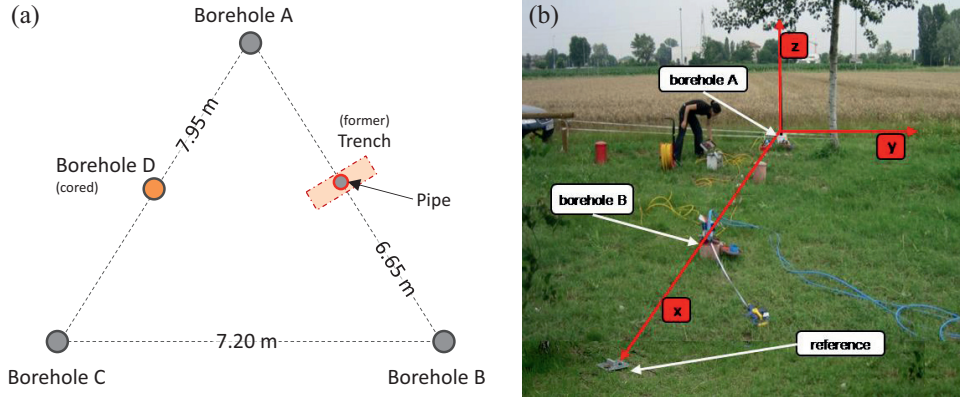


Figure 7.1. The Gorgonzola experimental site with (a) scheme of the borehole locations (redrawn after Deiana et al., 2005) (b) measurement setup with reference station and local coordinate system.

7.1.2. Survey specification

As proposed in Chapter 5, the tomographic measurement approach involves current injection via *v-dipole* configurations in borehole A and three-axis magnetic field readings along borehole B. Measurement density is determined by the 21 feasible transmitter configurations and the 24 equally spaced sensor position ranging likewise from -1.6 m to -20 m depth. According to the proposed correction for the borehole sensor orientation, a third reference sensor is installed at the surface, positioned 2.7 m apart from borehole B (Fig. 7.1b). Since the alignment of the reference sensor is essential to the latter processing, the sensor was fixed installed on a non-magnetic plate equipped with adjustable feet and a position level (Fig. 7.2). Furthermore, borehole sensors are equipped with plastic spacers in order to keep them in the center of the borehole (Fig. 6.2). Finally, data are acquired with the prototype MMR measurement system (section 6.1.) and processed according to the developed proceeding in Chapter 6, schematically illustrated in Fig. 6.12.

During initial test measurements on-site sufficient data quality emerged to be provided by using measurement cycles of 5 sec for each current mode. Measurement uncertainty is deduced by using an integration time $t_{int} = 1$ sec during lock-in-amplification. Given a measurement cycle of 5 sec, data can thereby be considered as five times stacked. By processing these five data subsets independently, a mean value and a standard deviation of the observed ground response is yielded. The derived standard deviation estimates the measurement uncertainty of the respective observation, and is displayed as error bars marked on the field data.



Figure 7.2. Reference sensor (Bartington Mag-03MSSL - low noise version) equipped with level and adjustable feet (not visible here).

The background dataset is composed of measurements according to all possible transmitter-receiver combinations, referred to as total survey in the following. Theoretically, the time needed to complete a total survey is given as 84 min. In order to increase measuring progress, the magnetic field is measured simultaneously with a two-fluxgate array and thus the total time should be halved. In practice, a significant rise in measuring time is still observed. The actually needed time is 2 hours 10 minutes. This large increase is probably due to synchronization times between hardware components. Although survey time is of no relevance for the background measurements, it is an important factor to be considered for the time-lapse measurements due to the fast dynamic of the water injection.

In general, the frequency of acquisition shall be high during and in the first hours after the injection. Since all three employed geophysical methods require high frequency of measurements to capture the hydrological process, survey time is limited during the first day of the experiment. Given the need to acquire data frequently and fast, the number of considered transmitter and sensor positions is considerably reduced for a fast survey. Included combinations of transmitter and sensors are illustrated as ray tomograms in Fig. 7.3 showing that the measurement density is still high above 10 m, while the time needed to complete the fast survey is significantly reduced to 35 min. The main survey specifications are summarized in Table 7.1. An explicit description of all conducted measurements, detailed images of the measurement equipment (e.g. the two-fluxgate array) are to be found in the Appendix B.

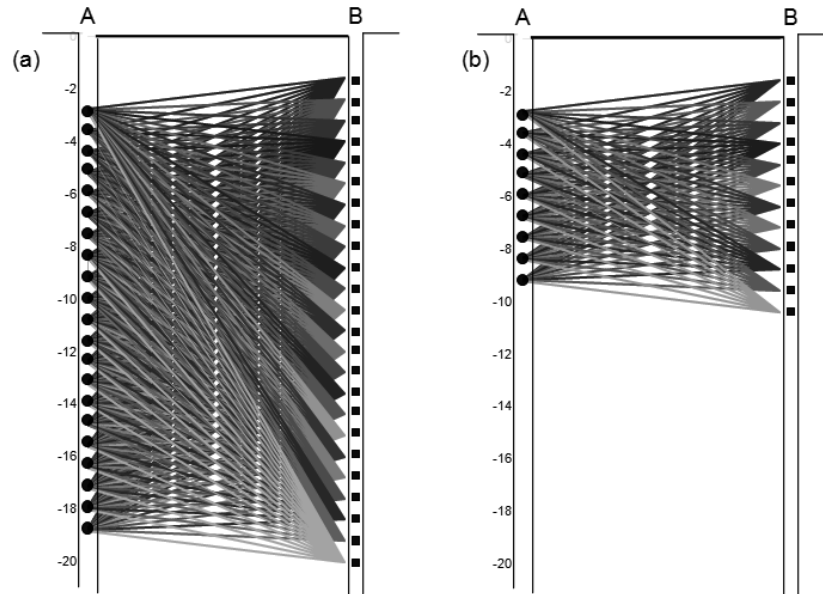


Figure 7.3. Ray tomogram of transmitter-receiver combinations considered for the (a) total and (b) fast survey. Circles and squares indicate transmitter and sensor locations, respectively. For the transmitter configurations, the mean depth of the respective vertical dipole is displayed (as specified in Appendix A).

Borehole sensors	Mag-03 MSS Measuring range: $\pm 100 \mu\text{T}$
Reference sensor	Mag-03MSL70 (low noise version) Measuring range: $\pm 70 \mu\text{T}$
Number of transmitter configurations	21
Number of sensor positions	24
Number of measurement configurations	504 (total) 120 (fast)
True current strengths	0,1 – 0,3 A
Measurement cycles	5 sec
Measuring time	2h 12min (total) 35 min (fast)
Sampling frequency	1 kHz

Table 7.1. Survey specifications for the field campaign in Gorgonzola (Italy) 2006.

7.2. Data validation of background measurements

For the background measurements, readily processed MMR field data are compared to model curves predicted over two conductivity models using the MMR forward modeling program MMRMod (described in Chapter 4). The first model is obtained from the inversion of independently collected ERT data (Fig. 7.4a), referred to as *ERT2MMR* in the following. The second model represents a horizontally stratified subsurface (Fig. 7.4b), referred to as *Layered Earth*, and is a 1D model inferred from the *ERT2MMR* model.

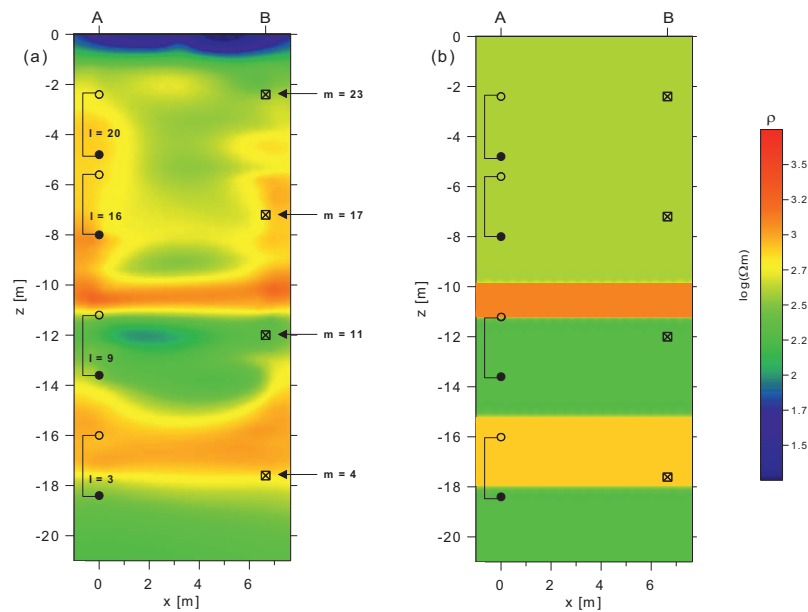


Figure 7.4. Conductivity models (a) *ERT2MMR* and (b) *Layered Earth* used for the validation of background measurements. The locations of transmitter configurations and magnetic sensors considered as representative examples in subsection 7.2.1 and 7.2.2 are indicated in both models as circles and squares, respectively.

The *ERT2MMR* model generally features smooth boundary transitions, while the *Layered Earth* model exhibits sharp contrasts from one layer to the next. Both models confirm the presence of two layers having higher resistivity at depths of about 10 m and 16 m. The area between these two layers is characterized as rather conductive. This layer is probably wetter than the surrounding material, and corresponds to the 2-m-thick layer of cemented gravel and sand. The two models are chosen in order to point out differences and similarities of MMR in relation to ERT. Subsequently, field data are discussed in two ways. At first, the MMR ground response B^g , obtained from field and model data, is displayed as a function of the sensor depth with respect to four exemplarily chosen transmitter configurations. In the second part, data are depicted as a function of the depth of the positive transmitter electrode with

respect to four exemplarily chosen sensor depths. The considered datasets are chosen as representative examples of the most prominent features visible in the data. For the purpose of a complete overview, all field data are represented in conjunction with the corresponding model curves in the Appendix C.

7.2.1. Moving receiver

The four representative examples for a moving-receiver arrangement are displayed in Fig. 7.5. In the first example ($l = 3$), a transmitter configuration located at -18.4 m depth is considered. As illustrated in Fig. 7.4, the dipole extends from rather conductive to rather resistive material. The observed MMR field data exhibit a strong negative response with peak amplitude of up to 6 nT/A. This negative response indicates clearly the depth range of the deep resistive layer (ranging from -15 m to -18 m). Field data favorably compare with the predicted response for the *Layered Earth* model, while the response predicted with the *ERT2MMR* model is significantly too low. From the comparison, it is concluded that the contrast of the resistive layer in relation to the layer below, obtained from the ERT data inversion, is not sufficient. Besides this good agreement between the model curve and the field data obtained for the lower half-space, larger deviations occur for the area above 10 m.

As second example ($l = 9$), field and model data are displayed with respect to a transmitter configuration placed at -13.6 m depth. In this case, current flows from rather resistive to rather conductive medium (Fig. 7.4). Field data show a distinct positive response with peak amplitude of 3 nT/A. The depth range of this positive response corresponds well with the position of the rather conductive sand and gravel layer around 12 m depth. The comparison of the field data with the predicted model curves shows an almost perfect agreement with the *ERT2MMR* model, whereas the data predicted for the *Layered Earth* model are clearly too low. These two examples reveal that the algebraic sign of the gained MMR response obviously depends on the direction of current flow. This result agrees well with the one obtained during the numerical analysis in Chapter 5. Therein, signal strength, obtained for current flowing from a resistive host medium into a conductive body, is positively valued, whereas the sensitivity for a resistive perturbation is negative. Furthermore, analyzing amplitude and shape of the response curves will probably yield information on conductivity gradient and contrast.

As already mentioned, modeled and measured data characterize the zone above 10 m differently. This discrepancy becomes fully apparent regarding a near-surface position of the transmitter configuration ($l = 20$) extending from -4.8 m to -2.4 m depth. Field data feature a distinct negative response with a peak amplitude of 2 nT/A, that is not supported by the model curves. While measured data suggest this additional maximum, approximately at -5 m depth, the model curves exhibit only a smooth change up to the final survey depth of -1.6 m. The origin of this anomaly remains unclear. However, based on the results of the previous two examples, a rather resistive anomaly is expected at this depth.

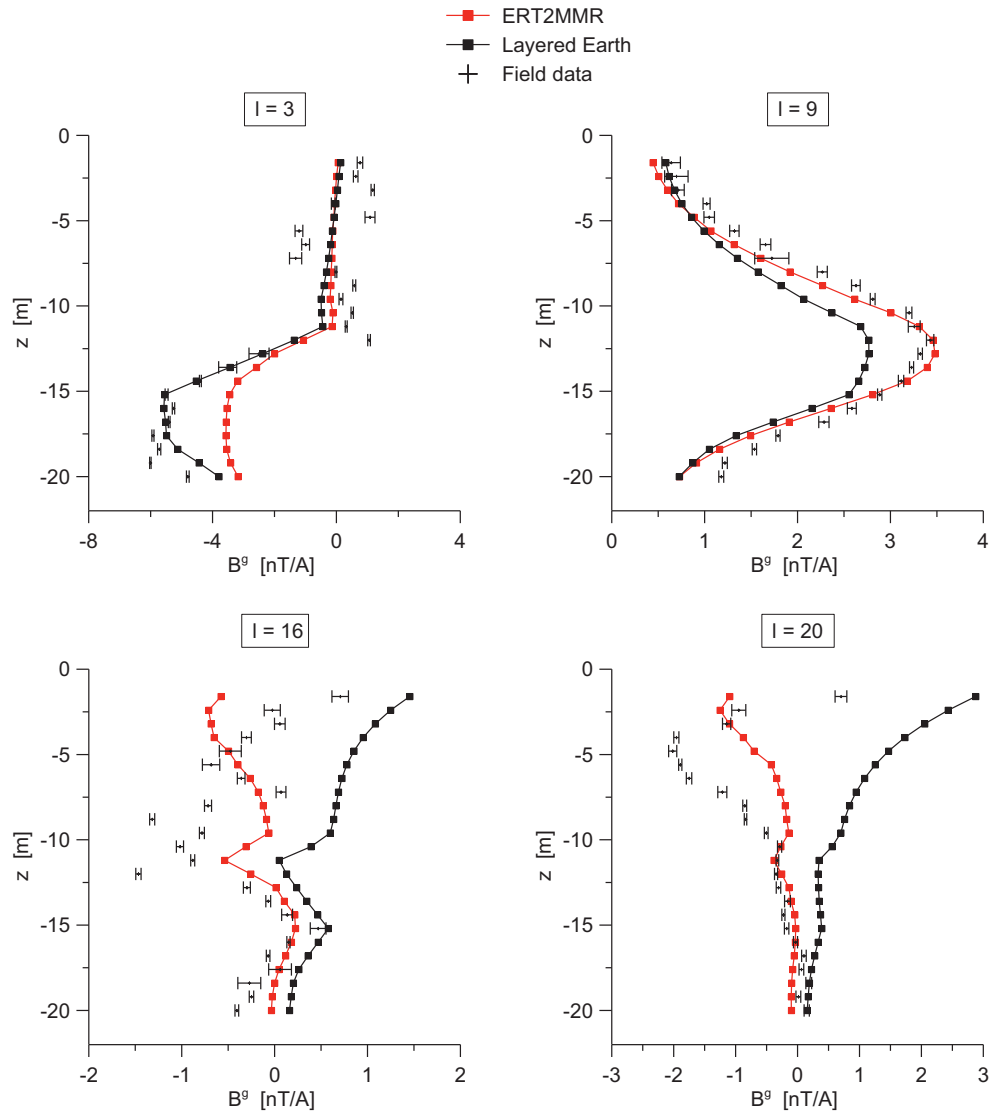


Figure 7.5. Variation of MMR ground response B^g with depth for a moving-receiver setup. Field data are compared to predicted response curves based on models *ERT2MMR* and *Layered Earth*. Locations of the four exemplarily discussed transmitter configurations ($l = 3, 9, 16$ and 20) are specified in Fig. 7.4. Errors bars marked on the field data indicate the measurement uncertainty.

As fourth example, a rather noisy data set is added ($l = 16$) regarding a dipole extending from -8 m to -5.6 m depth. Field data only show a rough agreement with the model curves for the depth below -12 m, whereas for the area above almost no conformity is yielded. While for the depth above -5 m at least a rather continuous progression is visible, field data feature large point-to-point variations in the depth ranging from -6 m to -12 m. The only indication for a possible source of these large deviations is the strong borehole effect noticeable in the ERT image (*ERT2MMR* model) which is situated in a similar depth range. The source of this negative feature partly distorts the overall image pattern and could probably affect also the magnetic field measurements. To further investigate whether these large deviations are artifacts of the actual acquisition, in the following part data are arranged and analyzed with respect to fixed sensor positions. Note that the moving-source arrangement corresponds to the actual acquisition geometry. In practice, the magnetic sensor is moved to a fixed location and the measurement PC automatically cycles through all transmitter configurations (using normal and reverse current mode). The sensor is then moved and the process is repeated. Hence, the difference between these two types of data representation is the actually needed time to acquire the data displayed in one profile. While data acquisition for a fixed sensor position is finished after 12 min, the generation of a full profile for the moving-receiver arrangement needs 2 hours. Therefore, data are rather exposed to random noise for the latter representation.

7.2.2. Moving source

Data arranged according to the moving-source setup are exemplarily discussed for four representative sensor positions (Fig. 7.6). The locations of the magnetic sensors considered as examples ($m = 4, 11, 17$ and 23) are shown in Fig. 7.4.

The first example ($m = 4$) considers a magnetic sensor at -17.6 m depth, positioned at the lower boarder of the resistive layer (Fig. 7.4). As in the transmitter example ($l = 3$) data exhibit a strong negative response with a peak amplitude of 7 nT/A. This example clearly reveals that MMR seems to be able to resolve both the sharp boundary contrast at the lower end and the smooth transition at the top end of the layer. For the descending part of the response peak field data are represented best by the *Layered Earth* model, while for the ascending part field data are online with the *ERT2MMR* response curve.

In the second example ($m = 11$), the magnetic sensor is placed within the conductive layer at -12 m depth. Data exhibit a clear change of sign. For transmitter configurations positioned below -12 m, current flows from resistive to conductive material, and thus MMR ground response B^g is positive. If current injection is accomplished above -12 m, direction of current flow changes (conductive to resistive) and thus B^g becomes negative. The comparison with the model curves shows a good agreement for the lower positive peak, while for the upper negative response both model curves underestimate the observed response. This example again suggests that the gained contrast from the ERT inversion is not sufficient, particularly for the lower boundaries.

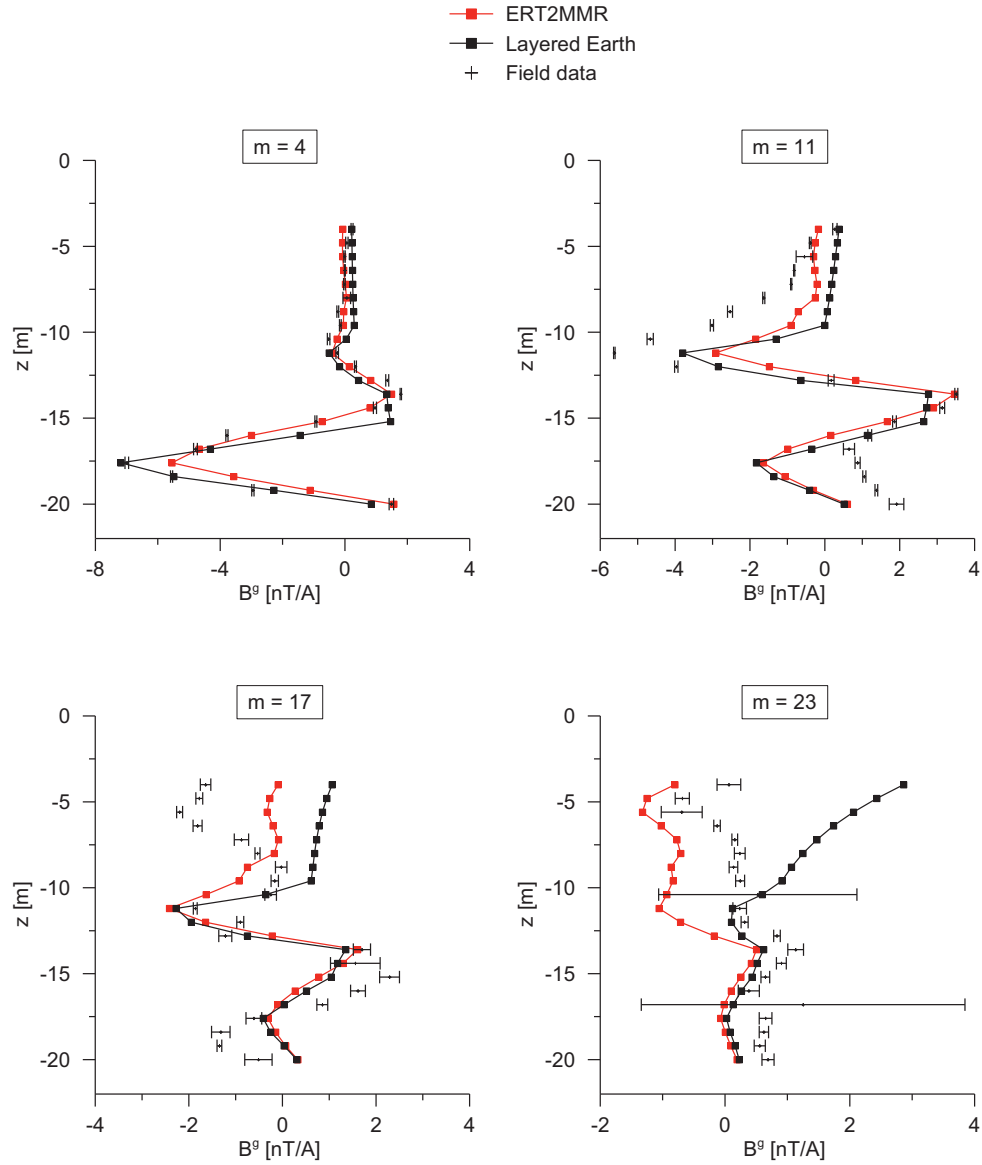


Figure 7.6. Variation of MMR ground response B^g with depth for a moving-source setup. Field data are compared to predicted responses based on models *ERT2MMR* and *Layered Earth*. Location of the four exemplarily chosen magnetic sensors ($m = 4, 11, 17$ and 23) is illustrated in Fig. 7.4. Errors bars marked on field data indicate the measurement uncertainty.

In the third example ($m = 17$), field data again indicate the existence of the resistive anomaly around -5 m depth. The last example ($m = 23$) regards a near-surface sensor position at a depth of -2.4 m. Field data exhibit almost no response but clearly largest measurement uncertainties. From a general inspection of the field data (Fig. 7.6), it becomes apparent that larger measurement uncertainties occur more frequently and to a larger degree while approaching the ground surface. This effect can be explained as near-surface magnetic field measurements are less shielded from EM noise (see Chapter 1) and become also more susceptible to man-made noise contributions. Besides the bad data quality of these examples, the overall inspection of the recorded data (Appendix C) shows that less than 5 % of the data exhibit these intolerable large measurement uncertainties. Data quality is considered as good and could be further improved, if required in terms of data preparation for inversion, by introducing longer measurement cycles.

The comparison of field and model data ($m = 23$) shows another interesting feature. The curve predicted from the *ERT2MMR* model features a weak but distinct negative response over the entire depth range from -4 m to -10 m. This response is likely to be generated by the borehole artifact (visible in the ERT image) that extends over the same depth range. The fact that MMR data exhibit no such negative response could indicate that the MMR data acquisition is generally less affected by the borehole.

These representative examples demonstrate

- that by means of the developed data processing routine data of good quality are provided
- that by means of the forward modeling program *MMRMod* the background data can be analyzed and interpreted

Further research is needed to clarify the origin of larger data errors in terms of measurement uncertainties and point-to-point variations. Potential sources for data errors in general are geomagnetic noise, cable artifacts (deviations from the assumed wire layout), possible interference between specific sensors merged in the fluxgate-array and environmental influences, for instance the nearby train and bus station.

The examples further illustrate the complexity of the acquired MMR responses. Amplitude and shape of obtained response peaks depend on conductivity contrast, direction of current flow (either from resistive to conductive or from conductive to resistive) and relative position of transmitter and sensor to the addressed layer or structure in general. The comparison between measured data and model curves indeed indicates that MMR can contribute additional structural information to the overall cross-hole resolution. In particular, MMR data suggest better resolvability of contrasts.

7.3. Analysis of time-lapse measurements

Time-lapse measurements refer to repeated measurements with time conducted on the same acquisition geometry and are intended to capture the interaction of the static geologic signal, discussed as background MMR ground response B^g , with the dynamic hydrological process. In the following, results are discussed in terms of the anomalous MMR ground response B_s^g caused by the injected water. This anomalous response B_s^g is calculated as difference of the actually measured ground response at a certain time step $B^g(t_i)$ with respect to the initially recorded background response $B^g(t_0)$:

$$B_s^g(t_i) = B^g(t_i) - B^g(t_0)$$

In practice, the evolution of the injected water plume in space and time was monitored for a total of 34 hours and within 7 time steps from June 13 (date of water injection) to June 14, 2006. A total volume of 11 cubic meters of tap water were injected over a period of 9 hours. The timing of the water injection and the monitoring scheme considered for the time-lapse measurements are shown in Fig. 7.7.

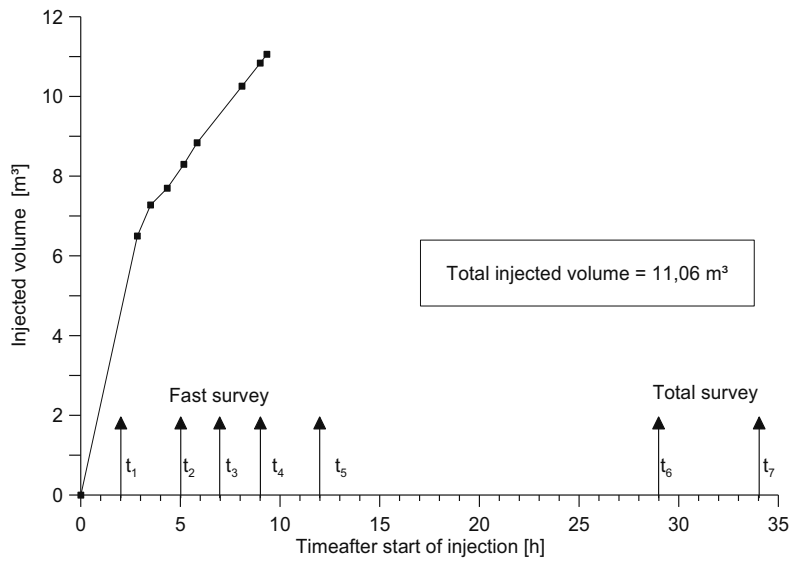


Figure 7.7. Measured volume of injected tap water at the Gorgonzola site during experiment in June 2006 and corresponding survey plan for the time-lapse MMR measurements.

In fact, water injection is realized by pouring water directly into a vertical tube embedded in the ground (Fig. 7.8). The tube extends approximately to a depth of 2 m and is used to skip the shallowest soil layer and allows for an injection of water directly in the natural formation below.

Data are discussed in two ways. The first part will focus on the results obtained during the first day of the experiment, in which data are acquired according to the fast survey. The data representation is therefore limited to the upper 10 m (Fig. 7.10). Secondly, results obtained during the second day of the experiment are presented. Since in this connection measurements according to the total survey are reintroduced, displayed time-lapse responses feature the entire profile depth (Fig. 7.11).



Figure 7.8. Realization of the water injection. Water is infiltrated via an embedded pipe (approx. 2 m depth extension) in order to skip the shallowest soil layer.

Due to the rather continuous developing of the data for the moving-source representation, the time-lapse response curves are shown as function of the depth of the positive transmitter electrode. In both cases, data are exemplarily depicted for five representative sensor positions. The addressed sensor positions for the data analysis are displayed in Fig. 7.9. The chosen datasets feature the most interesting characteristics visible in the data. For the purpose to give a complete overview, all obtained time-lapse responses (during first and second day of the experiment) are to be found in the Appendix D.

The first example ($m = 24$) reveals that for a near-surface sensor position at -1.6 m depth only marginally response amplitudes (generally < 1 nT/A) are generated. The obvious reason for these small amplitudes (for all 5 time steps) is the fact that water is directly injected into larger depths. Besides the small amplitudes, the most significant response is obtained for the second time step ($t_2 = 4$ hours after start of injection).

For a magnetic sensor, located at -4.8 m depth ($m = 20$), already considerably increased values for the anomalous MMR ground response B_s^g are obtained with peak amplitudes of up to 2 nT/A. Furthermore, a clear shift of the maximum peak towards larger depths is observed.

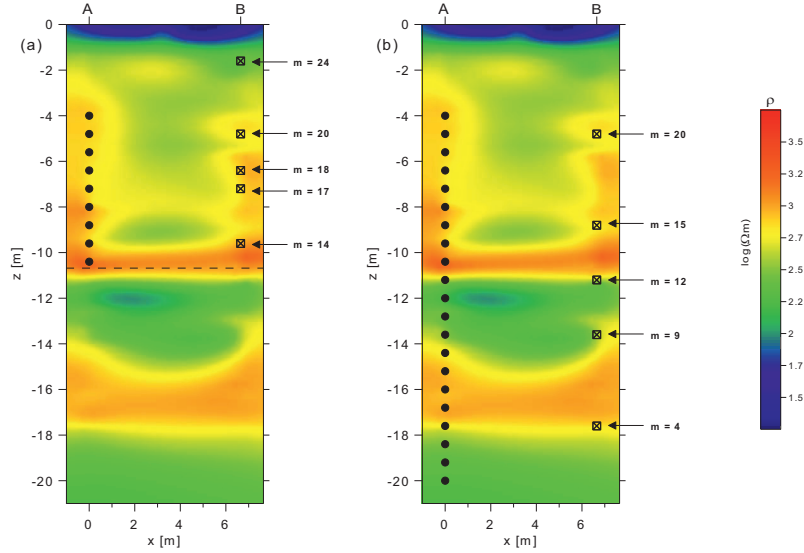


Figure 7.9. Conductivity model *ERT2MMR* with magnetic sensor locations m considered for the analysis of time-lapse measurements acquired during (a) day one and (b) day two. Circles indicate the transmitter electrode positions included in the fast (a) and the total (b) survey.

A similar shift is observed for the consecutive sensor positions $m = 18$ (-6.4 m depth) and $m = 17$ (-7.2 m depth), this time from $t_2 = 4$ h to $t_3 = 7$ h (after start of injection). This shift towards larger depths and later times within the addressed examples is a clear indicator for the vertically downward migrating water plume. In addition, for sensor position $m = 18$ clearly separated zero crossings are observed for each time step ($t_1 - t_5$). From previous examples (Fig. 7.6, $m = 11$) it is known that a zero crossing indicates a boundary between units of different conductivity. In case of time-lapse monitoring of the water injection, the zero crossing of the anomalous MMR response B_s^g is seen as an indicator for the depth of the water front. From the time-lapse monitoring for sensor position $m = 18$, it is therefore inferred that the water front has covered a depth range of 3 m within 7 hours. By contrast, the depth of the maximum peak of a time-lapse response curve is rather related to the center of mass of the injected water plume.

Finally, the last example ($m = 14$) pictures the observed responses for the bottom end of the sensor profile during the first day of the experiment. Again, data exhibit only marginally anomalous MMR responses B_s^g . Interestingly, the maximum response is observed 12 hours after start of injection. By comparing the top and bottom position of the magnetic sensor ($m = 24$ and $m = 14$) the spatiotemporal dependence of the MMR response caused by the injected water volume becomes fully apparent. While for the near-surface position the response maximum is observed already 4 hours after start of injection, for a magnetic sensor, situated 8 m below, the response maximum appears also 8 hours later.

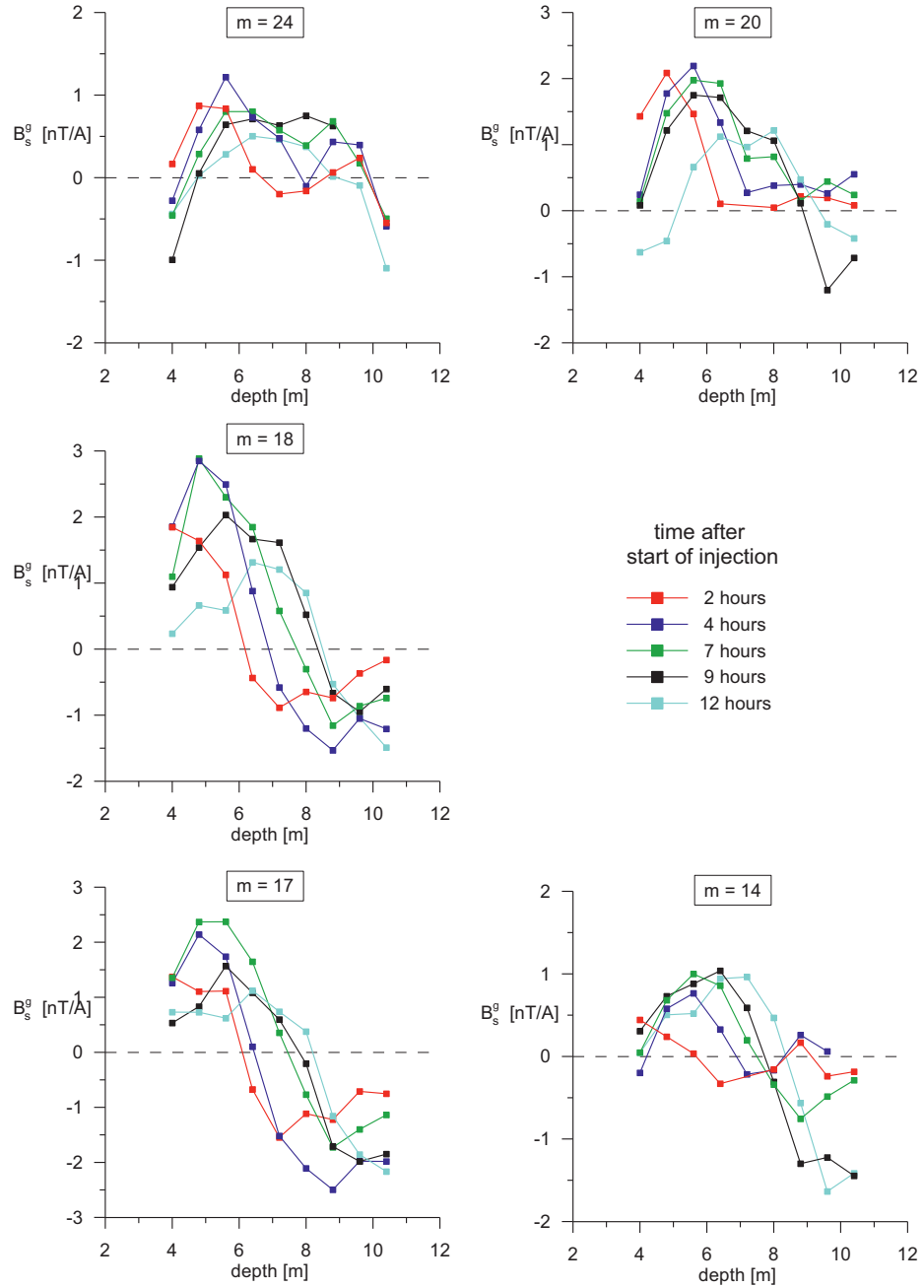


Figure 7.10. Variation of anomalous MMR ground response B_s^g with depth for 5 different time steps during the first day ($t_1 - t_5$). Locations of the 5 exemplarily discussed magnetic sensor positions ($m = 24, 20, 18, 17$ and 14) are specified in Fig. 7.9.

Response curves obtained during the second day, possess different characteristics compared to the first day. Generally, responses for the two time steps ($t_6 - t_7$) exhibit similar shape and feature only little visual difference. For example, the response, observed at a sensor depth of -4.8 m ($m = 20$), features almost no variation of the MMR ground response with respect to the background signal. This disappearance of the signal (for both time steps) for the shallower sensor positions indicates that the water plume has already moved to larger depths or to the sides. The inspection of the anomalous response B_s^g at a medium depth of -8.8 m ($m = 15$) points to a rather dispersed water body. In fact, field data exhibit only marginally higher values compared to $m = 14$ (during the first day – as shown in Fig. 7.9) but for a much larger depth extent from -6 m to -16 m. The expanded depth extension is probably related to the dispersion of the water body.

The next examples ($m = 12$ and $m = 9$) feature the anomalous MMR response B_s^g obtained for two magnetic sensors positioned in the lower half-space, at -11.2 m and -13.6 m depth in the rather conductive sand and gravel layer. For both sensors negative response values are generated in a depth range between -12 m and -16 m, whereas the amplitude is more pronounced for the lower sensor. These two examples indicate that variations in the electrical conductivity distribution also occur for deeper layers. The reason for this feature is not fully understood and requires further research in terms of image reconstruction.

By contrast, the last example ($m = 4$) indicates that for a magnetic sensor positioned below or at the lower end of the deep resistive layer no variation in the electrical conductivity distribution is observed, or at least not for the considered time steps. Water could be ultimately trapped in the cemented sand and gravel layer.

Finally, the evolution of the observed anomalous MMR response B_s^g with time is illustrated in Fig. 7.12. Exemplarily, results for selected transmitter-receiver combinations are displayed. Plot shows temporal evolution for three different depths of the magnetic sensor or transmitter configuration with respect to fixed transmitter or sensor, respectively.

The first example ($l = 19$) shows the temporal variation of the anomalous MMR response B_s^g with respect to a fixed transmitter configuration at -5.6 m depth and for three depths of the magnetic sensor (Fig. 7.11a). All three curves exhibit a significant positive peak during the first 12 hours after start of water injection. The maximum peak features a distinct shift to later times with increasing depth of the magnetic sensor (from $m = 21$ to $m = 19$), which is a clear indication for the vertically downward migrating water body. Since B_s^g already converges towards zero after the first 12 hours, it can be concluded that the water plume has passed the geometrical center of the considered transmitter-receiver combinations.

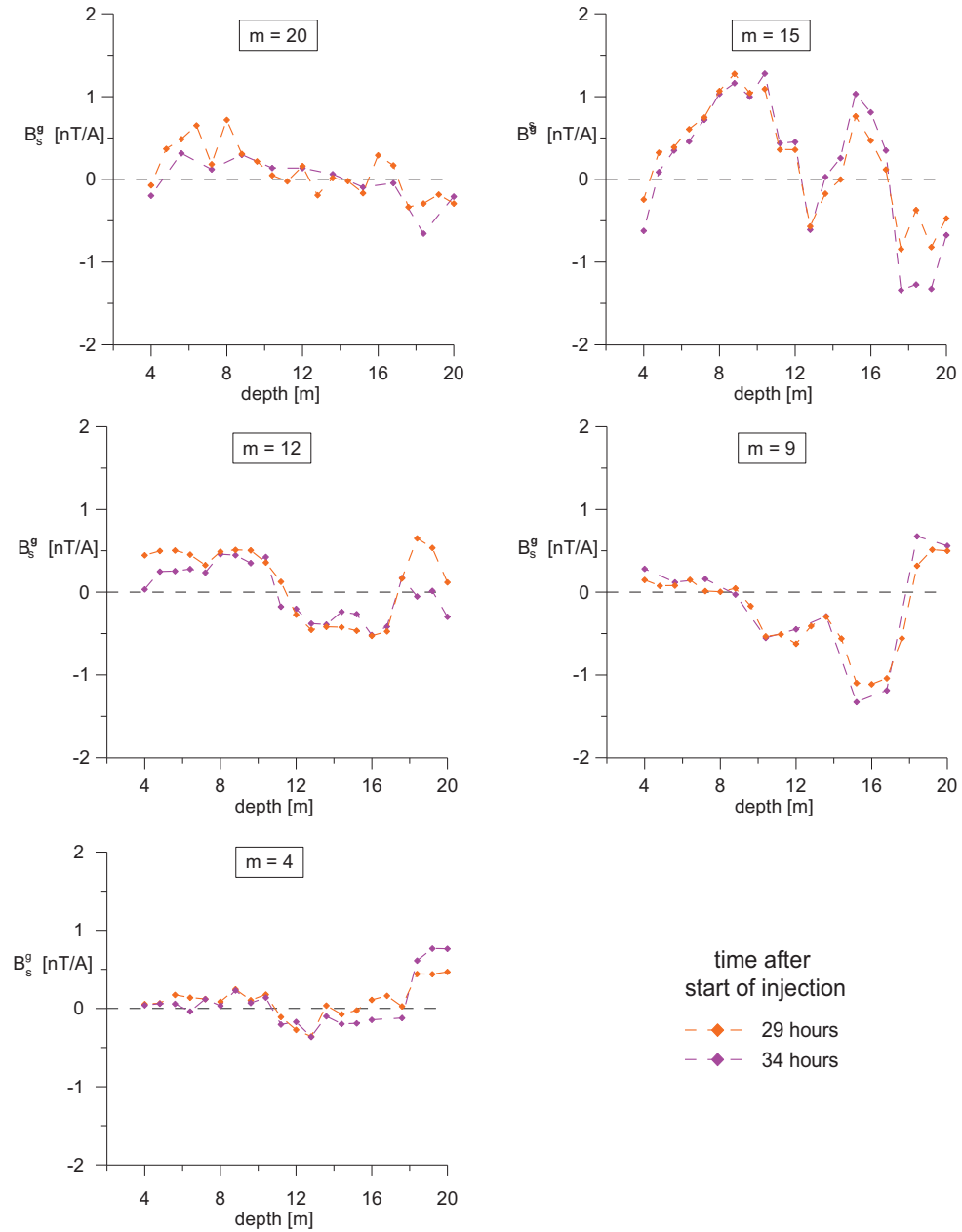


Figure 7.11. Variation of anomalous MMR ground response B_s^g with depth for two different time steps during the second day ($t_6 - t_7$). Locations of the 5 exemplarily discussed magnetic sensor positions ($m = 20, 15, 12, 9$ and 4) are specified in Fig. 7.9.

By contrast, the second example ($m = 18$) features the results with respect to a fixed sensor position and varying depth of the transmitter configuration (Fig. 7.11b). The curves obtained for $l = 19$ and $l = 20$ feature similar behavior as discussed in the first example. The shape of the third curve ($l = 16$) significantly differs from the other displayed examples. Field data exhibit negative values for the first time steps ($t_1 - t_3$) indicating that the water plume hasn't reached the center of maximum sensitivity of this particular (transmitter-receiver) combination. The following reversal for later times confirms the downward movement of the water plume. Due to the missing of additional time-steps between 12 h and 29 h (after start of injection) it remains unclear, whether the positive maximum would have been more pronounced within this period.

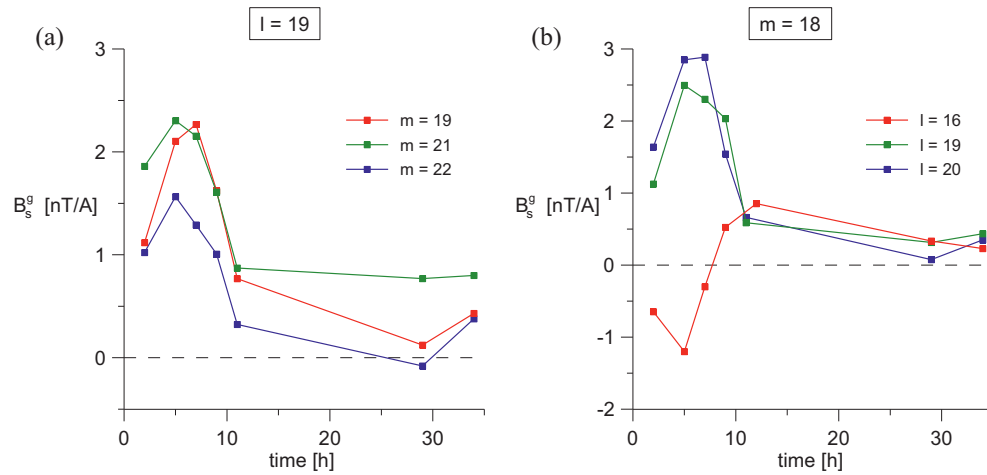


Figure 7.12. Variation of anomalous MMR ground response B_s^g with time for fixed transmitter-receiver combinations. Response curves are displayed with respect to (a) the fixed transmitter configuration $l = 19$ and (b) the fixed sensor position $m = 18$ and three different depths of the sensor or transmitter, respectively.

To sum up, the injected water volume causes significant MMR anomalies that bear a distinct spatiotemporal dependence and could therefore probably contribute to an advanced structural characterization as required for hydrogeophysical purposes.

Chapter 8

Summary and Recommendation

In this chapter a summary of the results and a discussion around several recommendations is given, leading to a possible outline for future research on cross-hole MMR. With the successful field application a working prototype of the cross-hole MMR system is completed. The implemented 2D cross-hole arrangement accommodates three-component measurements of the magnetic field in one borehole due to low-frequency (25 Hz) current injection in another borehole. The presented tomographic approach involves arrays of both transmitter electrodes and magnetic sensors in order to image the area between the two boreholes, separated by 5-10 m, with high resolution. The tomographic layout allows for spatially dense data sampling and enables the detection of even small-scale variations in the electrical resistivity distribution. The large number of individual measurement configurations, inherent in the tomographic setup, is intended to enable high-resolution image reconstruction.

Optimal survey parameters were inferred from numerical studies regarding signal strength and source-generated noise level. It could be proven that current injection via vertical dipoles (*v-dipole*) provides superior signal-to-noise ratio in comparison to horizontal dipoles (*h-dipole*) and single poles (*s-pole*). With a view to good resolution in tomographic surveys the resolving power of different transmitter configurations was analyzed in terms of sensitivity distributions. The spatial distributions illustrate that dipole configurations reflect confined subsurface volumes whereas the *s-pole* configuration covers a rather large depth range of equal sensitivity. While h-dipoles sample only the area around the borehole, *v-dipole* configurations exhibit substantial sensitivity in the middle of the cross-hole region. Furthermore, analyzing sensitivity maps showed that transmitter-receiver combinations, exceeding a vertical offset equal to the borehole separation, do not contribute significantly to the overall cross-hole resolution. Two possible optimization approaches are conceivable. In order to raise survey speed, sensor locations, exceeding a certain vertical offset, are discarded from the overall survey plan. The total number of measurement configurations is reduced and thus, less time needed to complete the survey. Otherwise in terms of improved resolution, one could keep the number of sensor locations fixed but rearrange them restricted to the depth range from $+r$ to $-r$ offset. This could certainly help to better resolve anomalous peaks and results would be less susceptible to measurement errors and noise level.

Laboratory testing as well as experiences from other branches of electrical tomography assisted and validated the development of an appropriate data processing procedure for MMR field data. Concepts for solving two major difficulties inherent in cross-hole MMR field surveying are presented: first the correction for the arbitrary borehole sensor orientation. The concept follows the idea of calculating the deviation angle between the actual measurement direction and a known reference direction. The re-orientation of the borehole sensor works properly, but demands further research and validation especially regarding the adopted assumption for the elevation displacement. The second concept, the measurement method with phase switching, corrects for the parasitic correlated noise fields induced by the measurement system itself. The method was originally developed to improve measuring accuracy for the electrical impedance tomography (EIT) by Zimmermann et al. (2007). In the present research, this technique was first-time successfully applied to laboratory and field data processing. In addition, the proposed data processing routine includes modern lock-in-technique and conventional correction for the wire current, and proved to be an appropriate tool for an effective information extraction from the measured total magnetic field.

In 2006, MMR data were first-time acquired and processed according to the developed tomographic approach and processing routine, respectively. During this field campaign, data were collected in time-lapse mode in order to monitor a water infiltration experiment across the Gorgonzola field site. As is known from literature, no such application has been published yet. By means of the initially acquired background data, it could be shown that 2D cross-hole MMR provides distinct response curves over the considered subsurface. Importantly, the comparison of processed MMR field data with responses predicted on the basis of an independently obtained ERT image, suggests better resolvability of contrasts by MMR than by ERT. Moreover, the analysis of the time-lapse measurements shows spatiotemporal dependence of the MMR response curves upon the water saturation. The anomalous MMR response due to the injected water volume exhibits significant peak amplitudes of up to 3 nT/A. Decay curves for fixed transmitter-receiver combinations clearly reveal that the temporal movement of the water plume is indeed detectable by MMR measurements conducted in time-lapse mode. The almost entire disappearance of the anomalous MMR signal also indicates that the water slug practically has disappeared one day after the injection. Thus, MMR has proven to be a feasible and valuable method for the purpose of hydrogeophysical monitoring.

Technical problems remain present, for instance the increase in survey time due to hardware synchronization. The current development of the measurement system is directed towards a reduction of these delay times. Such an optimization could enable a better applicability to several acquisition targets and survey approaches, e.g. the combined use with other geophysical methods. Apart from the usefulness of the MMR method, measurements of the magnetic field are limited in application with metallic objects (metal pipes or vessels for instance). These (ferro)-metallic objects interfere in two ways: first due to the presence of eddy currents in the objects which distort the magnetic field lines. Secondly the anomalous

magnetic properties, in particular the magnetic permeability μ^1 , will cause magnetic responses on the same scale as signals due to the current injection (for review see Ludwig et al., 2004). Since these effects can not be separated, no clear imaging of the electrical conductivity is possible in that case.

Finally, to complete the adaptation of MMR to cross-hole imaging a fundamental inversion algorithm is needed. The general goal of the inversion is to find a conductivity distribution that can reproduce the observed data to a certain degree. In contrast to forward modeling, inversion techniques of MMR data are less developed. Nevertheless, Fathianpour et al. (2005b) describe a successful inversion algorithm for 2D resistivity structures. The employed numerical inversion uses a Marquardt-Levenberg approach and quasi-Newton updating of the Jacobian matrix. Future application of MMR to hydrogeophysical imaging shall consider the reconstruction of 3D resistivity distribution. Generally, the solution of the inverse problem is constrained by insufficient available information and data noise. The employed tomographic approach and sufficiently long measurement cycles allow for a minimization of the impact due to these constraints. The solution of the inverse problem in MMR is additionally hindered by the strong inherent non-uniqueness, since MMR is only sensitive to conductivity contrasts. LaBreque et al. (2003) include ERT data in a joint inversion approach to overcome the inherent non-uniqueness of MMR data inversion. Even a limited number of independent ERT data is capable to provide an initial guess of the background conductivity distribution. The introduction of a coupled use with the DC resistivity method as suggested by the field data, may further improve the imaging capability.

Alternatively to the evaluation of MMR amplitudes, phase shift data have been previously obtained in MMR surveys and the data have been reported in terms of the Magnetic Induced Polarization (MIP) response (for review *see* Seigel, 1974). MIP is related to MMR in the same senses that IP resembles the DC resistivity method (Telford et al., 1990). In general, IP data are related to the complex resistivity. The current MMR measurement system is already designed to measure the complex resistivity distribution. In addition to the amplitude of the MMR response the lock-in technique provides the phase shift of the measured MMR data with respect to the reference signal. Practical surveys employing the MIP method are reported by previous authors, e.g. for surface exploration Boggs et al. (1998) and borehole exploration Bishop et al (1997). However, apart from Purss et al. (2003) and Chen & Oldenburg (2003), numerical models assisting with the interpretation of MIP surveys have not been recognized. While Chen & Oldenburg (2003) formulated the inverse problem as an optimization problem, Purss et al. (2002) employed a pseudo-3D algorithm to interpret downhole MIP data, based on a variation of the Cole-Cole relaxation model (Xiong & Tripp, 1995). They successfully used phase and amplitude of DHMMR data to explore massive sulphide deposits. Besides this successful application of an iterative technique, future work is needed to characterize and

¹ A general assumption in MMR modeling and data interpretation is that μ is equal to that of free space μ_0 .

understand the MIP response of borehole MMR data in a 3D setting. Nevertheless, the introduction of MIP possibly increases the resolution of IP surveys in a similar way as MMR supports ERT.

For future applications, an integrated approach evaluating amplitude and phase of MMR and ERT data is likely to generate high-resolution images as required for the monitoring in environmental investigations. Such an approach is advantageous in that it commonly results in a more comprehensive characterization of a suite of different physical properties of the target.

Appendix A

Indexing scheme

The exact positions according to the transmitter index l and the magnetic sensor index m , used during numerical studies (standard model – Chapter 4 and 5) and during the field application (in Chapter 7), are listed in the Table A.1. Electrodes and sensors are located in the vertical x-z-plane ($y = 0$) and along the vertical profiles at $x = 0$ m (transmitter electrodes in borehole A) and $x = 6.65$ m (magnetic sensors in borehole B).

Nr.	depth of magnetic sensor m	depth of transmitter configuration l			
		positive transmitter electrode ¹ $+I$	negative current electrode $+I$		mean depth of the v -dipole
			v -dipole	h -dipole ²	
1	-20.0 m	-20.0 m	-17.6 m	-20.0 m	-18.8 m
2	-19.2 m	-19.2 m	-16.8 m	-19.2 m	-18.0 m
3	-18.4 m	-18.4 m	-16.0 m	-18.4 m	-17.2 m
4	-17.6 m	-17.6 m	-15.2 m	-17.6 m	-16.4 m
5	-16.8 m	-16.8 m	-14.4 m	-16.8 m	-15.6 m
6	-16.0 m	-16.0 m	-13.6 m	-16.0 m	-14.8 m
7	-15.2 m	-15.2 m	-12.8 m	-15.2 m	-14.0 m
8	-14.4 m	-14.4 m	-12.0 m	-14.4 m	-13.2 m
9	-13.6 m	-13.6 m	-11.2 m	-13.6 m	-12.4 m
10	-12.8 m	-12.8 m	-10.4 m	-12.8 m	-11.6 m
11	-12.0 m	-12.0 m	-9.6 m	-12.0 m	-10.8m
12	-11.2 m	-11.2 m	-8.8 m	-11.2 m	-10.0 m
13	-10.4 m	-10.4 m	-8-0 m	-10.4 m	-9.2 m
14	-9.6 m	-9.6 m	-7.2 m	-9.6 m	-8.4 m
15	-8.8 m	-8.8 m	-6.4 m	-8.8 m	-7.6 m
16	-8-0 m	-8-0 m	-5.6 m	-8-0 m	-6.8 m
17	-7.2 m	-7.2 m	-4.8 m	-7.2 m	-6.0 m
18	-6.4 m	-6.4 m	-4.0 m	-6.4 m	-5.2 m

¹ Note, all transmitter configurations (v -dipole, h -dipole, s -pole) share the same positive transmitter electrode.

² Negative transmitter electrodes of h -dipole configurations are located at $x = 6.65$ m.

19	-5.6 m	-5.6 m	-3.2 m	-5.6 m	-4.4 m
20	-4.8 m	-4.8 m	-2.4 m	-4.8 m	-3.6 m
21	-4.0 m	-4.0 m	-1.6 m	-4.0 m	-2.8 m
22	-3.2 m			-3.2 m	
23	-2.4 m			-2.4 m	
24	-1.6 m			-1.6 m	

Table A.1. Index scheme references - Exact positions of transmitter electrodes and magnetic sensors indicated by indices ***l*** and ***m*** .

Appendix B

Extended survey specifications

This chapter illustrates in detail the proceeding during the field campaign 2006. The Gorgonzola experimental site is located near a public train and bus station (Fig. B.1).



Figure B.1. Gorgonzola test site (Italy).

In order to increase measuring progress, magnetic field sensing is conducted with a two-fluxgate array. For this reason, two fluxgate sensors were merged non-switched with fixed spacing of 0.8 m (Fig. B.2). Furthermore, borehole sensors were equipped with plastic spacers in order to keep them centrally aligned. In addition, the various hardware components of the MMR measurement system are shown in Fig. B3.



Figure B.2. Preparation of the two-fluxgate array.

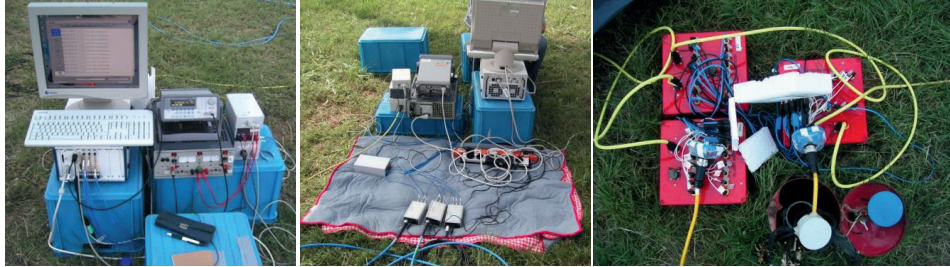


Figure B.3. MMR measurement system (front and back view) and Resecs switching boxes at the top of borehole A (from left to right).

B.1. Background measurements

The background measurements are conducted according to the total survey, including all feasible transmitter-receiver combinations. In addition, Table B.1 indicates that magnetic field is measured simultaneously at two sensor positions.

MNr.	Magnetic sensor position m	Transmitter configuration(s) N_c	Remarks
Background measurement A_0			
MD022	1-2	21 ($l = 1 - 21$)	Total Survey Time: 2h 10 min
MD023	3-4	21 ($l = 1 - 21$)	
MD024	5-6	21 ($l = 1 - 21$)	
MD025	7-8	21 ($l = 1 - 21$)	
MD026	9-10	21 ($l = 1 - 21$)	
MD027	11-12	21 ($l = 1 - 21$)	
MD028	13-14	21 ($l = 1 - 21$)	
MD029	15-16	21 ($l = 1 - 21$)	
MD030	17-18	21 ($l = 1 - 21$)	
MD031	19-20	21 ($l = 1 - 21$)	
MD032	21-22	21 ($l = 1 - 21$)	
MD033	23-24	21 ($l = 1 - 21$)	

Table B.1. Measurement numbers (MNr.) and survey specifications for initial background measurement.

B.2. Time-lapse measurements

The evolution of the water plume is monitored during the time-lapse measurements. Water injection is realized by means of a vertically, embedded tube (Fig. B.4). By skipping the shallowest soil layer water is directly injected into the natural formation below.



Figure B.4. Water infiltration operation.

Water movement is monitored for a total of 34 hours after start of injection and for 7 time steps t_i . The temporal variation of the injected water volume and the corresponding survey plan for the time-lapse MMR measurements is shown in Fig. B.5. In Table B.2 and B.3 the corresponding measurement configurations are listed.

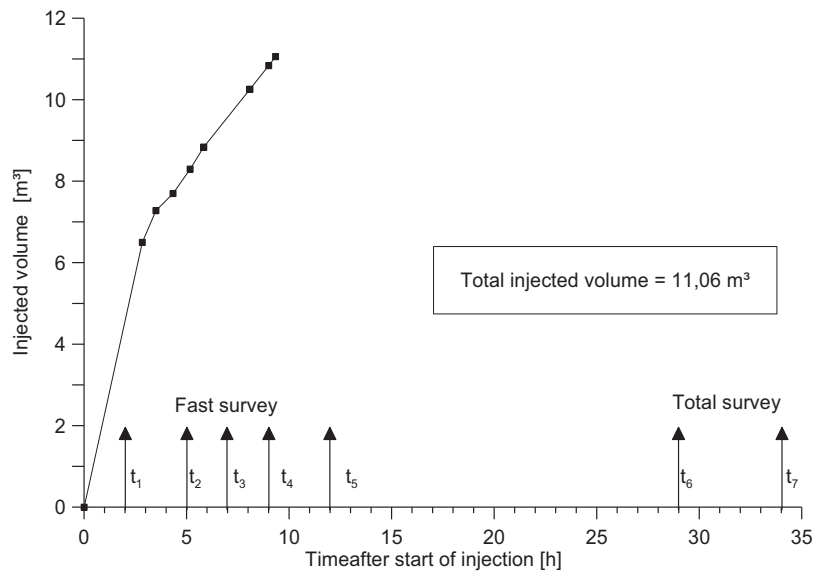


Figure B.5. Measured volume of injected water at the Gorgonzola site during infiltration experiment (June 2006) and corresponding survey plan for time-lapse MMR measurements.

MNr.	Magnetic sensor position <i>m</i>	Transmitter configuration(s) N _c	Remarks
Time-lapse measurement t ₁			
MD046	11-12	9 (<i>l</i> = 13 – 21)	start of reduced survey: 2 hours after start of water injection
MD047	13-14	9 (<i>l</i> = 13 – 21)	
MD048	15-16	9 (<i>l</i> = 13 – 21)	
MD049	17-18	9 (<i>l</i> = 13 – 21)	
MD050	19-20	9 (<i>l</i> = 13 – 21)	
MD051	21-22	9 (<i>l</i> = 13 – 21)	
MD052	23-24	9 (<i>l</i> = 13 – 21)	
Time-lapse measurement t ₂			
MD053	11-12	9 (<i>l</i> = 13 – 21)	start of reduced survey: 5 hours after start of water injection
MD054	13-14	9 (<i>l</i> = 13 – 21)	
MD055	15-16	9 (<i>l</i> = 13 – 21)	
MD056	17-18	9 (<i>l</i> = 13 – 21)	
MD057	19-20	9 (<i>l</i> = 13 – 21)	
MD058	21-22	9 (<i>l</i> = 13 – 21)	
MD059	23-24	9 (<i>l</i> = 13 – 21)	
Time-lapse measurement t ₃			
MD060	7-8	9 (<i>l</i> = 13 – 21)	additional data (not relevant)
MD061	9-10	9 (<i>l</i> = 13 – 21)	
MD062	11-12	9 (<i>l</i> = 13 – 21)	
MD063	13-14	9 (<i>l</i> = 13 – 21)	start of reduced survey: 7 hours after start of water injection
MD064	15-16	9 (<i>l</i> = 13 – 21)	
MD065	17-18	9 (<i>l</i> = 13 – 21)	
MD066	19-20	9 (<i>l</i> = 13 – 21)	
MD067	21-22	9 (<i>l</i> = 13 – 21)	
MD068	23-24	9 (<i>l</i> = 13 – 21)	

MNr.	Magnetic sensor position <i>m</i>	Transmitter configuration(s) N _c	Remarks
Time-lapse measurement t ₄			
MD069	7-8	9 (<i>l</i> = 13 – 21)	additional data (not considered)
MD070	9-10	9 (<i>l</i> = 13 – 21)	
MD071	11-12	9 (<i>l</i> = 13 – 21)	
MD072	13-14	9 (<i>l</i> = 13 – 21)	start of reduced survey: 9 hours after start of water infiltration
MD073	15-16	9 (<i>l</i> = 13 – 21)	
MD074	17-18	9 (<i>l</i> = 13 – 21)	
MD075	19-20	9 (<i>l</i> = 13 – 21)	
MD076	21-22	9 (<i>l</i> = 13 – 21)	
MD077	23-24	9 (<i>l</i> = 13 – 21)	
Time-lapse measurement t ₅			
MD078	1-2	21 (<i>l</i> = 1 – 21)	Total survey: Additional data
MD079	3-4	21 (<i>l</i> = 1 – 21)	
MD080	5-6	21 (<i>l</i> = 1 – 21)	
MD081	7-8	21 (<i>l</i> = 1 – 21)	
MD082	9-10	21 (<i>l</i> = 1 – 21)	
MD083	11-12	21 (<i>l</i> = 1 – 21)	
MD084	13-14	21 (<i>l</i> = 1 – 21)	Start of reduced survey: 12 hours after start of water infiltration
MD085	15-16	21 (<i>l</i> = 1 – 21)	
MD086	17-18	21 (<i>l</i> = 1 – 21)	
MD087	19-20	21 (<i>l</i> = 1 – 21)	
MD088	21-22	21 (<i>l</i> = 1 – 21)	
MD089	23-24	21 (<i>l</i> = 1 – 21)	

Table B.2. Measurement numbers (MNr.) and survey specifications for time-lapse measurements $t_1 - t_5$ (first day).

MNr.	Magnetic sensor position m	Transmitter configuration(s) N_c	Remarks
Time-lapse measurement t_6 (29 hours after the start of water injection)			
MD090	3-4	21 ($l = 1 - 21$)	Total survey –
MD091	5-6	21 ($l = 1 - 21$)	
MD092	7-8	21 ($l = 1 - 21$)	
MD093	9-10	21 ($l = 1 - 21$)	
MD094	11-12	21 ($l = 1 - 21$)	
MD095	13-14	21 ($l = 1 - 21$)	Unfortunately, sensor positions 1 and 2 were omitted due to limited time and no expected change in this area
MD096	15-16	21 ($l = 1 - 21$)	
MD097	17-18	21 ($l = 1 - 21$)	
MD098	19-20	21 ($l = 1 - 21$)	
MD099	21-22	21 ($l = 1 - 21$)	
MD100	23-24	21 ($l = 1 - 21$)	
Time-lapse measurement t_7 (34 hours after the start of water injection)			
MD111	1-2	21 ($l = 1 - 21$)	Total survey – Sensor positions 23 and 24 were omitted due to limited time and no expected change in this area.
MD110	3-4	21 ($l = 1 - 21$)	
MD109	5-6	21 ($l = 1 - 21$)	
MD108	7-8	21 ($l = 1 - 21$)	
MD107	9-10	21 ($l = 1 - 21$)	
MD106	11-12	21 ($l = 1 - 21$)	
MD105	13-14	21 ($l = 1 - 21$)	
MD104	15-16	21 ($l = 1 - 21$)	
MD103	17-18	21 ($l = 1 - 21$)	
MD102	19-20	21 ($l = 1 - 21$)	
MD101	21-22	21 ($l = 1 - 21$)	

Table B.3. Measurement numbers (MNr.) and survey specifications for time-lapse measurement $t_6 - t_7$ (second day).

Very special thanks go to all the field workers that participated and helped during the field campaign 2006 in Gorgonzola (Italy).



Figure B.6. Participants of the 2006 Gorgonzola field campaign.

Appendix C

Validation of background measurements

For the purpose to give a complete overview, all measured data (during the initially conducted background measurement) are displayed in this chapter. Field data are qualitatively validated on the basis of two different conductivity models (Fig. C.1).

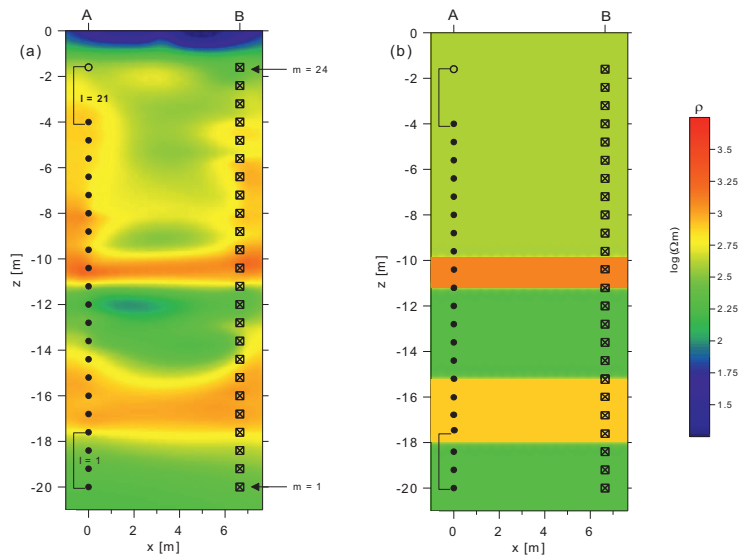


Figure C.1. Conductivity models *ERT2MMR* (a) and *Layered Earth* (b) used for the predication of model curves.

C.1. Moving-receiver

Field data are depicted in two ways. At first, the MMR ground response B^g obtained from field and model data is displayed as a function of the magnetic sensor depth with respect to all transmitter configurations considered in the total survey (Fig. C.2 – C.5). As mentioned before, this type of presentation is referred to as moving-receiver arrangement. Error bars marked on the field data indicate calculated measurement uncertainty.

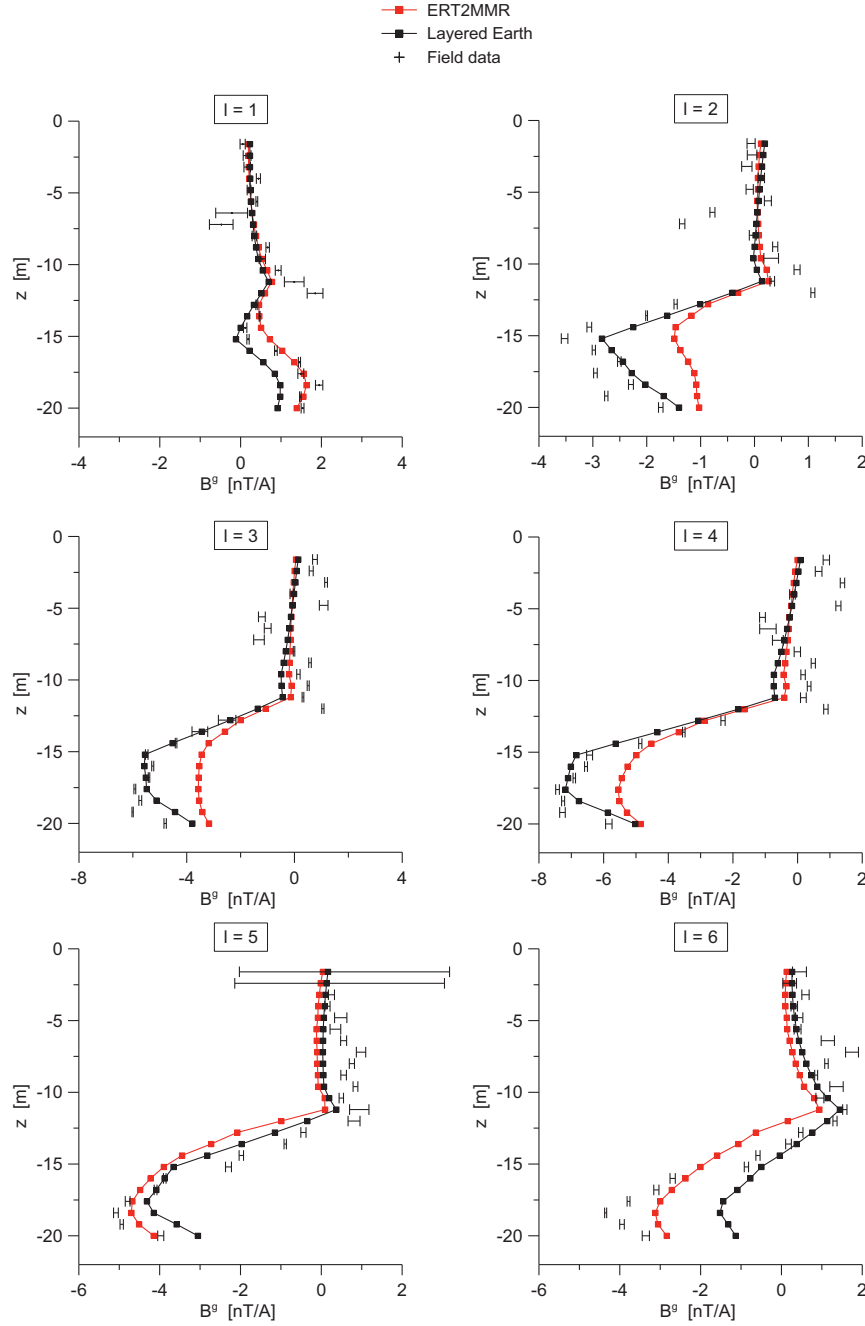


Figure C.2. Variation of MMR ground response B^g with depth for moving-receiver setup. Field data are compared to predicted responses, based on *ERT2MMR* and *Layered Earth* models, with respect to fixed transmitter positions $l = 1 - 6$.

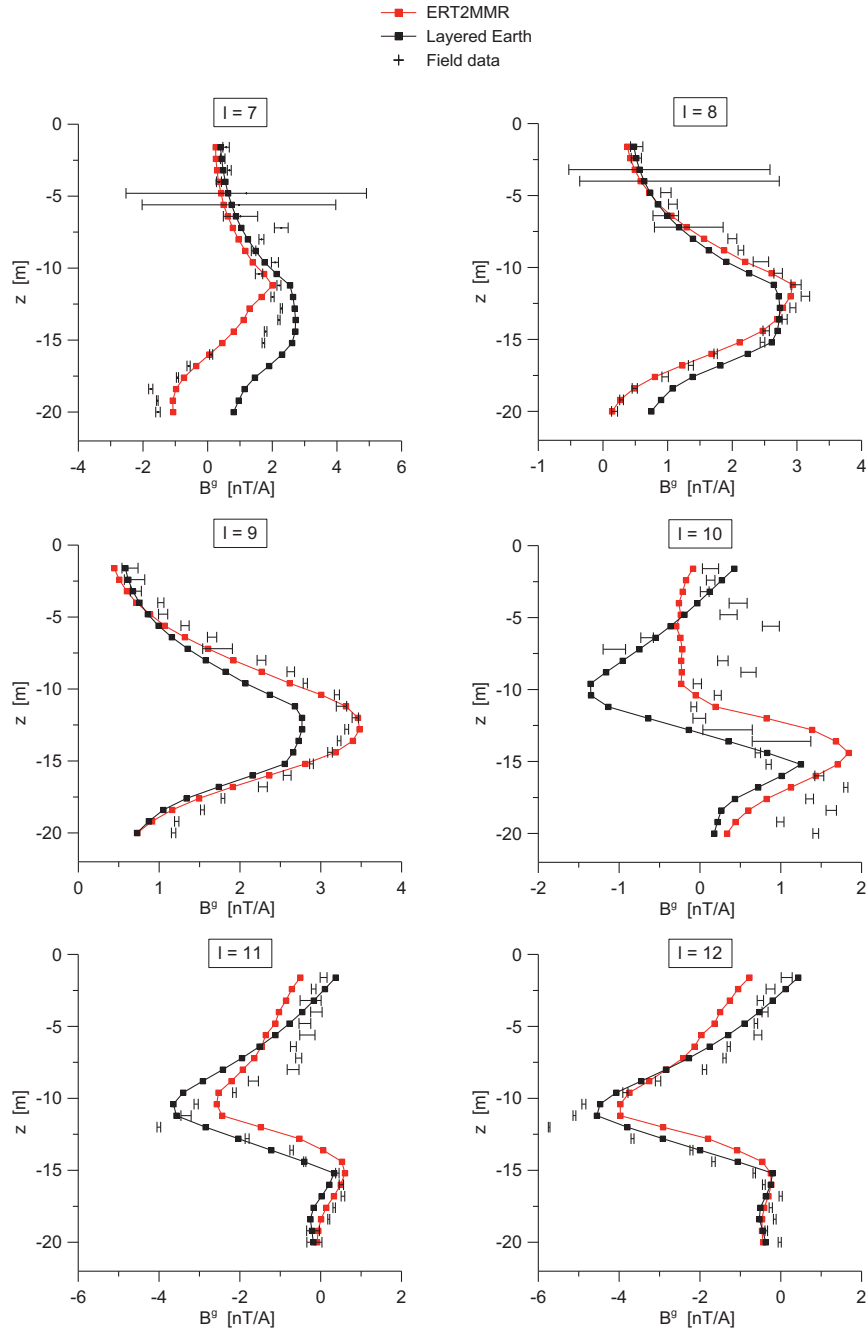


Figure C.3. Variation of MMR ground response B^g with depth for moving-receiver setup. Field data are compared to predicted responses, based on *ERT2MMR* and *Layered Earth* models, with respect to fixed transmitter positions $l = 7 - 12$.

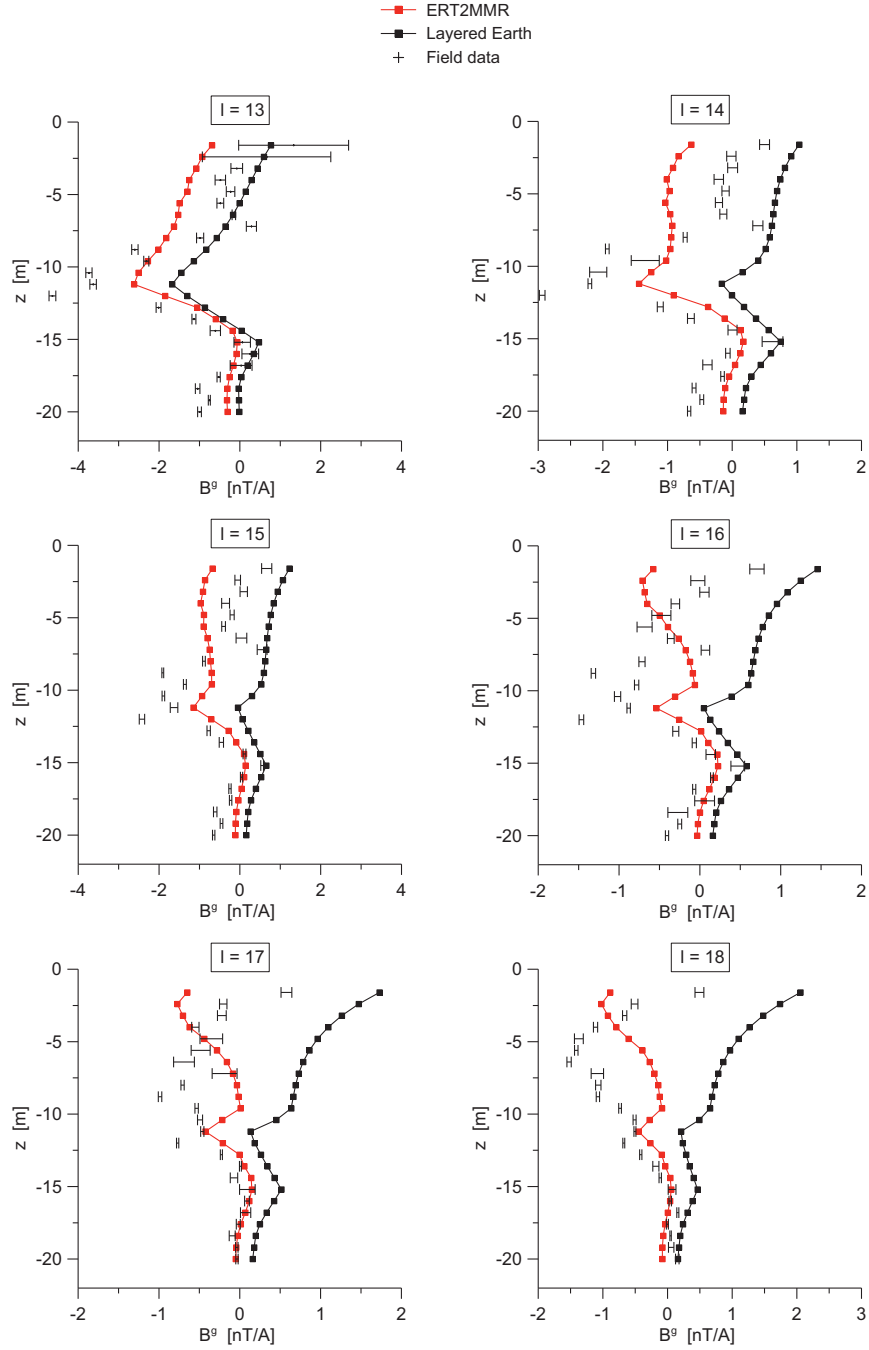


Figure C.4. Variation of MMR ground response B^g with depth for moving-receiver setup. Field data are compared to predicted responses, based on *ERT2MMR* and *Layered Earth* models, with respect to fixed transmitter positions $l = 13 - 18$.

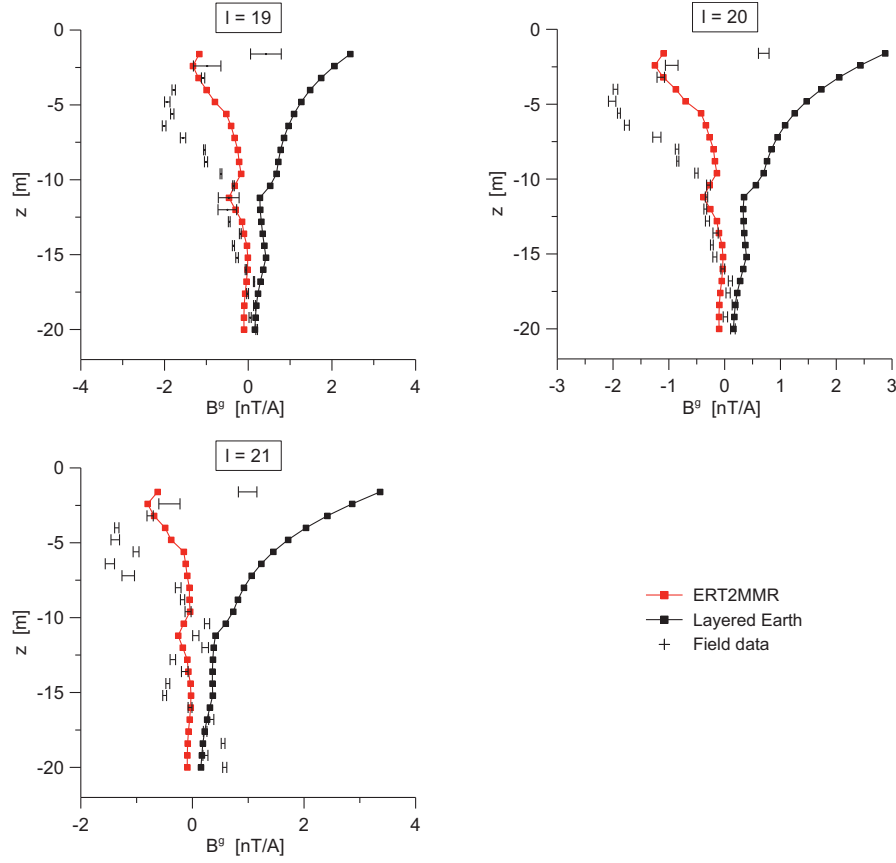


Figure C.5. Variation of MMR ground response B^g with depth for moving-receiver setup. Field data are compared to predicted responses, based on *ERT2MMR* and *Layered Earth* models, with respect to fixed transmitter positions $l = 19 - 21$.

C.2. Moving-source

In the second part, the MMR ground response B^g obtained from field and model data is displayed as a function of the depth of the transmitter electrode with respect to all 24 sensor positions considered in the total survey (Fig. C.6 – C.9). Error bars marked on the field data indicate calculated measurement uncertainty.

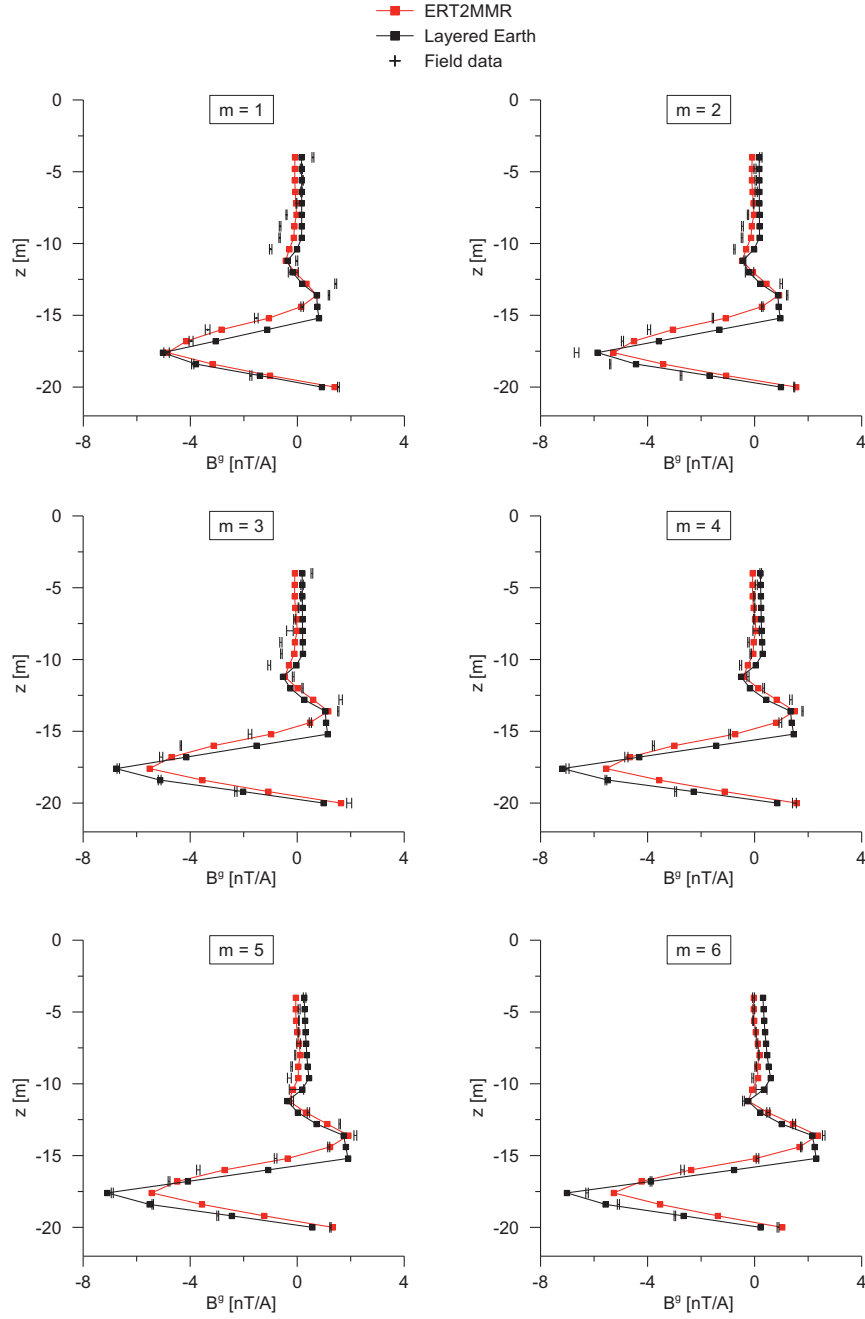


Figure C.6. Variation of MMR ground response B^g with depth for moving-source setup. Field data are compared to predicted responses, based on *ERT2MMR* and *Layered Earth* models, with respect to fixed magnetic field sensor positions $m = 1 - 6$.

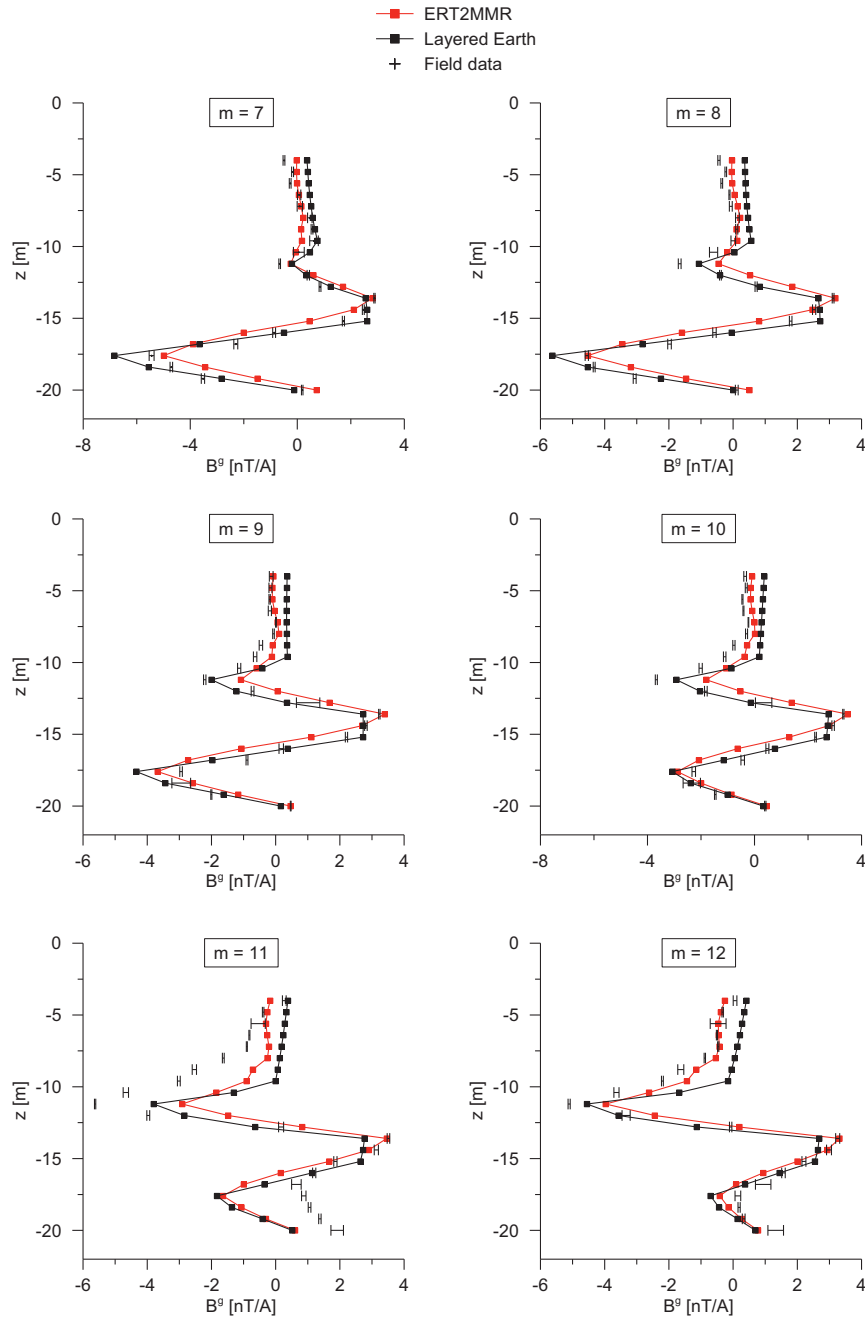


Figure C.7. Variation of MMR ground response B^g with depth for moving-source setup. Field data are compared to predicted responses, based on *ERT2MMR* and *Layered Earth* models, with respect to fixed magnetic field sensor positions $m = 7 - 12$.

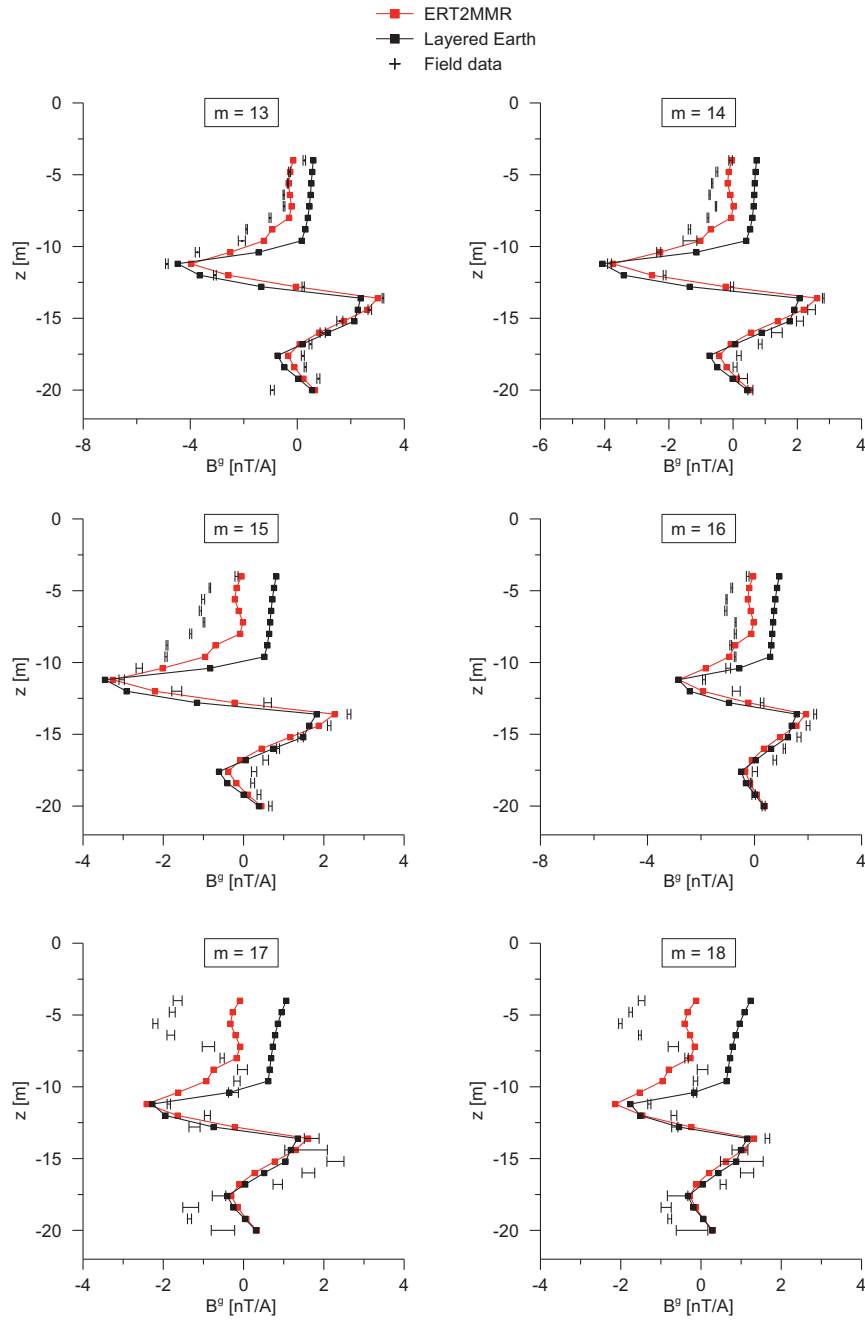


Figure C.8. Variation of MMR ground response B^g with depth for moving-source setup. Field data are compared to predicted responses, based on *ERT2MMR* and *Layered Earth* models, with respect to fixed magnetic field sensor positions $m = 13 - 18$.

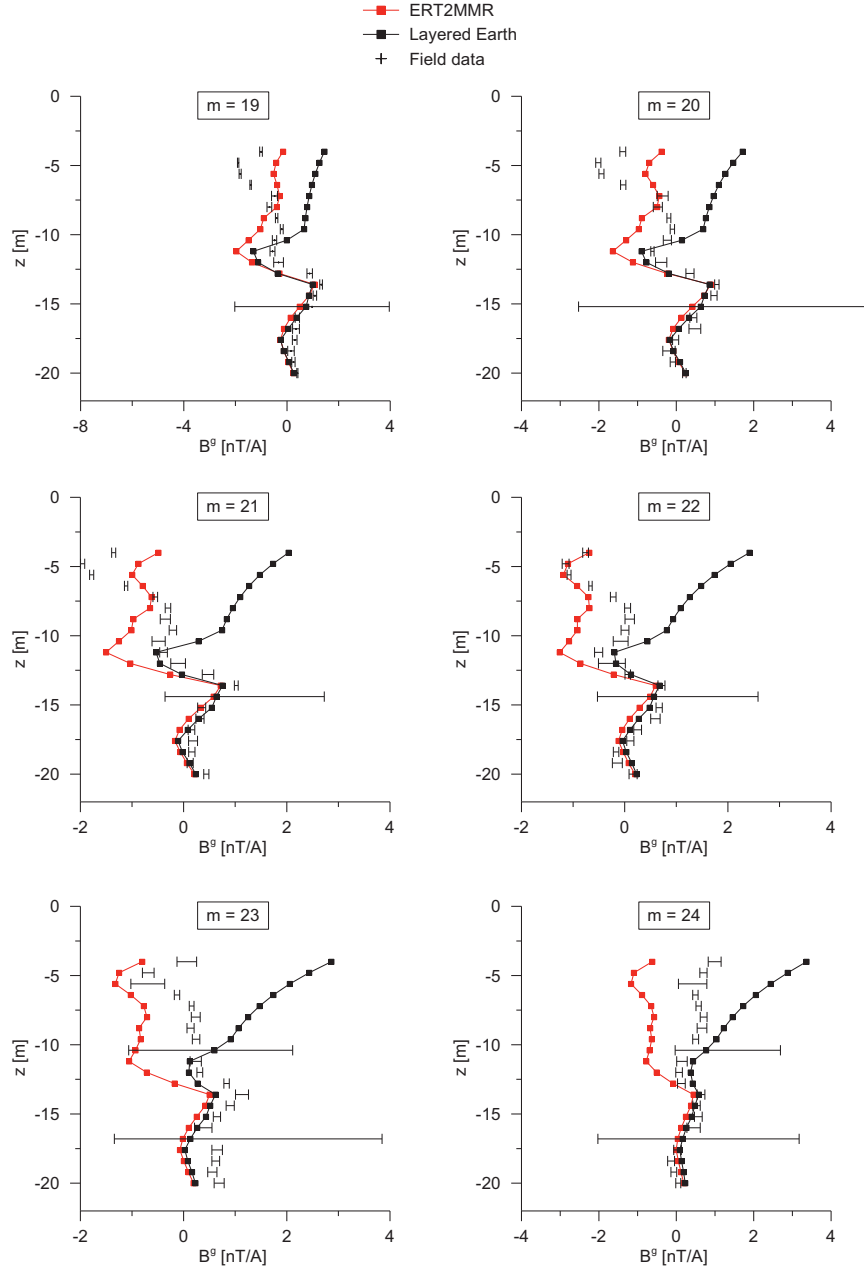


Figure C.9. Variation of MMR ground response B^g with depth for moving-source setup. Field data are compared to predicted responses, based on *ERT2MMR* and *Layered Earth* models, with respect to fixed magnetic field sensor positions $m = 19 - 24$.

Appendix D

Time-lapse responses

In order to give a complete overview, all field data acquired during time-lapse measurements are displayed in this chapter. Generally, data are collected according to the fast survey ($t_1 - t_5$) or total survey ($t_6 - t_7$). Difference in acquisition is illustrated in Fig. D.1.

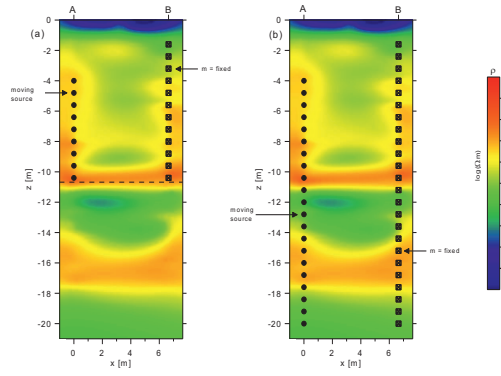


Figure D.1. Transmitter-receiver combinations considered for (a) fast and (b) total survey.

First, results in terms of anomalous MMR response B_s^g (7.1) are displayed for the first five time steps $t_1 - t_5$ with respect to the magnetic sensor positions ($m = 24 - 13$).

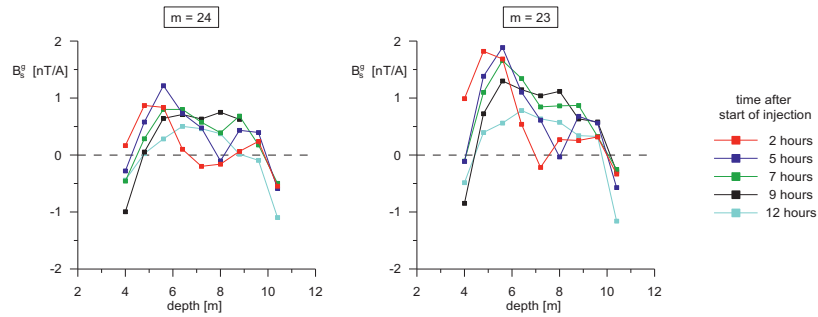


Figure D.2. Variation of the anomalous MMR ground response B_s^g with depth for the first five time-steps $t_1 - t_5$ and sensor positions $m = 24 - 13$.

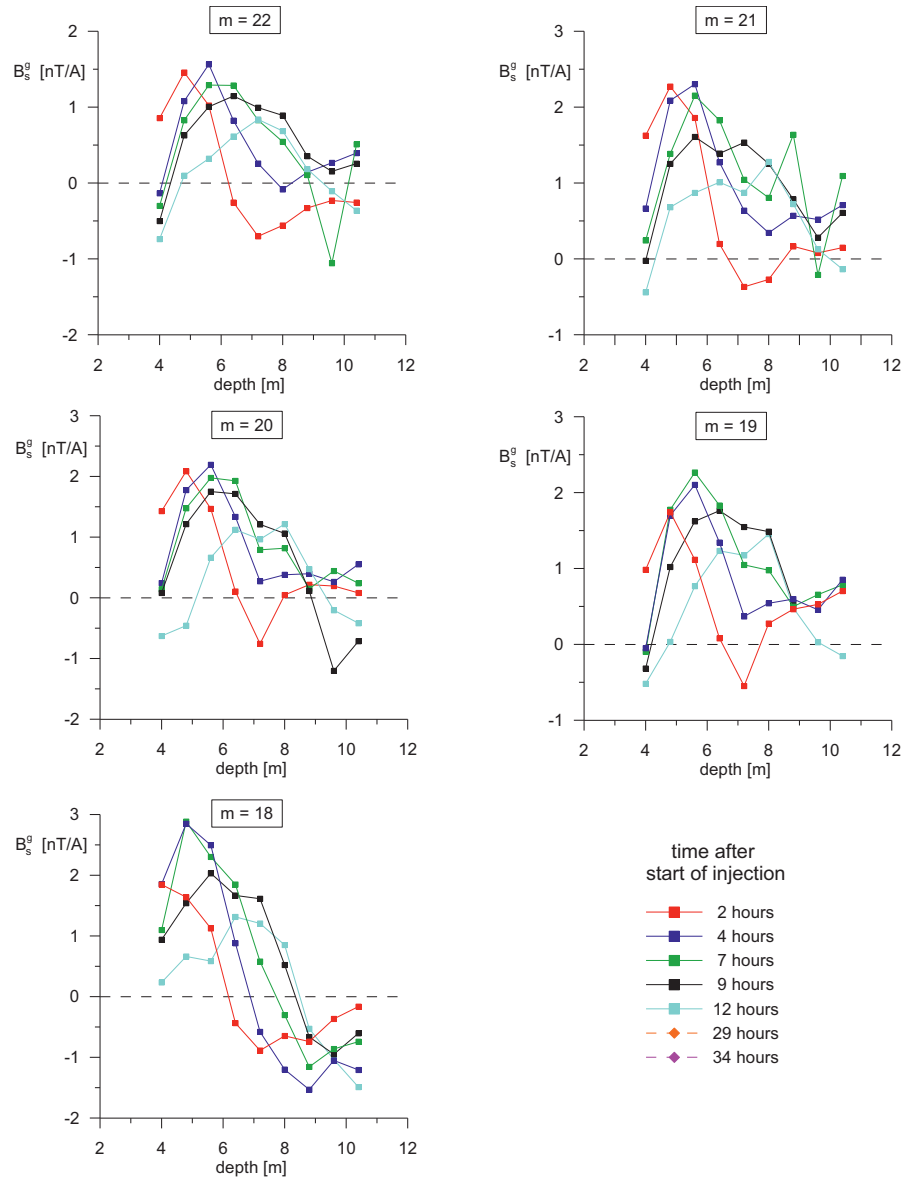


Figure D.3. Variation of the anomalous MMR ground response B_s^g with depth for the first five time-steps $t_1 - t_5$ and sensor positions $m = 22-18$.

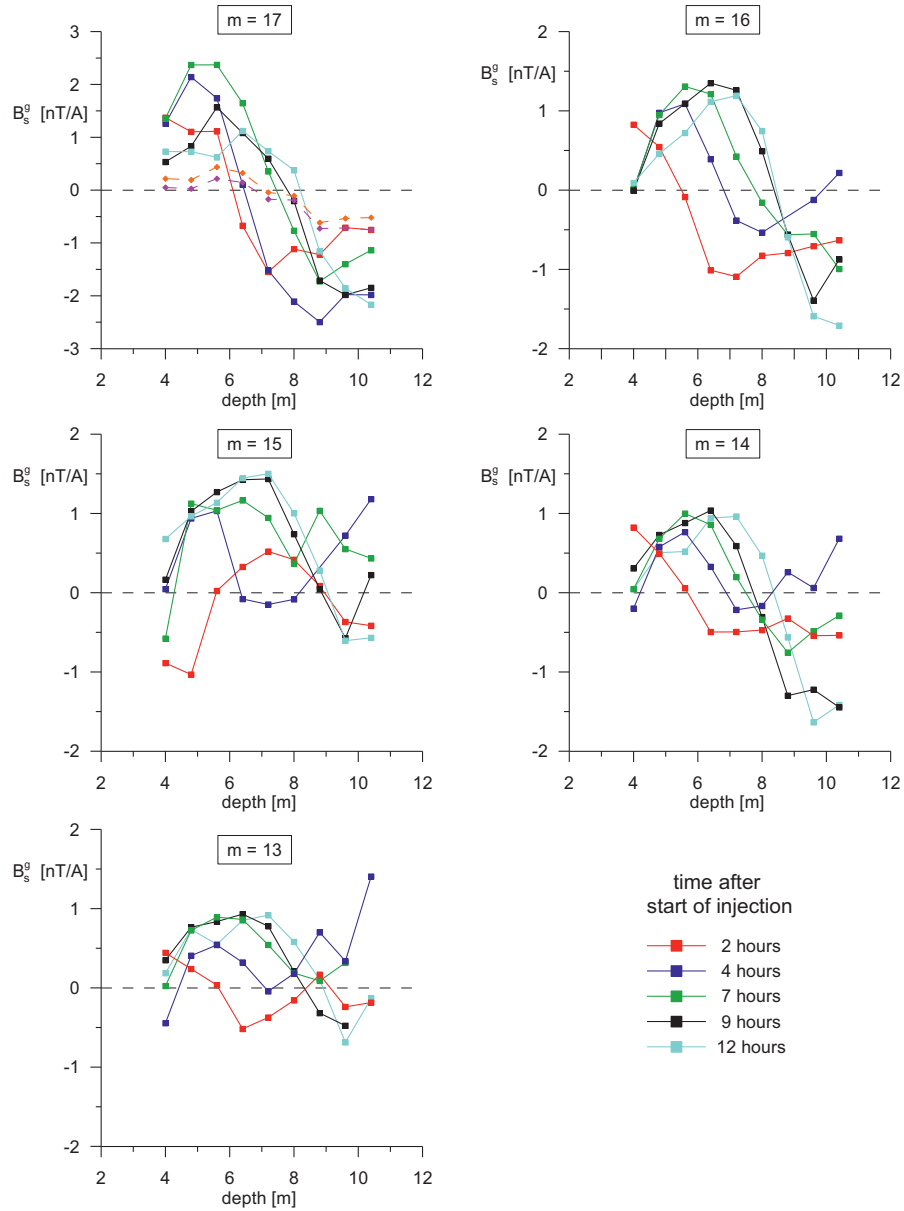


Figure D.4. Variation of the anomalous MMR ground response B_s^g with depth for the first five time-steps $t_1 - t_5$ and sensor positions $m = 17-13$.

Secondly, results in terms of anomalous MMR response B_s^g (7.1) are displayed for the two time steps $t_6 - t_7$ (collected during Day 2) with respect to the sensor positions ($m = 22 - 3$).

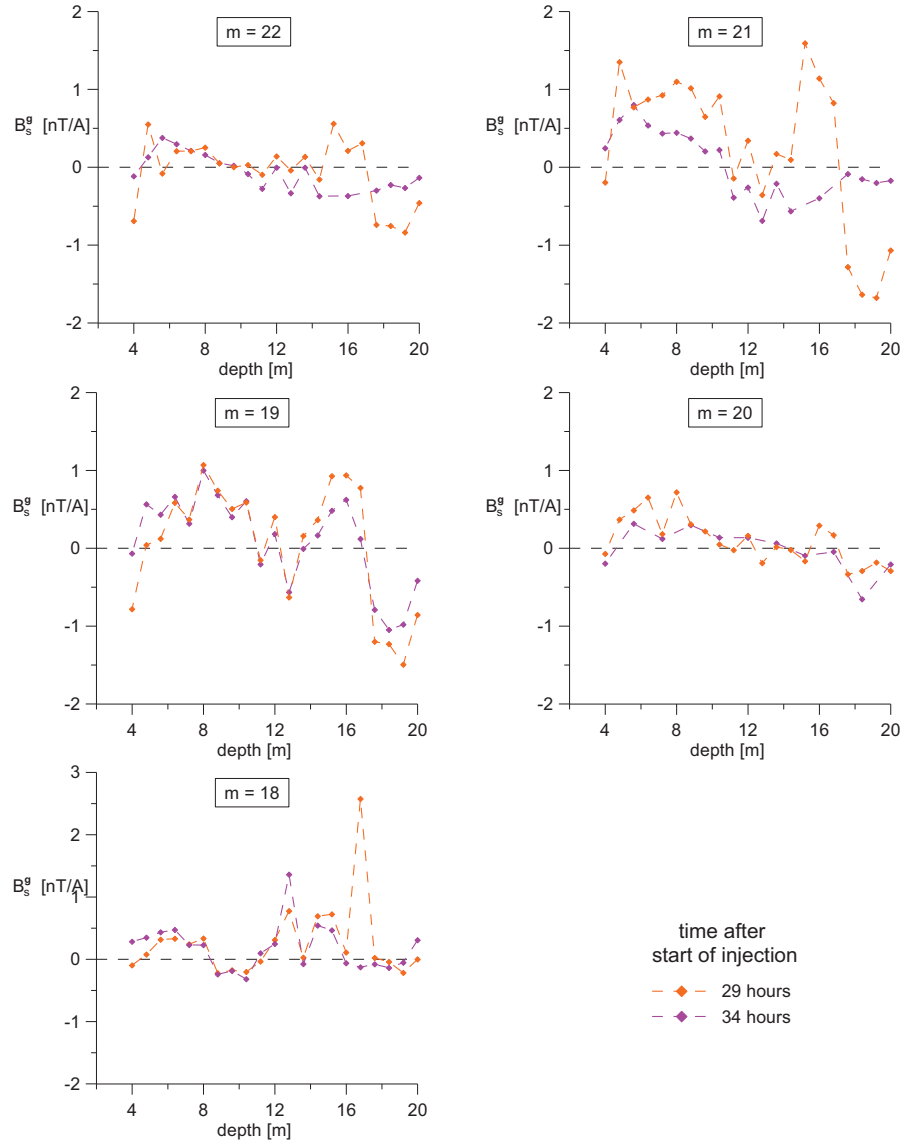


Figure D.5. Variation of the anomalous MMR ground response B_s^g with depth for the later two time-steps $t_6 - t_7$ and sensor positions $m = 22-18$.

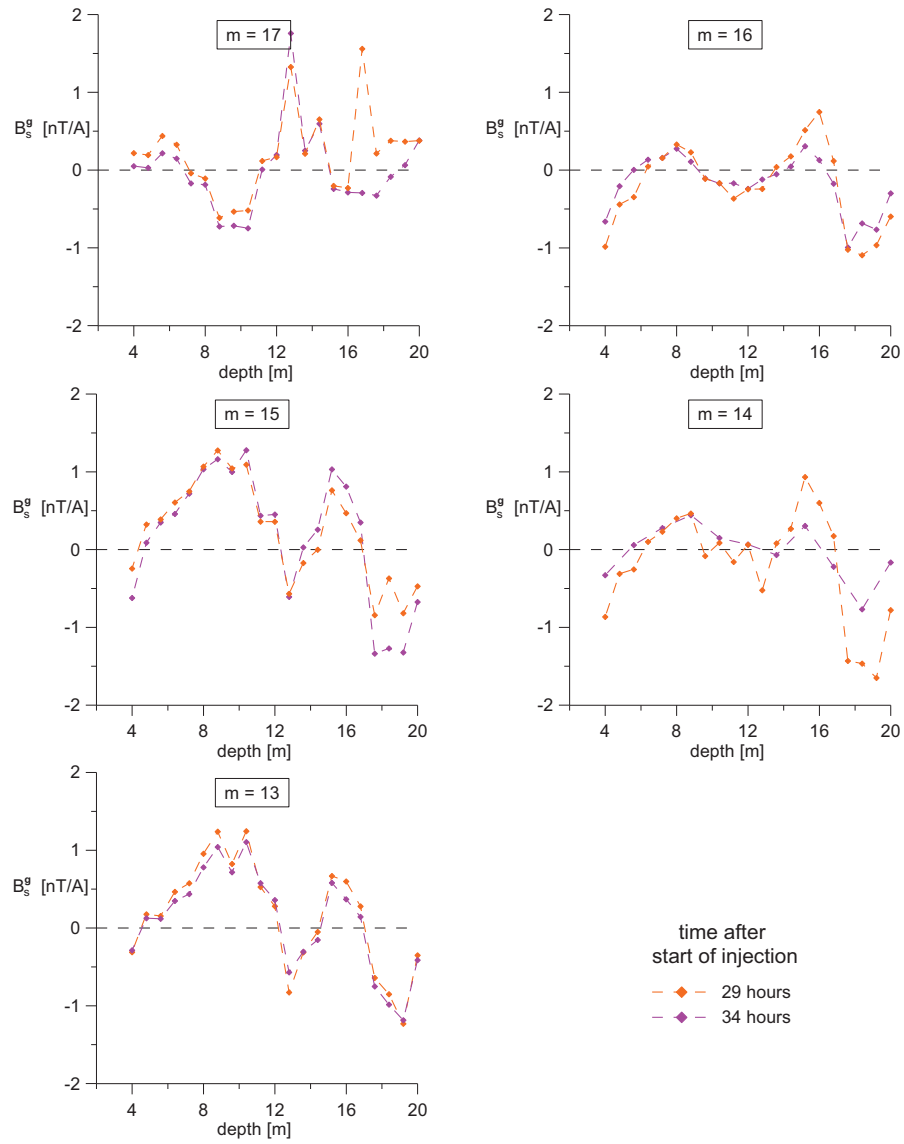


Figure D.6. Variation of the anomalous MMR ground response B_s^g with depth for the later two time-steps $t_6 - t_7$ and sensor positions $m = 17-13$.

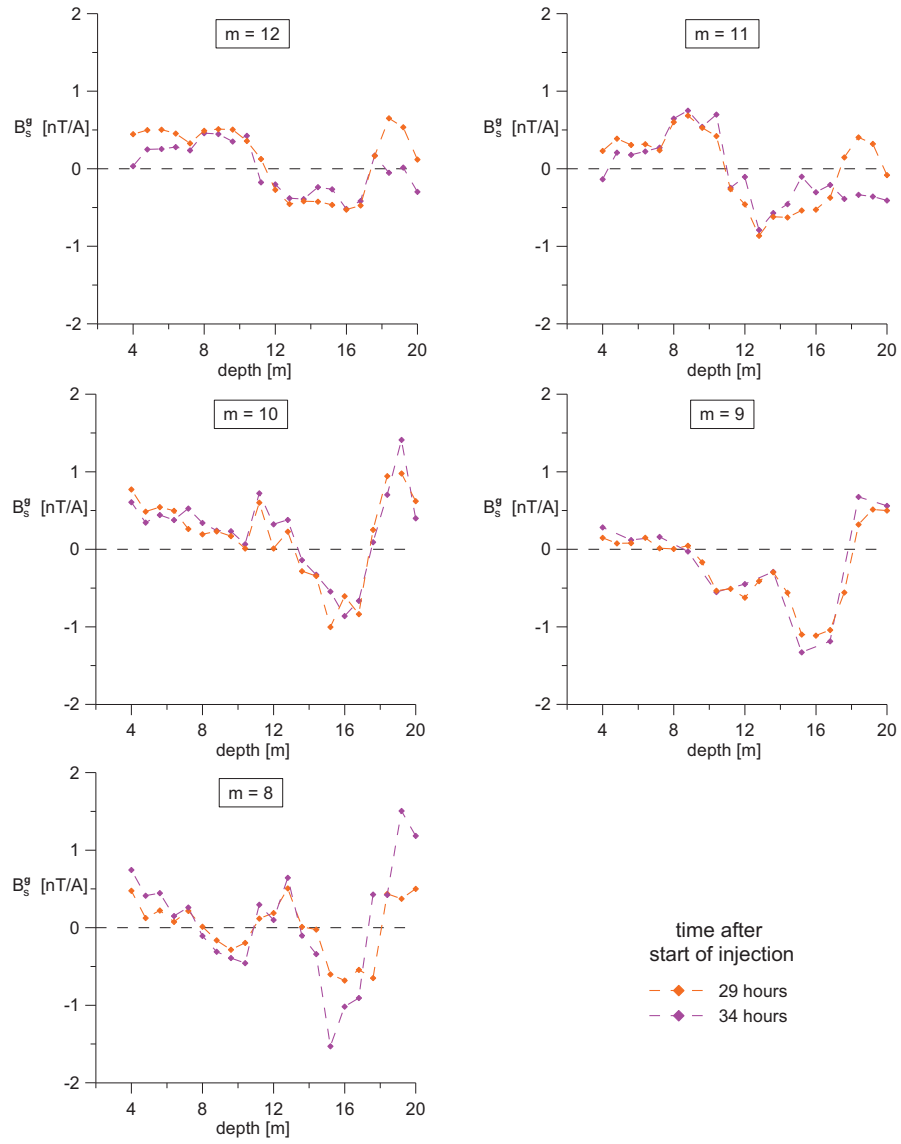


Figure D.7. Variation of the anomalous MMR ground response B_s^g with depth for the later two time-steps $t_6 - t_7$ and sensor positions $m = 12-8$.

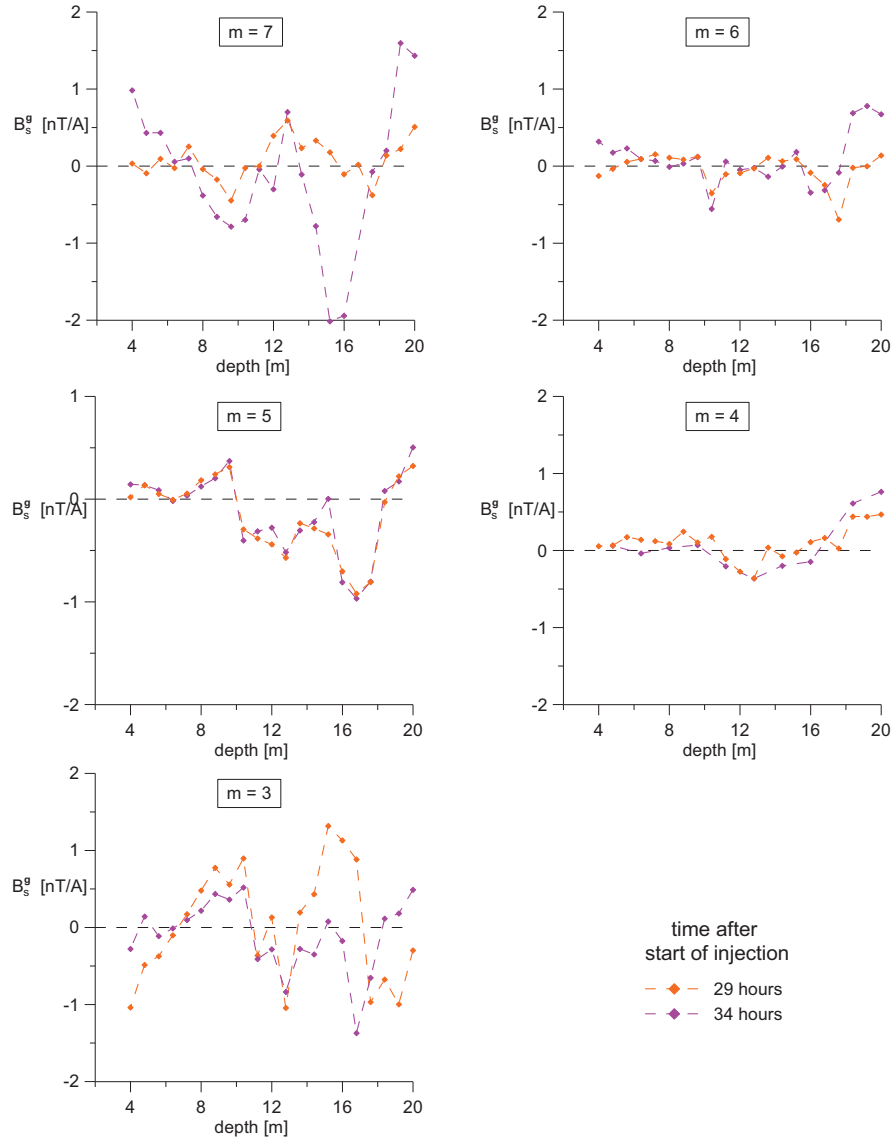


Figure D.8. Variation of the anomalous MMR ground response B_s^g with depth for the later two time-steps $t_6 - t_7$ and sensor positions $m = 7-3$.

References

- Acosta, J. E. and M. H. Worthington. 1983, A borehole magnetometric resistivity experiment: Geophysical Prospecting, **31**, 800-809.
- Archie, G. E., 1942, The electrical resistivity log as an aid in determining some reservoir characteristics: Transaction of the American Institute of Mining, Metallurgical and Petroleum Engineers (AIME), Littleton, **146**, 54-62.
- Asten, M. W., 1988, The downhole magnetometric resistivity (DHMMR) method: Exploration Geophysics, **19**, 12-16.
- Bishop, J., Lewis, R. and N. Stolz, 2000, Horseshoe for (conductive) courses: DHEM and DHMMR: Exploration Geophysics, **31**, 192-199.
- Boggs, D. B., Stanley, J. M. and M. K. Cattach, 1998, Feasibility studies of TFMMIP and TFEM surveying with Sub-Audio Magnetics: Exploration Geophysics, **29**, 290-295.
- Boggs, D. B., Stanley, J. M. and M. K. Cattach, 1999, Three-dimensional numerical modelling of sub-audio magnetic data: Exploration Geophysics, **30**, 147-156.
- Cattach, M. K., Stanley, J. M., Lee, S. J. and G. W. Boyd, 1993, Sub-Audio Magnetics (SAM) - A high resolution technique for simultaneously mapping electrical and magnetic properties: Exploration Geophysics, **24**, 387-400.
- Chen, J. and D. W. Oldenburg, 2004, Magnetic and electric fields of direct currents in a layered Earth (Short Note): Exploration Geophysics, **35**, 157-163.
- Chen, J. and D. W. Oldenburg, 2006, 3-D inversion of magnetic induced polarization data: Exploration Geophysics, **37**, 245 - 253 .
- Chen, J., Oldenburg, D. W. and E. Haber, 2002a, 3-D inversion of magnetometric resistivity data: Proceedings of the 72nd SEG annual meeting, Salt Lake City, Expanded Abstracts, 633-636.

- Chen, J., Oldenburg, D. W. and E. Haber, 2002b, Three-dimensional numerical modeling and inversion of magnetometric resistivity data: *Geophys. J. Int.*, **149**, 679-697.
- Cheesman, S. J. and R. N. Edwards, 1989, Current channelling in square plates with applications to magnetometric resistivity: *Geophysical Prospecting*, **37**, 553-581.
- Deiana, R., Cassiani, G., Kemna, A., Villa, A., Bruno, V. and A. Bagliani, 2007, An experiment of non-invasive characterisation of the vadose zone via water injection and cross-hole time-lapse geophysical monitoring: *Near Surface Geophysics*, **5**, 183-194.
- Edwards, R. N., 1973, The magnetometric resistivity method and its application to the mapping of a fault: *Can. J. Earth Sci.*, **11**, 1136-1156.
- Edwards, R. N., 1984, The cross-hole magnetometric resistivity (MMR) response of a disc conductor: *Geophysical Prospecting*, **32**, 955-969.
- Edwards, R. N. and E. C. Howell, 1976, A field test of the magnetometric resistivity (MMR) method: *Geophysics*, **41**, 1170-1183.
- Edwards, R. N. and M. N. Nabighian, 1991, The magnetometric resistivity method, *in* Nabighian, M. N., ed., *Electromagnetic Methods in Applied Geophysics*, 2, Application: Soc. Expl. Geophys., 47-104.
- Elders, J. A. and M. W. Asten, 2004, A comparison of receiver technologies in borehole MMR and EM surveys: *Geophysical Prospecting*, **52**, 85-96.
- Erdélyi, A., Oberhettinger, M. F. and F. G. Tricomi, 1954, *Tables of Integral Transforms*. Based, in Part, on Notes left by Harry Bateman and Compiled by the Staff of the Bateman Manuscript Project. McGraw-Hill.
- Fathianpour, N., 1997, Analytical and numerical modelling of total magnetometric resistivity (TFMMR) data: Ph.D. thesis, Flinders University of South Australia.
- Fathianpour, N., Heinson, G. and A. White, 2005a, The Total Field Magnetometric Resistivity (TFMMR) Method Part I: theory and 2.5D forward modelling: *Exploration Geophysics*, **36**, 181-188.
- Fathianpour, N., Heinson, G. and A. White, 2005b, The Total Field Magnetometric Resistivity (TFMMR) Method Part II: 2D resistivity inversion of data from the Flying Doctor Deposit, Broken Hill, Australia: *Exploration Geophysics*, **36**, 189-197.
- Gomez Trevino, E. and R. N. Edwards, 1979, Magnetometric resistivity (MMR) anomalies of two-dimensional structures: *Geophysics*, **44**, 947-958.

- Haber, E., 2000, A mixed finite element method for the solution of the magnetostatic problem with highly discontinuous coefficients in 3D: *Computational Geosciences*, **4**, 323-326.
- Hashemi, A., Meyers, J. and E. Rothery, 2005, Sub-Audio Magnetic surveying for shallow occurrences of conductive manganese ore, Woodie Woodie area, Western Australia: *Exploration Geophysics*, **36**, 170-175.
- Jakosky, J. J., 1933, Method and Apparatus for Determining Underground structure. U.S. Patent no. 1906271.
- Jin, J., 1993, *The Finite Element Method in Electromagnetics*: John Wiley & Sons, New York.
- Kaiguang, Z. and Y. Jianwen, 2008, Time-dependent magnetometric resistivity anomalies of groundwater contamination: Synthetic results from computational hydro-geophysical modeling: *Applied Geophysics*, **5**, No. 4, 322-330.
- Kemna, A., 2000, Tomographic inversion of complex resistivity – theory and application: Ph.D. thesis, Ruhr-Universität Bochum.
- Kemna, A., Vanderborght, J., Kulesa, B. and H. Vereecken, 2002, Imaging and characterisation of subsurface solute transport using electrical resistivity tomography (ERT) and equivalent transport models: *Journal of Hydrology*, **267**, 125-146.
- Kemna, A., Tillmann, A., Verweerd, A., Zimmermann, E., and H. Vereecken, 2003, MERIT – a new magneto-electrical resistivity imaging technique: 1) modeling and tomographic reconstruction: in *Proc. 3rd World Congr. Industrial Tomography*, 256-261.
- Kemna, A., Fielitz, D., Cassiani, G., and E. Zimmermann, 2008, 2.5D MMR modeling on compact grids, 68th Annual Meeting of the German Geophysical Society, Freiberg, (in German).
- Koestel, J., Kemna, A., Javaux, M., Binley, A. and H. Vereecken, 2008, Quantitative image of solute transport in an unsaturated and undisturbed soil monolith with 3D ERT and TDR: *Water Resources Research*, **44**, W12411.
- Kulesa, B., Jaekel, U., Kemna, A., and H. Vereecken, 2002, Magnetometric resistivity (MMR) imaging of subsurface solute flow: Inversion framework and laboratory tests: *Journal of Environmental Engineering Geophysics (JEEG)*, **7**, 111-118.

- LaBrecque, D., Sharpe, R., Cascale, D., Heath, G. L. and J. M. Svoboda, 2003, Combined electrical and magnetic resistivity tomography: synthetic model study and inverse modeling: *Journal of Environmental and Engineering Geophysics (JEEG)*, **8**, Issue 4, 251-262.
- Li, Y., and D. W. Oldenburg, 1991, Aspects of charge accumulation in DC resistivity experiments: *Geophysical Prospecting*, **39**, 803-826.
- Looms, M., 2007, Hydrogeophysics - Hydrological characterisation using cross-borehole ground penetrating radar and electrical resistivity tomography: Ph.D. thesis, University of Copenhagen, Denmark.
- Ludwig, M. A., Alumbaugh, D., LaBrecque, D., Sharpe, R. and G. L. Heath, 2004, Synthetic studies to determine the effects of anomalous magnetic permeability on a new electrical resistivity tomography/magnetometric resistivity survey system: *Proceedings of SAGEEP 2004*, Colorado Springs, 673-686.
- Nabighian, M. N., and G. L. Oppliger, 1980, Recent advances in the magnetometric resistivity methods: Presented at the 42nd meeting of the European Assoc. of Expl. Geophys., Istanbul.
- Nabighian, M. N., Oppliger, G. L., Edwards, R. N., Lo, B. B. H. and S. J. Cheesman, 1984, Cross-hole magnetometric resistivity (MMR): *Geophysics*, **49**, 1313-1326.
- Pai, D. M. and R. N. Edwards, 1983, Programme MMR2DFD: finite difference modelling of MMR anomalies: *Res. in Applied Geophysics*, No. 25, University of Toronto.
- Pai, D. M. and J. P. Yeoh, 1987, Downhole magnetometric resistivity response of a half-plane conductor: *Geophysics*, **52**, No. 3, 353-362.
- Purss, M. B. J. and J. P. Cull, 2003, B-field probes for downhole magnetometric resistivity surveys: *Exploration Geophysics*, **34**, 233-240.
- Purss, M. B. J., Cull, J. P. and M. W. Asten, 2003, Simultaneous modelling of the phase and amplitude components of downhole magnetometric resistivity data: *Journal of Applied Geophysics*, **54**, 1-14.
- Seigel, H. O., 1974, The magnetometric induced polarization (MIP) method: *Geophysics*, **39**, 321-339.
- Svoboda, J. M., Canan, B., Morrison, J. L., Heath, G. L. and D. LaBrecque, 2002, Advanced technology for mapping subsurface water conductivity. *Proceedings of SAGEEP 2002*, Las Vegas, EEGS.

- Telford, W. M., Geldart, L.P., and R. E. Sheriff, 1990, Applied Geophysics, 2nd Edition: Cambridge University Press, Cambridge.
- Tronicke, J., Blindow, N., Gross, R. and M. A. Lange, 1999, Joint application of surface electrical resistivity- and GPR-measurements for groundwater exploration on the island of Spiekeroog - northern Germany: Journal of Hydrology, **223**, 44-53.
- Veitch, D., Asten, M. W. and E. H. Leeuwen. 1990, Electrical and magnetometric fields in a layered earth containing buried electrodes: Geophysics, **55**, No. 12, 1605-1612.
- Vereecken, H., Hubbard, S., Binley, A. and T. Ferré, 2004, Hydrogeophysics: An Introduction from the Guest Editors: Vadoze Zone Journal, **3**, SSSA, 1060-1062.
- Verweerd, A., 2007, Performance analysis and characterisation of a new magneto-electrical measurement system for electrical conductivity imaging: Ph.D. thesis, University of Bonn, published by Forschungszentrum Juelich.
- Whitford, M., Meyers, J. and N. Stolz, 2005, The SAM EQMMR response of the regolith at East Victory, St Ives Gold Mine, Western Australia: Exploration Geophysics, **36**, 133-139.
- Xiong, Z. and A. Tripp, 1995, A block iterative algorithm for 3-D electromagnetic modelling using integral equations with symmetrized substructures: Geophysics, **60**, 291-295.
- Yaramanci, U., Kemna, A. And H. Vereecken, 2005, Emerging Technologies in hydrogeophysics: *in* Hydrogeophysics by Rubin, Y. And S. Hubbard, Ed., Springer-Verlag, Berlin Heidelberg.
- Zimmermann, E., Verweerd, A., Glaas, W., Tillmann, A. and A. Kemna, 2005, An AMR sensor-based measurements system for magnetoelectrical resistivity tomography: IEEE-Sensors-Journal, **5**, 233-241.
- Zimmermann, E., Kemna, A., Berwix, J. and W. Glaas, 2007, EIT measurement system with high phase accuracy for the imaging of spectral induced polarization properties of soils and sediments: Measurement Science and Technology, **19**, 094010.
- Zimmermann, E., Fielitz, D., Glaas, W. and A. Kemna, 2008, Neues Messsystem für MMR-Messungen im Bohrloch, 68th Annual Meeting of the German Geophysical Society, Freiberg, (in German).

Ich versichere, dass ich die von mir vorgelegte Dissertation selbständig angefertigt, die benutzten Quellen und Hilfsmittel vollständig angegeben und die Stellen der Arbeit – einschließlich Tabellen, Karten und Abbildungen –, die anderen Werken im Wortlaut oder dem Sinn nach entnommen sind, in jedem Einzelfall als Entlehnung kenntlich gemacht habe; dass diese Dissertation noch keiner anderen Fakultät oder Universität zur Prüfung vorgelegen hat; dass sie – abgesehen von unten angegebenen Teilpublikationen – noch nicht veröffentlicht worden ist sowie, dass ich eine solche Veröffentlichung vor Abschluss des Promotionsverfahrens nicht vornehmen werde. Die Bestimmungen der Promotionsordnung sind mir bekannt. Die von mir vorgelegte Dissertation ist von Prof. Bülent Tezkan betreut worden.

Köln, 16.12.2009

1. **Einsatz von multispektralen Satellitenbilddaten in der Wasserhaushalts- und Stoffstrommodellierung – dargestellt am Beispiel des Rureinzugsgebietes**
von C. Montzka (2008), XX, 238 Seiten
ISBN: 978-3-89336-508-1
2. **Ozone Production in the Atmosphere Simulation Chamber SAPHIR**
by C. A. Richter (2008), XIV, 147 pages
ISBN: 978-3-89336-513-5
3. **Entwicklung neuer Schutz- und Kontaktierungsschichten für Hochtemperatur-Brennstoffzellen**
von T. Kiefer (2008), 138 Seiten
ISBN: 978-3-89336-514-2
4. **Optimierung der Reflektivität keramischer Wärmedämmschichten aus Yttrium-teilstabilisiertem Zirkoniumdioxid für den Einsatz auf metallischen Komponenten in Gasturbinen**
von A. Stuke (2008), X, 201 Seiten
ISBN: 978-3-89336-515-9
5. **Lichtstreuende Oberflächen, Schichten und Schichtsysteme zur Verbesserung der Lichteinkopplung in Silizium-Dünnschichtsolarzellen**
von M. Berginski (2008), XV, 171 Seiten
ISBN: 978-3-89336-516-6
6. **Politiksznarien für den Klimaschutz IV – Szenarien bis 2030**
hrsg.von P. Markewitz, F. Chr. Matthes (2008), 376 Seiten
ISBN 978-3-89336-518-0
7. **Untersuchungen zum Verschmutzungsverhalten rheinischer Braunkohlen in Kohledampferzeugern**
von A. Schlüter (2008), 164 Seiten
ISBN 978-3-89336-524-1
8. **Inorganic Microporous Membranes for Gas Separation in Fossil Fuel Power Plants**
by G. van der Donk (2008), VI, 120 pages
ISBN: 978-3-89336-525-8
9. **Sinterung von Zirkoniumdioxid-Elektrolyten im Mehrlagenverbund der oxidkeramischen Brennstoffzelle (SOFC)**
von R. Mücke (2008), VI, 165 Seiten
ISBN: 978-3-89336-529-6
10. **Safety Considerations on Liquid Hydrogen**
by K. Verfondern (2008), VIII, 167 pages
ISBN: 978-3-89336-530-2

11. **Kerosinreformierung für Luftfahrtanwendungen**
von R. C. Samsun (2008), VII, 218 Seiten
ISBN: 978-3-89336-531-9
12. **Der 4. Deutsche Wasserstoff Congress 2008 – Tagungsband**
hrsg. von D. Stolten, B. Emonts, Th. Grube (2008), 269 Seiten
ISBN: 978-3-89336-533-3
13. **Organic matter in Late Devonian sediments as an indicator for environmental changes**
by M. Klopisch (2008), XII, 188 pages
ISBN: 978-3-89336-534-0
14. **Entschwefelung von Mitteldestillaten für die Anwendung in mobilen Brennstoffzellen-Systemen**
von J. Latz (2008), XII, 215 Seiten
ISBN: 978-3-89336-535-7
15. **RED-IMPACT**
Impact of Partitioning, Transmutation and Waste Reduction Technologies on the Final Nuclear Waste Disposal
SYNTHESIS REPORT
ed. by W. von Lensa, R. Nabbi, M. Rossbach (2008), 178 pages
ISBN 978-3-89336-538-8
16. **Ferritic Steel Interconnectors and their Interactions with Ni Base Anodes in Solid Oxide Fuel Cells (SOFC)**
by J. H. Froitzheim (2008), 169 pages
ISBN: 978-3-89336-540-1
17. **Integrated Modelling of Nutrients in Selected River Basins of Turkey**
Results of a bilateral German-Turkish Research Project
project coord. M. Karpuzcu, F. Wendland (2008), XVI, 183 pages
ISBN: 978-3-89336-541-8
18. **Isotopengeochemische Studien zur klimatischen Ausprägung der Jünger Dryas in terrestrischen Archiven Eurasiens**
von J. Parplies (2008), XI, 155 Seiten, Anh.
ISBN: 978-3-89336-542-5
19. **Untersuchungen zur Klimavariabilität auf dem Tibetischen Plateau - Ein Beitrag auf der Basis stabiler Kohlenstoff- und Sauerstoffisotope in Jahrringen von Bäumen waldgrenznaher Standorte**
von J. Griessinger (2008), XIII, 172 Seiten
ISBN: 978-3-89336-544-9

20. **Neutron-Irradiation + Helium Hardening & Embrittlement Modeling of 9%Cr-Steels in an Engineering Perspective (HELENA)**
by R. Chaouadi (2008), VIII, 139 pages
ISBN: 978-3-89336-545-6
21. **in Bearbeitung**
22. **Verbundvorhaben APAWAGS (AOEV und Wassergenerierung) – Teilprojekt: Brennstoffreformierung – Schlussbericht**
von R. Peters, R. C. Samsun, J. Pasel, Z. Porš, D. Stolten (2008), VI, 106 Seiten
ISBN: 978-3-89336-547-0
23. **FREEVAL**
Evaluation of a Fire Radiative Power Product derived from Meteosat 8/9 and Identification of Operational User Needs
Final Report
project coord. M. Schultz, M. Wooster (2008), 139 pages
ISBN: 978-3-89336-549-4
24. **Untersuchungen zum Alkaliverhalten unter Oxycoal-Bedingungen**
von C. Weber (2008), VII, 143, XII Seiten
ISBN: 978-3-89336-551-7
25. **Grundlegende Untersuchungen zur Freisetzung von Spurstoffen, Heißgaschemie, Korrosionsbeständigkeit keramischer Werkstoffe und Alkalirückhaltung in der Druckkohlenstaubeuerung**
von M. Müller (2008), 207 Seiten
ISBN: 978-3-89336-552-4
26. **Analytik von ozoninduzierten phenolischen Sekundärmetaboliten in *Nicotiana tabacum* L. cv Bel W3 mittels LC-MS**
von I. Koch (2008), III, V, 153 Seiten
ISBN 978-3-89336-553-1
27. **IEF-3 Report 2009. Grundlagenforschung für die Anwendung**
(2009), ca. 230 Seiten
ISBN: 978-3-89336-554-8
28. **Influence of Composition and Processing in the Oxidation Behavior of MCrAlY-Coatings for TBC Applications**
by J. Toscano (2009), 168 pages
ISBN: 978-3-89336-556-2
29. **Modellgestützte Analyse signifikanter Phosphorbelastungen in hessischen Oberflächengewässern aus diffusen und punktuellen Quellen**
von B. Tetzlaff (2009), 149 Seiten
ISBN: 978-3-89336-557-9

30. **Nickelreaktivlot / Oxidkeramik – Fügungen als elektrisch isolierende Dichtungskonzepte für Hochtemperatur-Brennstoffzellen-Stacks**
von S. Zügner (2009), 136 Seiten
ISBN: 978-3-89336-558-6
31. **Langzeitbeobachtung der Dosisbelastung der Bevölkerung in radioaktiv kontaminierten Gebieten Weißrusslands – Korma-Studie**
von H. Dederichs, J. Pillath, B. Heuel-Fabianek, P. Hill, R. Lennartz (2009),
Getr. Pag.
ISBN: 978-3-89336-532-3
32. **Herstellung von Hochtemperatur-Brennstoffzellen über physikalische Gasphasenabscheidung**
von N. Jordán Escalona (2009), 148 Seiten
ISBN: 978-3-89336-532-3
33. **Real-time Digital Control of Plasma Position and Shape on the TEXTOR Tokamak**
by M. Mitri (2009), IV, 128 pages
ISBN: 978-3-89336-567-8
34. **Freisetzung und Einbindung von Alkalimetallverbindungen in kohlebefeuerten Kombikraftwerken**
von M. Müller (2009), 155 Seiten
ISBN: 978-3-89336-568-5
35. **Kosten von Brennstoffzellensystemen auf Massenbasis in Abhängigkeit von der Absatzmenge**
von J. Werhahn (2009), 242 Seiten
ISBN: 978-3-89336-569-2
36. **Einfluss von Reoxidationszyklen auf die Betriebsfestigkeit von anodengestützten Festoxid-Brennstoffzellen**
von M. Ettler (2009), 138 Seiten
ISBN: 978-3-89336-570-8
37. **Großflächige Plasmaabscheidung von mikrokristallinem Silizium für mikromorphe Dünnschichtsolarmodule**
von T. Kilper (2009), XVII, 154 Seiten
ISBN: 978-3-89336-572-2
38. **Generalized detailed balance theory of solar cells**
by T. Kirchartz (2009), IV, 198 pages
ISBN: 978-3-89336-573-9
39. **The Influence of the Dynamic Ergodic Divertor on the Radial Electric Field at the Tokamak TEXTOR**
von J. W. Coenen (2009), xii, 122, XXVI pages
ISBN: 978-3-89336-574-6

40. **Sicherheitstechnik im Wandel Nuklearer Systeme**
von K. Nünighoff (2009), viii, 215 Seiten
ISBN: 978-3-89336-578-4
41. **Pulvermetallurgie hochporöser NiTi-Legierungen für Implantat- und Dämpfungsanwendungen**
von M. Köhl (2009), XVII, 199 Seiten
ISBN: 978-3-89336-580-7
42. **Einfluss der Bondcoatzusammensetzung und Herstellungsparameter auf die Lebensdauer von Wärmedämmschichten bei zyklischer Temperaturbelastung**
von M. Subanovic (2009), 188, VI Seiten
ISBN: 978-3-89336-582-1
43. **Oxygen Permeation and Thermo-Chemical Stability of Oxygen Permeation Membrane Materials for the Oxyfuel Process**
by A. J. Ellett (2009), 176 pages
ISBN: 978-3-89336-581-4
44. **Korrosion von polykristallinem Aluminiumoxid (PCA) durch Metalljodidschmelzen sowie deren Benetzungseigenschaften**
von S. C. Fischer (2009), 148 Seiten
ISBN: 978-3-89336-584-5
45. **IEF-3 Report 2009. Basic Research for Applications**
(2009), 217 Seiten
ISBN: 978-3-89336-585-2
46. **Verbundvorhaben ELBASYS (Elektrische Basissysteme in einem CFK-Rumpf) - Teilprojekt: Brennstoffzellenabgase zur Tankinertisierung - Schlussbericht**
von R. Peters, J. Latz, J. Pasel, R. C. Samsun, D. Stolten
(2009), xi, 202 Seiten
ISBN: 978-3-89336-587-6
47. **Aging of ¹⁴C-labeled Atrazine Residues in Soil: Location, Characterization and Biological Accessibility**
by N. D. Jablonowski (2009), IX, 104 pages
ISBN: 978-3-89336-588-3
48. **Entwicklung eines energetischen Sanierungsmodells für den europäischen Wohngebäudesektor unter dem Aspekt der Erstellung von Szenarien für Energie- und CO₂ - Einsparpotenziale bis 2030**
von P. Hansen (2009), XXII, 281 Seiten
ISBN: 978-3-89336-590-6

49. **Reduktion der Chromfreisetzung aus metallischen Interkonnektoren für Hochtemperaturbrennstoffzellen durch Schutzschichtsysteme**
von R. Trebbels (2009), iii, 135 Seiten
ISBN: 978-3-89336-591-3
50. **Bruchmechanische Untersuchung von Metall / Keramik-Verbundsystemen für die Anwendung in der Hochtemperaturbrennstoffzelle**
von B. Kuhn (2009), 118 Seiten
ISBN: 978-3-89336-592-0
51. **Wasserstoff-Emissionen und ihre Auswirkungen auf den arktischen Ozonverlust**
Risikoanalyse einer globalen Wasserstoffwirtschaft
von T. Feck (2009), 180 Seiten
ISBN: 978-3-89336-593-7
52. **Development of a new Online Method for Compound Specific Measurements of Organic Aerosols**
by T. Hohaus (2009), 156 pages
ISBN: 978-3-89336-596-8
53. **Entwicklung einer FPGA basierten Ansteuerungselektronik für Justageeinheiten im Michelson Interferometer**
von H. Nöldgen (2009), 121 Seiten
ISBN: 978-3-89336-599-9
54. **Observation – and model – based study of the extratropical UT/LS**
by A. Kunz (2010), xii, 120, xii pages
ISBN: 978-3-89336-603-3
55. **Herstellung polykristalliner Szintillatoren für die Positronen-Emissions-Tomographie (PET)**
von S. K. Karim (2010), VIII, 154 Seiten
ISBN: 978-3-89336-610-1
56. **Kombination eines Gebäudekondensators mit H₂-Rekombinatorelementen in Leichtwasserreaktoren**
von S. Kelm (2010), vii, 119 Seiten
ISBN: 978-3-89336-611-8
57. **Plant Leaf Motion Estimation Using A 5D Affine Optical Flow Model**
by T. Schuchert (2010), X, 143 pages
ISBN: 978-3-89336-613-2
58. **Tracer-tracer relations as a tool for research on polar ozone loss**
by R. Müller (2010), 116 pages
ISBN: 978-3-89336-614-9

59. **Sorption of polycyclic aromatic hydrocarbon (PAH) to Yangtze River sediments and their components**
by J. Zhang (2010), X, 109 pages
ISBN: 978-3-89336-616-3
60. **Weltweite Innovationen bei der Entwicklung von CCS-Technologien und Möglichkeiten der Nutzung und des Recyclings von CO₂**
Studie im Auftrag des BMWi
von W. Kuckshinrichs et al. (2010), X, 139 Seiten
ISBN: 978-3-89336-617-0
61. **Herstellung und Charakterisierung von sauerstoffionenleitenden Dünnschichtmembranstrukturen**
von M. Betz (2010), XII, 112 Seiten
ISBN: 978-3-89336-618-7
62. **Politiksznarien für den Klimaschutz V – auf dem Weg zum Strukturwandel, Treibhausgas-Emissionsszenarien bis zum Jahr 2030**
hrsg. von P. Hansen, F. Chr. Matthes (2010), 276 Seiten
ISBN: 978-3-89336-619-4
63. **Charakterisierung Biogener Sekundärer Organischer Aerosole mit Statistischen Methoden**
von C. Spindler (2010), iv, 163 Seiten
ISBN: 978-3-89336-622-4
64. **Stabile Algorithmen für die Magnetotomographie an Brennstoffzellen**
von M. Wannert (2010), ix, 119 Seiten
ISBN: 978-3-89336-623-1
65. **Sauerstofftransport und Degradationsverhalten von Hochtemperaturmembranen für CO₂-freie Kraftwerke**
von D. Schlehüser (2010), VII, 139 Seiten
ISBN: 978-3-89336-630-9
66. **Entwicklung und Herstellung von foliengegossenen, anodengestützten Festoxidbrennstoffzellen**
von W. Schafbauer (2010), VI, 164 Seiten
ISBN: 978-3-89336-631-6
67. **Disposal strategy of proton irradiated mercury from high power spallation sources**
by S. Chiriki (2010), xiv, 124 pages
ISBN: 978-3-89336-632-3
68. **Oxides with polyatomic anions considered as new electrolyte materials for solid oxide fuel cells (SOFCs)**
by O. H. Bin Hassan (2010), vii, 121 pages
ISBN: 978-3-89336-633-0

69. **Von der Komponente zum Stack: Entwicklung und Auslegung von HT-PEFC-Stacks der 5 kW-Klasse**
von A. Bendzulla (2010), IX, 203 Seiten
ISBN: 978-3-89336-634-7
70. **Satellitengestützte Schwerewellenmessungen in der Atmosphäre und Perspektiven einer zukünftigen ESA Mission (PREMIER)**
von S. Höfer (2010), 81 Seiten
ISBN: 978-3-89336-637-8
71. **Untersuchungen der Verhältnisse stabiler Kohlenstoffisotope in atmosphärisch relevanten VOC in Simulations- und Feldexperimenten**
von H. Spahn (2010), IV, 210 Seiten
ISBN: 978-3-89336-638-5
72. **Entwicklung und Charakterisierung eines metallischen Substrats für nanostrukturierte keramische Gastrennmembranen**
von K. Brands (2010), vii, 137 Seiten
ISBN: 978-3-89336-640-8
73. **Hybridisierung und Regelung eines mobilen Direktmethanol-Brennstoffzellen-Systems**
von J. Chr. Wilhelm (2010), 220 Seiten
ISBN: 978-3-89336-642-2
74. **Charakterisierung perowskitischer Hochtemperaturmembranen zur Sauerstoffbereitstellung für fossil gefeuerte Kraftwerksprozesse**
von S.A. Möbius (2010) III, 208 Seiten
ISBN: 978-3-89336-643-9
75. **Characterization of natural porous media by NMR and MRI techniques: High and low magnetic field studies for estimation of hydraulic properties**
by L.-R. Stingaciu (2010), 96 pages
ISBN: 978-3-89336-645-3
76. **Hydrological Characterization of a Forest Soil Using Electrical Resistivity Tomography**
by Chr. Oberdörster (2010), XXI, 151 pages
ISBN: 978-3-89336-647-7
77. **Ableitung von atomarem Sauerstoff und Wasserstoff aus Satellitendaten und deren Abhängigkeit vom solaren Zyklus**
von C. Lehmann (2010), 127 Seiten
ISBN: 978-3-89336-649-1

78. **18th World Hydrogen Energy Conference 2010 – WHEC2010**
Proceedings
Speeches and Plenary Talks
ed. by D. Stolten, B. Emonts (2010)
ISBN: 978-3-89336-658-3
- 78-1. **18th World Hydrogen Energy Conference 2010 – WHEC2010**
Proceedings
Parallel Sessions Book 1:
Fuel Cell Basics / Fuel Infrastructures
ed. by D. Stolten, T. Grube (2010), ca. 460 pages
ISBN: 978-3-89336-651-4
- 78-2. **18th World Hydrogen Energy Conference 2010 – WHEC2010**
Proceedings
Parallel Sessions Book 2:
Hydrogen Production Technologies – Part 1
ed. by D. Stolten, T. Grube (2010), ca. 400 pages
ISBN: 978-3-89336-652-1
- 78-3. **18th World Hydrogen Energy Conference 2010 – WHEC2010**
Proceedings
Parallel Sessions Book 3:
Hydrogen Production Technologies – Part 2
ed. by D. Stolten, T. Grube (2010), ca. 640 pages
ISBN: 978-3-89336-653-8
- 78-4. **18th World Hydrogen Energy Conference 2010 – WHEC2010**
Proceedings
Parallel Sessions Book 4:
Storage Systems / Policy Perspectives, Initiatives and Cooperations
ed. by D. Stolten, T. Grube (2010), ca. 500 pages
ISBN: 978-3-89336-654-5
- 78-5. **18th World Hydrogen Energy Conference 2010 – WHEC2010**
Proceedings
Parallel Sessions Book 5:
Strategic Analysis / Safety Issues / Existing and Emerging Markets
ed. by D. Stolten, T. Grube (2010), ca. 530 pages
ISBN: 978-3-89336-655-2
- 78-6. **18th World Hydrogen Energy Conference 2010 – WHEC2010**
Proceedings
Parallel Sessions Book 6:
Stationary Applications / Transportation Applications
ed. by D. Stolten, T. Grube (2010), ca. 330 pages
ISBN: 978-3-89336-656-9

78 Set (complete book series)

**18th World Hydrogen Energy Conference 2010 – WHEC2010
Proceedings**

ed. by D. Stolten, T. Grube, B. Emonts (2010)

ISBN: 978-3-89336-657-6

79. Ultrafast voltex core dynamics investigated by finite-element micromagnetic simulations

by S. Gliga (2010), vi, 144 pages

ISBN: 978-3-89336-660-6

80. Herstellung und Charakterisierung von keramik- und metallgestützten Membranschichten für die CO₂-Abtrennung in fossilen Kraftwerken

von F. Hauler (2010), XVIII, 178 Seiten

ISBN: 978-3-89336-662-0

81. Experiments and numerical studies on transport of sulfadiazine in soil columns

by M. Unold (2010), xvi, 115 pages

ISBN: 978-3-89336-663-7

82. Prompt-Gamma-Neutronen-Aktivierungs-Analyse zur zerstörungsfreien Charakterisierung radioaktiver Abfälle

von J.P.H. Kettler (2010), iv, 205 Seiten

ISBN: 978-3-89336-665-1

83. Transportparameter dünner geträgerter Kathodenschichten der oxidkeramischen Brennstoffzelle

von C. Wedershoven (2010), vi, 137 Seiten

ISBN: 978-3-89336-666-8

84. Charakterisierung der Quellverteilung von Feinstaub und Stickoxiden in ländlichem und städtischem Gebiet

von S. Urban (2010), vi, 211 Seiten

ISBN: 978-3-89336-669-9

85. Optics of Nanostructured Thin-Film Silicon Solar Cells

by C. Haase (2010), 150 pages

ISBN: 978-3-89336-671-2

86. Entwicklung einer Isolationsschicht für einen Leichtbau-SOFC-Stack

von R. Berhane (2010), X, 162 Seiten


ISBN: 978-3-89336-672-9

87. Hydrogen recycling and transport in the helical divertor of TEXTOR

by M. Clever (2010), x, 172 pages

ISBN: 978-3-89336-673-6

88. **Räumlich differenzierte Quantifizierung der N- und P-Einträge in Grundwasser und Oberflächengewässer in Nordrhein-Westfalen unter besonderer Berücksichtigung diffuser landwirtschaftlicher Quellen**
von F. Wendland et. al. (2010), xii, 216 Seiten
ISBN: 978-3-89336-674-3
89. **Oxidationskinetik innovativer Kohlenstoffmaterialien hinsichtlich schwerer Luftfeinbruchstörfälle in HTR's und Graphitentsorgung oder Aufarbeitung**
von B. Schlögl (2010), ix, 117 Seiten
ISBN: 978-3-89336-676-7
90. **Chemische Heißgasreinigung bei Biomassenvergasungsprozessen**
von M. Stemmler (2010), xv, 196 Seiten
ISBN: 978-3-89336-678-1
91. **Untersuchung und Optimierung der Serienverschaltung von Silizium-Dünnschicht-Solarmodulen**
von S. Haas (2010), ii, 202 Seiten
ISBN: 978-3-89336-680-4
92. **Non-invasive monitoring of water and solute fluxes in a cropped soil**
by S. Garré (2010), xxiv, 133 pages
ISBN: 978-3-89336-681-1
93. **Improved hydrogen sorption kinetics in wet ball milled Mg hydrides**
by L. Meng (2011), II, 119 pages
ISBN: 978-3-89336-687-3
94. **Materials for Advanced Power Engineering 2010**
ed. by J. Lecomte-Beckers, Q. Contrepois, T. Beck and B. Kuhn
(2010), 1327 pages
ISBN: 978-3-89336-685-9
95. **2D cross-hole MMR – Survey design and sensitivity analysis for cross-hole applications of the magnetometric resistivity method**
by D. Fielitz (2011), xvi, 123 pages
ISBN: 978-3-89336-689-7



The presence and flow of water in the shallow subsurface controls a number of phenomena of great environmental interest like mountain slope instability, floods as well as soil and groundwater contamination. A better understanding of these processes is necessary to guarantee a sustainable use of soils and aquifers as well as to maintain acceptable groundwater quality.

The magnetometric resistivity (MMR) method measures low-level (typically below 1 nT) magnetic fields associated with a low-frequency (1–20 Hz) electric current impressed into the ground to determine the subsurface resistivity structure. As a step towards the implementation of MMR for cross-hole imaging, in this Ph.D. thesis several aspects of survey design for near-surface applications are discussed. In numerical, laboratory and field studies the potential of MMR for advanced structural characterization and process monitoring at the field scale is assessed. The considered 2D cross-hole setup comprises borehole measurements of the magnetic field as response to borehole current injection.